MRI ASSESSMENT OF BRAIN IRON CONTENT IN METHAMPHETAMINE
USERS

By

Yosef A. Berlow

DISSERTATION

Presented to the
Department of Behavioral Neuroscience
and the
Oregon Health & Science University School of Medicine
in partial fulfillment of
the requirements for the degree of

Doctor of Philosophy

July 2014

School of Medicine
Oregon Health & Science University

CERTIFICATE OF APPROVAL

This is to certify that the PhD dissertation of

Yosef A. Berlow

**MRI ASSESSMENT OF BRAIN IRON CONTENT IN METHAMPHETAMINE
USERS**

has been approved

_____
Mentor/Advisor - William Rooney, Ph.D.

_____
Committee Chair – Suzanne Mitchell, Ph.D.

_____
Committee Member - William Hoffman, M.D., Ph.D.

_____
Committee Member - Charles Meshul, Ph.D.

_____
Committee Member – Randall Woltjer, M.D., Ph.D.

Table of Contents

Abbreviations

6-OHDA 6-hydroxydopamine
ATP .... adenosine triphosphate
B_0 .... magnetic field
BBB .... blood brain barrier
BET .... Brain Extraction Tool
CNS............. central nervous system
CSF .... cerebrospinal fluid
DA .... dopamine
DA-Q .... dopamine quinones
DAT .... dopamine transporter
DMT .... divalent metal transporter
FDRI .... field-dependent relaxation rate increase
Fe .... iron
FIRST .... FMRIB's Integrated Registration and Segmentation Tool
FLASH .... fast low angle shot
f_M .... macromolecular fraction
FNIRT .... FMRIB's Nonlinear Image Registration Tool
FSL .... Functional Magnetic Resonance Imaging of the Brain (FMRIB) Software Library
f_W .... fractional water content
FWHM .... full width half maximum
GABA .... gamma amino butyric acid
H_2O_2 .... hydrogen peroxide
ICC .... intraclass correlation
IRE .... iron regulatory element
IRP .... iron regulatory protein
M_0 .... net magnet moment at equilibrium
MA .... methamphetamine
MAO .... monoamine oxidase
MNI152 .... Montreal Neurological Institute 152 subject standard space template
MPP+ 1-methyl-4-phenylpyridinium
MPRAGE .... magnetization prepared acquisition gradient echo
MPTP 1-methyl-4-phenyl-1,2,3,6-tetrahydropyridine
MR .... magnetic resonance
MRI .... magnetic resonance imaging
MS .... multiple sclerosis
NADPH .... nicotinamide adenine dinucleotide phosphate
NMDA .... N-methyl-D-aspartate
NO.............. nitric oxide
PD .... proton density
R_1 .... longitudinal relaxation rate constant

r_{1x} .... longitudunal relaxivity for component x
R_2 .... transverse relaxation rate constant
r_{2x} .... transverse relaxivity for component x
RF .... radiofrequency
RNS .... reactive nitrogen species
ROI .... region of interest
ROS .... reactive oxygen species
S .... signal intensity
SNR .... signal to noise ratio
SPM .... Statistical Parametric Mapping
T .... Tesla
T_1 .... longitudinal relaxation time constant
T_2 .... transverse relaxation time constant
TE .... echo time
TH .... tyrosine hydroxylase
TOST .... two one-sided test of equivalence
TRSE .... twice refocused spin echo
TSE .... turbo spin echo
VMAT2 .... vesicular monoamine transporter 2
ω .... Larmor frequency
γ .... gyromagnetic ratio

Index of Figures

Index of Tables

Acknowledgments

I would like to thank Dr. William Rooney for his guidance, mentorship, encouragement and support throughout my graduate training. His efforts provided me the opportunity to learn about the practical and fundamental elements of magnetic resonance imaging over a wide range of applications and helped develop my thinking about the possible questions one could ask. I would like to thank Dr. William Hoffman for his collaboration on this project and openness to allow me to conduct this study. I would like to thank Dr. Suzanne Mitchell for her support and assistance throughout my training in the Department of Behavioral Neuroscience and for serving as chair of my committee. I would like to thank Dr. Charles Meshul for his participation and feedback on my committee. I would like to thank Dr. Randall Woltjer for his participation in my oral examination committee.

I would like to thank current and past members of the Advanced Imaging Research Center for their help, ideas and support: Dr. Manoj Sammi, Jim Pollaro, Audrey Selzer, Brendan Moloney, Eric Earl, Dr. Valerie Anderson, Dr. Charles Springer, Dr. Thomas Barbara, Erin Taber, William Woodward, Ian Tagge, Dr. Lisa Vingara, Mara Bahri, Dr. Merryl Lobo, Dr. Lindsey Leigland, Dr. John Grinstead, Dr. Steven Kohama and Maggie Jameson. I would also like to thank members of the Hoffman lab for doing all of the hard work: Daniel Schwartz, Britta Tremblay, Laura Dennis, Vanessa Wilson and David Lahna. Additional

Finally, I would like to thank my wife, Emilie, for her love, understanding and support.

Abstract

Introduction: Methamphetamine (MA) abuse produces long term changes to the dopamine system that likely contribute to the psychiatric and cognitive symptoms that are seen in MA users. Emerging evidence from preclinical studies suggests that brain iron accumulation plays a role in MA toxicity, both as a biomarker of damage and a potential source of oxidative stress; however, this relationship has not yet been characterized in human MA users. The goal of this study was to utilize in vivo magnetic resonance imaging (MRI) techniques to measure brain iron levels in human subjects with a history of MA dependence and determine if these measurements represent functionally significant biomarkers of MA toxicity. Iron is paramagnetic, and its presence increases the transverse relaxation rate constant (R_2) of nearby water protons causing a loss of signal intensity on T_2-weighted images. Measuring this effect using quantitative MRI techniques allows for in vivo investigation of the effects of MA on the distribution of brain iron.

Methods: MRI datasets were acquired from 27 currently abstinent MA users and 27 aged matched healthy control subjects. Series used in this study included a high-resolution, T_1-weighted MPRAGE, T_2-weighted TRSE, Turbo Spin Echo (TSE) sequences acquired with three different echo times and a 3D proton density (PD) sequence. R_2 ($\equiv 1/T_2$) maps were calculated at each voxel using a monoexponential decay function. Maps of the fractional macromolecular (f_M) content were created by normalizing PD images intensities to the peak intensity

values of voxels within the cerebrospinal fluid. Parametric maps of the distribution of iron content were then calculated using a relaxometry model incorporating the combined effects of f_M and iron content. These parametric iron maps were registered to a common brain space. The effect of MA on regional iron distribution was assessed using both region of interest analysis and voxel-wise linear models. Additional analyses were also conducted using the R_2 and f_M maps, as well as T_2-weighted signal intensity measurements.

Results: Using quantitative relaxometry measures that are specific for iron, I was unable to detect any differences in regional iron content in former MA users when compared to aged-matched healthy control subjects. These measures yielded values for iron and f_M that were in substantial agreement with literature values. These measures also detected strong age associated increases in iron content within basal ganglia regions consistent with previous reports providing a positive control for these methods. While no group differences in iron accumulation were found, the MA group had significantly reduced f_M values in the thalamus, suggesting increased tissue water content in this region.

Discussion: Contrary to the proposed hypothesis, this study found no evidence of altered iron accumulation in abstinent MA users, suggesting that iron accumulation is not a useful biomarker of MA toxicity. This finding is in marked contrast to a study in nonhuman primates which demonstrated an MA induced increase in iron accumulation that was similar to the effects of advanced aging. The discrepancy between these findings is likely due to interspecies differences in brain iron accumulation.

Methamphetamine toxicity and brain iron accumulation

Introduction

Methamphetamine (MA) is a highly addictive, stimulant drug of abuse that represents a serious public health problem in the US, with over 1 million Americans reporting past-year use and over 12 million reporting lifetime use (Substance Abuse and Mental Health Services Administration, 2012). Long-term MA abuse is associated with psychiatric morbidity, including addiction, mood disturbances and psychosis, and impairment in cognitive domains, including memory and executive function (Simon et al., 2000; Zweben et al., 2004; Rusyniak, 2011). These changes in mood and cognition are likely due to the toxic effects of MA on the dopamine (DA) system that result in reduced markers of DA transmission, terminal degeneration and neuronal death (Wilson et al., 1996; Cadet et al., 2003; Ares-Santos et al., 2014). Damage to DA neurons is often accompanied by an increase in iron accumulation (Oestreicher et al., 1994). This relationship has been investigated and documented for several drugs that cause selective damage to DA neurons (Salazar et al., 2008; Jiang et al., 2010; Carroll et al., 2011). Emerging evidence suggests that iron plays an important role in MA toxicity as well, both as a biomarker of damage (Melega et al., 2007) and a source of increased oxidative stress (Yamamoto and Zhu, 1998; Park et al., 2006).

Iron is essential for many cellular processes including oxygen transport,

oxidative metabolism, and DNA replication and repair. It is normally found in high concentrations in many of the same regions that are affected by MA, including the substantia nigra, striatum and pallidum (Hallgren and Sourander, 1958). In DA neurons, iron is required by tyrosine hydroxylase (TH) to synthesize DA and deficiencies in iron levels, especially in early development, have been shown to lead to chronic impairment in normal DA functioning (Beard, 2003). However, at excess levels, iron can contribute to increased oxidative stress due to its ability to form highly reactive oxygen species (ROS). Abnormally increased iron levels have been associated with cognitive and motor impairment due to aging, Alzheimer's disease, and Parkinson's disease (Martin et al., 1998; Cass et al., 2007; Ding et al., 2009; Sullivan et al., 2009; Penke et al., 2010; Bartzokis et al., 2011) and have been implicated as a risk factor for developing neurodegenerative dementias (Bartzokis et al., 2007a). In rodent models, increasing brain iron content by dietary iron supplementation during the neonatal period has been shown to result in decreased levels of DA in adulthood, accelerated age-associated DA neuron loss and enhanced vulnerability to DA toxins (Kaur et al., 2007). Similarly, peripheral iron loading has also been shown to increase brain iron accumulation and decrease DA levels in the striatum and reduce the number TH positive cells in the substantia nigra (Jiang et al., 2007). Finally, direct injection of iron into the substantia nigra has been shown to produce DA depletions in the striatum and behavioral changes associated with nigrostriatal lesions (Ben-Shachar and Youdim, 1991; Sengstock et al., 1993). If

2

present, increased iron levels in MA users may contribute to the psychiatric and neurological comorbidity associated with chronic MA abuse. In this chapter, I will examine studies that suggest that MA increases brain iron accumulation, explore mechanisms implicated in MA toxicity that could bring about alterations in iron handling, review the evidence that iron potentiates MA induced oxidative stress and discuss the implications of these findings for future studies.

Methamphetamine increases brain iron accumulation

Preliminary evidence that MA increases brain iron accumulation was first described by Woolverton and colleagues 25 years ago (Woolverton et al., 1989). In this paper, they described the neuropathological changes in two rhesus macaques who had been part of an MA self administration study four years earlier (Woolverton et al., 1984; Woolverton et al., 1989). One of these monkeys had received a total of 14 escalating doses of MA ranging from 4 to 40 mg/kg. The second monkey was exposed to 28 MA administrations with more than half of the doses ranging from 20.0 to 60.0 mg/kg. This second monkey displayed dramatic reductions in serotonin and DA levels and uptake, while the other MA exposed animal only showed mild reductions in serotonin. In addition, these authors noted that the monkey who had been exposed to several high dose MA administrations had "an increase in iron pigment...in the substantia nigra".

A more recent study by followed up on this initial observation and investigated the effects of acute MA exposure on brain iron accumulation in eight

3

young adult vervet monkeys (Melega et al., 2007). They administered two 2.0 mg/kg doses of MA to five of the animals and saline injections to the other three animals. In contrast to the earlier study, this dose of MA is more comparable to doses taken by human MA users (Kramer et al., 1967; Cho and Melega, 2002) and was chosen because it had been shown to be capable of depleting striatal DA without causing cell death (Harvey et al., 2000). The animals were then sacrificed at either one month (2/5 monkeys in the MA group and all 3 saline controls) or one and a half years post drug administration (3/5 in MA group). At one month, the acute effects of MA were demonstrated with decreased TH immunoreactivity in the substantia nigra. These acute effects were accompanied by an increase in iron staining and an increase in the immunoreactivity of the iron storage protein, ferritin, in the substantia nigra pars reticulata. One and a half years after administration, TH activity returned to baseline in the nigra, however, the iron staining and ferritin immunoreactivity continued to be increased, reaching levels that were 2.5 and 3.1 fold those of controls, respectively. In the pallidum, at one a half years, animals that received MA had iron staining that was 2.5 fold greater than aged matched controls and reached levels seen in advanced aged monkeys (Melega et al., 2007). Figure 2 from the (Woolverton et al., 1989; Melega et al., 2007; Melega et al., 2007) paper illustrates the differences in iron staining between the three groups in the pallidum and suggests that there may also be increased iron staining in the nearby putamen in the MA treated animal. Digital image analysis of the intensities within this region confirms lower mean

4

intensities as shown in **Figure 1**. Unfortunately, the authors did not explicitly analyze or comment on this or other basal ganglia regions. Nevertheless, this study demonstrates that acute administration of MA can lead to increased brain iron accumulation that is sustained long after the last dose of MA and even after recovery of normal TH activity in the nigra. This altered pattern of brain iron accumulation may represent an acceleration of the pattern seen in normal aging and suggests that MA users may be predisposed to age-associated
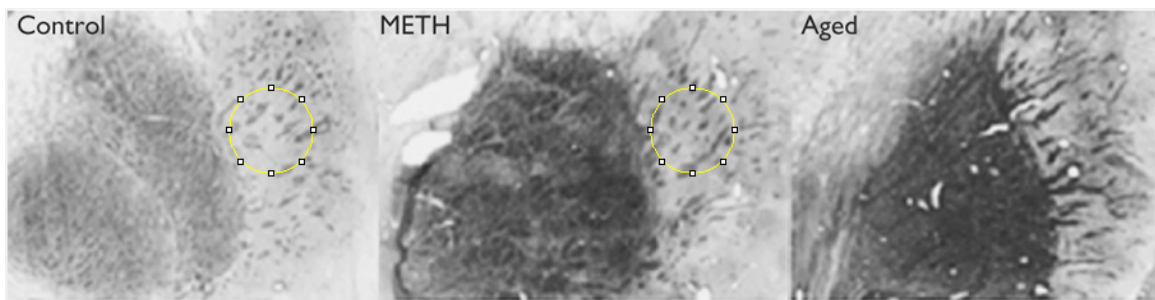
Figure 1: Image analysis of iron staining within the putamen.
Circular regions of interest were used to analyze Figure 2 from Melega et al. 2007 (top panel). The distributions of pixel intensities within these regions of interest demonstrate a shift to lower intensities in the putamen of methamphetamine (MA) treated monkeys (red), suggesting greater iron staining within the putamen in addition to the more dramatic increase that is seen in the pallidum (lower panel; dotted lines represent mean pixel intensity).

5

neurodegenerative processes associated with increased iron accumulation, such as Parkinson's disease.

In a study by Todd et al. (2013), transcranial sonography was used to measure echogenicity in the substantia nigra of human stimulant users, cannabis users and non-drug using control subjects. This measure is thought to reflect the presence of increased iron in the brainstem (Berg et al., 2002; Zecca et al., 2005; Todd et al., 2013) and has been used extensively to demonstrate abnormal increases in echogenicity in Parkinson's disease, a disease with selective damage to dopamine neurons within the substantia nigra pars compacta (Berg, 2011). In this study, the stimulant group consisted of 36 polydrug using subjects who used MA, methylenedioxymethamphetamine (MDMA), and/or cocaine. Eighty one percent of these subjects reported using MA. Individuals in the stimulant group were found to have increased echogenicity in the substantia nigra when compared to both cannabis users and to individuals with no illicit drug use history. In fact, 53% percent of the stimulant users displayed echogenicity that exceeded the 90th percentile seen in control subjects. This finding of hyperechogenicity in the substantia nigra has been shown to be associated with decreased dopamine functioning in healthy control subjects (Berg et al., 2002; Todd et al., 2013) and increased risk of developing Parkinson's disease (Berg, 2011; Berg et al., 2013). A recent epidemiological study suggests that MA use is also associated with an increased risk of Parkinson's disease (Callaghan et al., 2012).

Together, these two studies support the hypothesis that MA increases brain iron accumulation in specific basal ganglia regions, including the substantia nigra and pallidum. However, in each of these studies, there are important limitations to consider. In the study by , saline treated animals were sacrificed 1 month after injection and then compared to MA treated animals 1.5 years later. Human and nonhuman primates rapidly accumulate iron in the pallidum during the first two decades of life and the lack of a control group waiting a similar period of time after injection may have masked any of the age related increases in brain iron that might have been seen over this 17 month period. Similarly, it is unclear what the age distributions were for each of these groups. In addition, there is evidence from our group and others, that old world monkeys (Japanese macaque and Rhesus macaque) accumulate approximately twice the amount of iron in the pallidum with age compared to humans, suggesting important species specific differences in iron handling in the pallidum that may limit our ability to generalize these findings to human MA users (Hardy et al., 2005; Berlow et al., 2012a).

In the study by Todd et al. (2013), it is not clear that changes in echogenicity measured by sonogram are specific for increased iron. Modest correlations between iron levels in the substantia nigra and transcranial echogenicity measures have been found, however, based on these studies, echogenicity measures account for less than 10% of variance in substantia nigra iron content (Zecca et al., 2005). It is also difficult to ascribe all of the group

7

differences in echogenicity to MA abuse. The stimulant group was older (mean 31 years old) than the two control groups (24 and 25 years old). This group was also defined by the use of a variety of stimulant drugs of abuse and differed from the two control groups in their use of multiple drugs, including alcohol and cigarettes. Polydrug abuse is a common confounding factor in most human substance abuse studies and to their credit, the authors acknowledge many of these issues. Finally, the measurement of echogenicity area was performed by a rater who was not blinded to subject grouping, introducing potential bias in the measurement; and attempts to demonstrate inter-rater reliability in a subset of the data yielded only modest intraclass correlations (ICC = 0.57). Despite these limitations, these studies provide preliminary evidence that MA increases brain iron accumulation.

Mechanisms of methamphetamine toxicity and iron metabolism

MA neurotoxicity involves a cascade of interacting processes that increase oxidative and metabolic stress and ultimately result in damage to the DA system. MA has been shown to result in excess cytosolic DA degradation, proteasome impairment, mitochondrial dysfunction, alterations in glutamate and GABA transmission, blood brain barrier (BBB) disruption, and microglial activation. These mechanisms have been shown to cause increased brain iron accumulation using other drugs which are toxic to DA neurons, such as 6-OHDA, MPTP and lactacystin. In many of these models, the alterations in brain iron

metabolism have been shown to be due to the effects of these processes on the activity and availability of iron regulatory proteins, leading to increased iron uptake and accessibility (Jiang et al., 2003; Salazar et al., 2008; Jiang et al., 2010; Carroll et al., 2011). In the following section, I will review the evidence supporting the involvement of these mechanisms in MA toxicity and the possible roles these processes might play in MA induced alterations in iron metabolism.

Oxidative stress

One of the primary causative mechanisms implicated in MA toxicity is increased oxidative stress (Cadet and Brannock, 1998; Brown and Yamamoto, 2003)(Riddle et al., 2006; Yamamoto and Raudensky, 2008). Oxidative stress can be defined as an excess of oxidizing species, such as reactive oxygen and nitrogen species (ROS and NOS), in relation to the cell's endogenous antioxidant defense systems; leading to oxidation and damage of proteins, lipid membranes and nucleic acids. As we will see, the pharmacodynamic effects of MA increase oxidative stress by several mechanisms that begin with MA's ability to release DA from vesicular stores. MA is a small (149 daltons), lipophilic (log Kow=2.07), weak base (pKa=9.9) that rapidly crosses the BBB via lipid-mediated free diffusion (National Center for Biotechnology Information, (accessed Feb. 22, 2014).). It enters neurons through uptake at monoamine transporters, with a high affinity for the DA transporter (DAT) (Sulzer et al., 2005). At the DAT, it produces reverse transport, causing increased levels of DA release into the synapse

9

(Sulzer et al., 1995). This mechanism also prevents normal reuptake of DA from the synapse further increasing synaptic DA levels. In the DA nerve terminal, MA accumulates in DA vesicles and induces release of DA from vesicular stores by collapsing the pH gradient of the vesicle and blocking and reversing the vesicular monoamine transporter 2 (VMAT2), preventing vesicular uptake (Sulzer et al., 1995; Sulzer et al., 2005). These processes lead to excess DA release and degradation within the cytosol. Chronic administration of MA may also lead to decreased activity and down regulation of the DAT, reducing the ability of DAT to clear cytosolic DA, and increasing DA degradation within the cytosol (Riddle et al., 2006). When cytosolic DA is degraded enzymatically by monoamine oxidase B (MAO-B) or nonenzymatically via autooxidation, it produces reactive oxidation products, including hydrogen peroxide (H_2O_2) (Cubells et al., 1994), DA quinones (Sulzer and Zecca, 2000; Miyazaki et al., 2006) and 6-hydroxydopamine (6-OHDA) (Seiden and Vosmer, 1984; Marek et al., 1990; Napolitano et al., 1995; Pezzella et al., 1997). DA and the reactive metabolites of DA are capable of releasing iron from ferritin (Double et al., 1998). In the presence of ferrous iron (Fe^{+2}), additional oxygen free radicals can be produced through the Fenton and Haber Weis reactions. Large changes in levels of brain antioxidants have been demonstrated in animal models (Jayanthi et al., 1998; Moszczynska et al., 1998; Kim et al., 1999), suggesting increases in oxidative stress. Similarly, changes in brain antioxidant levels have been reported in human MA users (Mirecki et al., 2004). More direct measures of increased oxidative stress, such as increased

levels of malondialdehyde and 4-hydroxynonenal indicating lipid peroxidation, have been demonstrated in the blood (Suriyaprom et al., 2011)and brain (Fitzmaurice et al., 2006) of human MA users, mirroring results seen in rodent models (Açikgöz et al., 1998; Yamamoto and Zhu, 1998; Gluck et al., 2001; Flora et al., 2002; Park et al., 2006). Furthermore, several studies have demonstrated that pretreatment with antioxidants, such as vitamin E and vitamin C, can attenuate some of the measures of MA damage, indicating the importance of oxidative stress in MA toxicity (Wagner et al., 1985; Vito and Wagner, 1989; Imam et al., 2001; Park et al., 2006).

MA induced increases in oxidative stress may cause alterations in iron metabolism by affecting the Iron Regulatory Protein / Iron Responsive Element (IRP/IRE) system as shown in **Figure 2**. Iron Responsive Elements (IRE) are found on the untranslated regions of iron regulated mRNAs that code for several proteins related to iron metabolism (Levenson and Tassabehji, 2004). Activated Iron Regulatory Proteins (IRP-1 and IRP-2) are able to bind to these IREs, affecting the mRNA stability and translation. This posttranscriptional regulation process is normally controlled by circulating levels of cystolic iron. When iron levels are normal or increased, an iron-sulfer cluster is formed on IRP-1, making it unable to interact with the IREs on the mRNA (Levenson and Tassabehji, 2004). High iron levels also lead to the ubiquitination and degradation of IRP-2 leading to decreased interactions with IREs (Guo et al., 1995). When iron levels are low, IRPs are activated and able to bind to IREs, which increases the stability

11
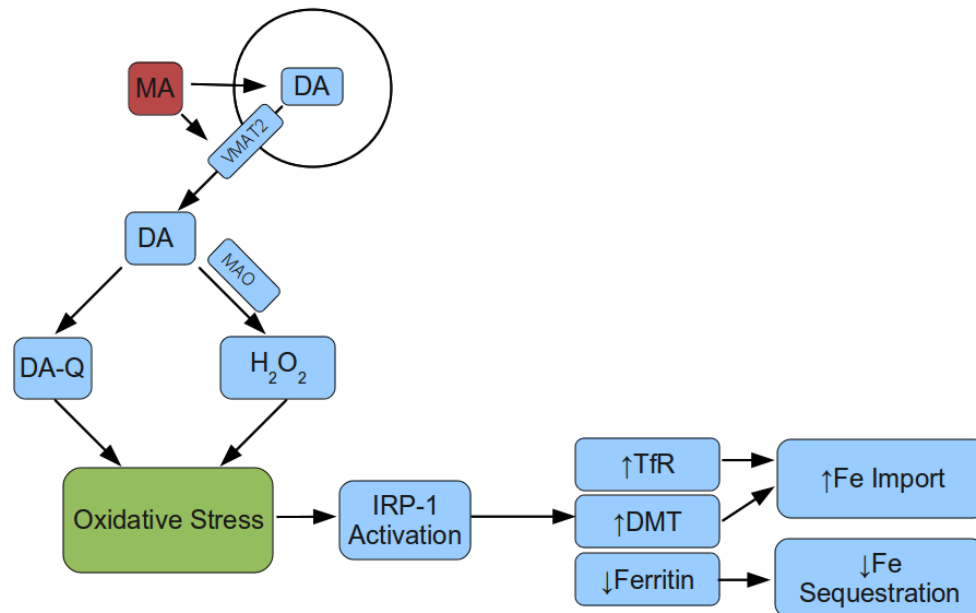
Figure 2: Hypothetical model of the acute effects of MA induced oxidative stress on iron regulation.
MA causes release of DA from vesicular stores, leading to excess DA degradation within the cytosol and production of reactive oxygen species. The resulting increased oxidative stress may be capable of activating IRP-1 in a manner that is independent of iron status, leading to increased translation of the iron import proteins, DMT and TfR, and decreased translation of the iron storage protein, ferritin. DA=dopamine; DA-Q=dopamine quinones; DMT=divalent metal transporter; Fe=iron; H2O2=hydrogen peroxide; IRP-1=iron regulatory protein 1; MA=methamphetamine; MAO=monoamine oxidase; TfR=transferrin receptor; VMAT2=vesicular monoamine transporter 2.

and translation of mRNAs with IREs at the 3' region, including those coding for the transferrin receptor and the divalent metal transporter (DMT). Increases in the translation of these proteins accelerates cellular iron uptake. Conversely, when an IRP binds to the IRE located on the 5' end of mRNA coding for ferritin, translation is inhibited and the ability of the cell to bind and store free iron is decreased (Levenson and Tassabehji, 2004). High levels of oxidative stress are

also able to activate IRP-1 independent of iron status (Pantopoulos et al., 1996). The activation of IRP-1 makes it capable of binding to the IRE's, increasing the translation of the transferrin receptor and the divalent metal transporter (DMT), and decreasing the translation of ferritin (Pantopoulos et al., 1996; Levenson and Tassabehji, 2004). Following a reduction in the oxidative stress levels, the increased iron would bind to IRP-1 and signal for the degradation of IRP-2, making them incapable of interacting with IREs, increasing the ferritin expression and decreasing expression of the transferrin receptor and the DMT. These processes would ultimately lead to increased iron accumulation.

If MA induced oxidative stress was capable of activating IRP-1, an early down-regulation of ferritin mRNA would be predicted. Analysis of gene expression in the rat striatum following neurotoxic MA administration has shown that ferritin mRNA is down-regulated 1.6 fold (Cai et al., 2006). Similarly, proteomic expression data from Drosophila treated with MA show a 10 fold reduction in ferritin levels (Sun et al., 2011). There is also evidence that neurotoxic doses of MA upregulate tranferrin mRNA in the striatum, leading to increased delivery of iron to this area, however, the mechanism of this upregulation is unknown (Cai et al., 2006). As shown in **Figure 3**, following the acute oxidative stress period, IRP-1 would be deactivated and unable to bind to the IRE, leading to increased ferritin expression, as was seen in vervet monkeys examined 1 month and 1.5 years after acute MA administration (Melega et al., 2007). An increase in ferritin expression following MA treatment was also seen in

cultured astrocytes (Shah et al., 2013). These results are consistent with the hypothesis that MA induced oxidative stress alters the expression of proteins involved in iron handling through activation of IRP-1.

Inhibition of the ubiquitin proteasome system

The MA induced increase in oxidative stress could also alter iron metabolism through its effects on the ubiquitin proteasome system. Excess production of ROS causes oxidative damage to proteins that are subsequently
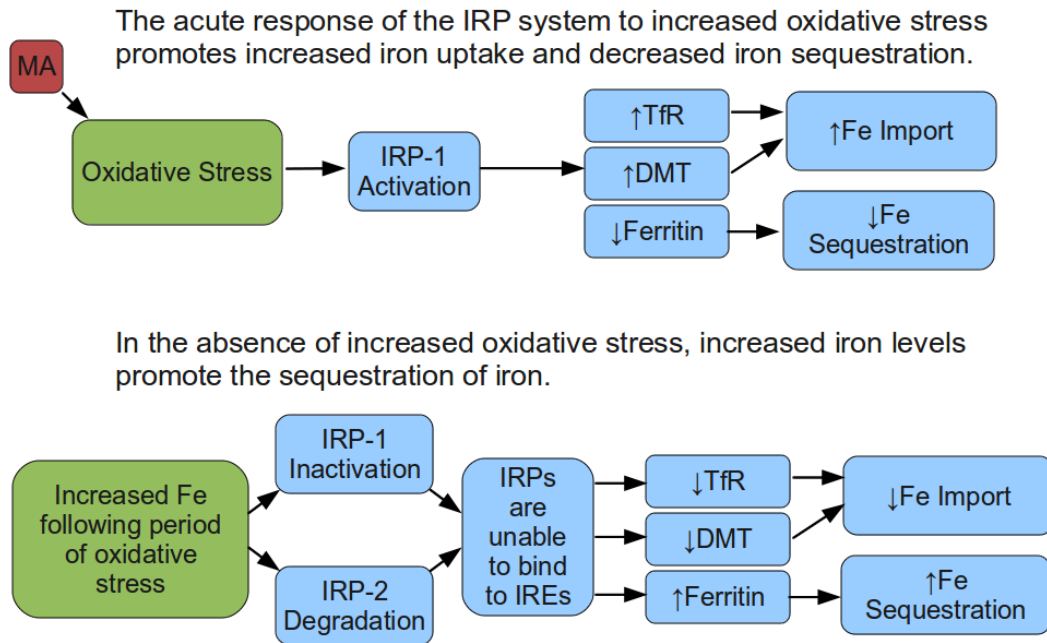
Figure 3: Hypothetical model of the subsequent effects of MA induced oxidative stress on iron regulation.
After a period of increased oxidative stress and increased iron uptake, iron dependent regulation of the IRP system increases translation of the iron storage protein, ferritin, and promotes iron sequestration. DMT=divalent metal transporter; Fe=iron; IRP-1=iron regulatory protein 1; IRP-2=iron regulatory protein 2; MA=methamphetamine; TfR=transferrin receptor.

ubiquitinated and degraded by the ubiquitin proteasome system. If the proteasome is unable to remove these damaged proteins, aggregations may form similar to the inclusion bodies seen in Parkinson's disease. Several studies have confirmed that MA induces the formation of inclusion bodies in both in vitro and in vivo models (Fornai et al., 2003; Fornai et al., 2004a, b; Fornai et al., 2005; Lazzeri et al., 2006; Lazzeri et al., 2007). In mice treated with MA, neuronal inclusions positive for components of the ubiquitin proteasome system, including ubiquitin, ubiquitin-activating enzyme and ubiquitin ligase were found in both the striatum and substantia nigra (Fornai et al., 2004a). Furthermore, increased levels of diffuse ubiquitin positive inclusions have been reported in the substantia nigra of human MA users at autopsy (Quan et al., 2005). In this study, the degree of ubiquitin positive staining was correlated with blood levels of MA at the time of death (Quan et al., 2005). Inclusion bodies produced by MA share a remarkable similarity to those produced by proteasome inhibitors (Fornai et al., 2004a; Sun et al., 2011) and treatment of neuronal cell cultures with MA has been shown to inhibit proteasome activity (Fornai et al., 2006; Lin et al., 2012). Similarly, decreases in proteosome activity have been reported in rats after neurotoxic doses of MA (Moszczynska and Yamamoto, 2011). These studies strongly support the role of proteasome inhibition in MA toxicity.

MA induced inhibition of the proteasome may lead to increased iron accumulation by altering the availability and activity of proteins related to iron homeostasis and metabolism as shown in **Figure 4**. Levels of IRP-2 are normally
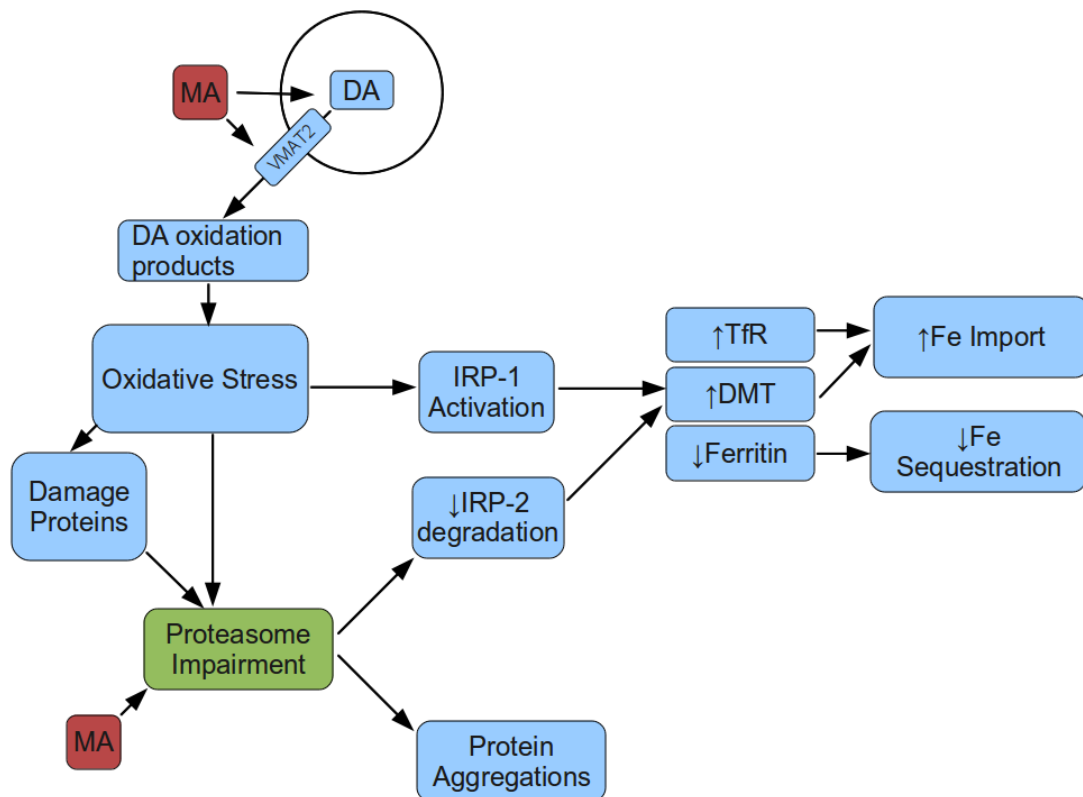
Figure 4: Hypothetical model of the role of MA induced proteasome impairment on iron regulation.
MA induced oxidative stress causes increased demand and impairment to the ubiquitin proteasome system, leading to the formation of protein aggregations. Proteasome impairment would also decrease the degradation of IRP-2, leading to increased cellular iron accumulation. DA=dopamine; DA-Q=dopamine quinones; DMT=divalent metal transporter; Fe=iron; H_2O_2=hydrogen peroxide; IRP-1=iron regulatory protein 1; IRP-2=iron regulatory protein 2; MA=methamphetamine; MAO=monoamine oxidase; TfR=transferrin receptor; VMAT2= vesicular monoamine transporter 2.

regulated by proteasome degradation in response to high iron levels (Guo et al., 1995). Impairment of this pathway by inhibiting the proteasome has been shown to lead to dysregulation of iron homeostasis, increased iron accumulation and cell injury. Treatment of DA neurons with the proteasome inhibitor, lactacystin, results in increased levels of IRP-2, leading to increased expression of the

tranferrin receptor, decreased expression of ferritin and an increase in labile iron and ROS (ping Li et al., 2012). This process creates a vicious cycle in which increased oxidative stress leads to increased damaged proteins and increased demands of the impaired proteasome system (ping Li et al., 2012). Similarly, in vivo models of proteasome inhibition demonstrate that this mechanism is capable of causing degeneration of DA neurons accompanied by neuronal inclusions and an increase in iron accumulation (Zhang et al., 2005; Zhu et al., 2007). These studies suggest that alterations in iron metabolism due to proteasome inhibition may play a role in MA toxicity.

Production of 6-hydroxydopamine

MA evoked release of DA from vesicular stores may lead to the formation of 6-hydroxydopamine (6-OHDA), a potent dopaminergic neurotoxin that is capable of increasing neuronal iron accumulation and accessibility. In vitro, the nonenzymatic oxidation of DA has been shown to produce 6-OHDA in the presence of H_2O_2 and peroxidase (Napolitano et al., 1995) or H_2O_2 and small amounts of iron (Linert et al., 1996; Pezzella et al., 1997). MA may promote conditions to favor this reaction in vivo by disrupting the vesicular storage of DA and increasing intracellular DA degradation, producing intracellular H_2O_2 in brain regions with high iron levels. High dose MA administration (50-100 mg/kg) in rats has been shown to produce measurable amounts of 6-OHDA in the striatum (Seiden and Vosmer, 1984; Seiden, 1985; Marek et al., 1990). MA induced

production of 6-OHDA is greatly enhanced by co-administration of MAO inhibitors, suggesting that this oxidation pathway may be avoided by enzymatic degradation of DA (Marek et al., 1990; Liao et al., 2003). While these studies demonstrate that MA is capable of producing 6-OHDA in vivo, the resulting levels of 6-OHDA are low and short lived (Seiden and Vosmer, 1984; Seiden, 1985; Marek et al., 1990). In addition, some studies have been unable to detect 6-OHDA after administration of high doses of MA (Karoum et al., 1993), leading some to question whether 6-OHDA production is an important factor in MA toxicity (Wrona et al., 1997). It has been suggested that this difficulty in measuring MA induced 6-OHDA may be due to its highly reactive nature (Wrona et al., 1997). 6-OHDA undergoes rapid auto-oxidization to form oxygen radicals, H_2O_2 and quinones, and, similar to MA toxicity, this increased oxidative stress is one of the primary mechanisms of 6-OHDA toxicity (Blum et al., 2001).

In vitro and in vivo models of 6-OHDA toxicity cause degeneration of DA neurons accompanied by iron accumulation. Increased iron levels in the substantia nigra have been demonstrated in rats shortly after 6-OHDA administration (2 or 3 weeks)(Oestreicher et al., 1994; Jiang et al., 2010) and persist up to one year (He et al., 1996). Similar increases in iron have been reported in other brain regions including the putamen and pallidum, but these increases are much lower magnitude than those seen in the substantia nigra (Tarohda et al., 2005). This increase in iron accumulation in the substantia nigra is associated with an upregulation in the IRE+ form of DMT-1, leading to

increased iron transport into the cell (Song et al., 2007; Jiang et al., 2010). In cell culture models, iron accumulation due to 6-OHDA was found to be IRP/IRE dependent and associated with an increased expression IRP-1 and IRP-2, which led to increased expression of DMT-1 and transferrin receptor 1 (Jiang et al., 2010). In this model, attenuating the 6-OHDA induced oxidative stress with an
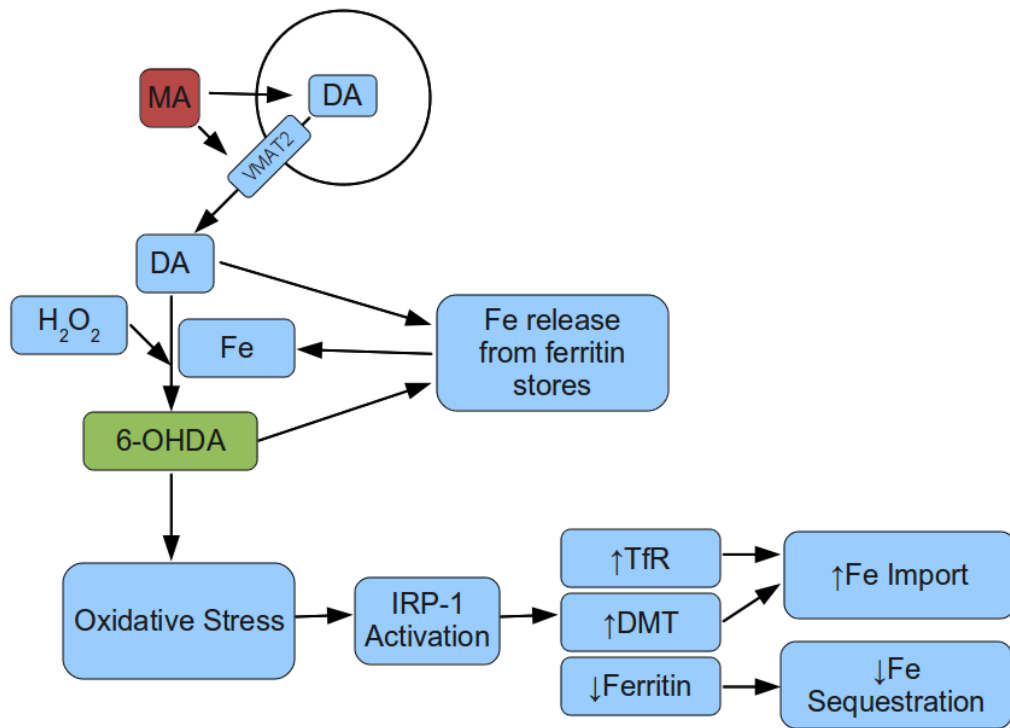
Figure 5: Hypothetical model of the effect of MA induced 6-hydroxydopamine (6-OHDA) formation on iron homeostasis.
Dopamine release following MA administration is capable of releasing iron from ferritin, potentially catalyzing the production of 6-OHDA and other reactive oxygen species. 6-OHDA could perpetuate this catalysis by a similar interactions with ferritin, increasing iron accessibility. The resulting oxidative stress caused by 6-OHDA could activate the IRP system and result in increased iron accumulation. 6-OHDA= 6-hydroxydopamine; DA=dopamine; DMT=divalent metal transporter; Fe=iron; H_2O_2=hydrogen peroxide; IRP-1=iron regulatory protein 1; MA=methamphetamine; MAO=monoamine oxidase; TfR=transferrin receptor; VMAT2= vesicular monoamine transporter 2.

antioxidant, N-acetyl-cysteine, blocked the upregulation and, presumably, the activation of IRP-1 and IRP-2 (Jiang et al., 2010). 6-OHDA has also been shown to be capable of releasing iron from ferritin in vitro, providing a potential source of additional labile iron that could catalyze the further production of 6-OHDA from DA (Monteiro and Winterbourn, 1989). This process could sustain the continued production of ROS (Linert et al., 1996). These studies suggest that if 6-OHDA is produced by MA, even transiently, it may increase iron accumulation within DA neurons by activating the IRP/IRE system and increase iron accessibility through its actions on ferritin as shown in **Figure 5**.

Mitochondrial dysfunction

MA has been shown to inhibit mitochondrial functioning (Chan et al., 1994; Burrows et al., 2000; Brown et al., 2005; Klongpanichapak et al., 2006) and this metabolic stress may also alter iron homeostasis. Mice treated with a neurotoxic dose of MA (four 10 mg/kg doses with 2 hr intervals) developed a rapid decrease in ATP concentration in striatal tissue that was apparent 1.5 hours after the last injection (Chan et al., 1994). This decrease in ATP levels was associated with DA depletion at 1.5 hours and 1 week. In contrast, mice that were treated with only a single 10 mg/kg dose of MA displayed neither decreased ATP levels nor DA depletion, suggesting that this decrease in ATP production is associated with MA neurotoxicity. Various complexes within the mitochondrial respiratory chain have been implicated in this inhibition. Rats treated with the same neurotoxic dose of

MA displayed a reduction in cytochrome oxidase staining in the striatum two hours after MA administration that recovered at 24 hours, indicating a rapid decrease in the activity of complex IV (Burrows et al., 2000). In a similar study, neurotoxic doses of MA were found to be capable of producing a rapid inhibition of complex II activity that was apparent at 1 hour and was still present at 24 hours (Brown et al., 2005). Decreased complex I immunoreactivity in striatal tissue has also been reported in mice 24 hours after repeated MA administration (Klongpanichapak et al., 2006).

Several models of mitochondrial inhibition are associated with damage to dopamine neurons, increased iron accumulation and altered iron regulatory proteins. One possible contributing mechanism for MA induced inhibition of mitochondria is through the excess release and degradation of DA, producing DA quinones and aminochrome (Miyazaki et al., 2006). In mitochondrial preparations or cell cultures, DA has been shown to be capable of inhibiting complexes I and IV, likely due to interactions with quinones and other DA oxidation products (Ben-Shachar et al., 1995; Khan et al., 2005; Jana et al., 2011). In vitro and in vivo studies suggest that MA is capable of increasing quinone formation. DA cells treated with MA show a dose dependent increase in quinone formation (Miyazaki et al., 2006). Similarly, mice show an increase in striatal quinone formation shortly after MA administration (LaVoie and Hastings, 1999; Miyazaki et al., 2006). This increase in quinone formation is thought to be due to MA induced redistribution of vesicular DA into the cytosol followed by intracellular auto-

oxidation (Sulzer et al., 1995; LaVoie and Hastings, 1999). These DA quinones can easily cyclize to form aminochrome (Sulzer and Zecca, 2000; Sulzer et al., 2005), which is capable of inhibiting mitochondrial complex I (Aguirre et al., 2012). Aminochrome induced mitochondrial inhibition has been shown to alter the expression of the iron regulatory proteins DMT-1 and ferroportin-1 and result in increased iron accumulation (Aguirre et al., 2012).

Other dopaminergic toxins that induce mitochondrial inhibition have also been shown to increase iron accumulation and alter iron regulation. 1-Methyl-4-phenyl-1,2,3,6-tetrahydropyridine (MPTP) is a protoxin that is converted to the toxic metabolite 1-methyl-4-phenylpyridinium (MPP+) by MAO. MPP+ is a potent inhibitor of mitochondrial complex I and causes increased production of ROS and selective degeneration to DA neurons. The behavioral and neurotoxic effects of MPTP were first documented in case studies describing human drug users who injected a synthetic opioid that contained MPTP as a contaminant, resulting in progressive Parkinsonian symptoms and premature loss of DA neurons in the substantia nigra (Davis et al., 1979). After these descriptions, MPTP became a popular animal model for Parkinson's disease due to its ability to mimic many of the features of Parkinson's disease. In rodent and nonhuman primate models, MPTP has been shown to cause extensive nigrostriatal cell death accompanied by increases in iron accumulation (Mochizuki et al., 1994; Temlett et al., 1994; Mandel et al., 2004; Salazar et al., 2008; Hare et al., 2013). In cell culture models, MPP+ was shown to increase expression of mRNA coding for the IRE+

form of DMT-1, the transferrin receptor 1, and the mitochondrial iron transporters, transferrin receptor 2 and mitoferrin 2 (Carroll et al., 2011). Increases in the protein levels were also seen for each of these receptors, except mitoferrin 2 protein, which showed a 10 fold reduction (Carroll et al., 2011). Increases in the expression of DMT-1 along with increased iron accumulation have also been shown in the substantia nigra of mice treated with MPTP (Salazar et al., 2008). The increased expression of some of these iron import proteins, including DMT-1 and transferrin receptor 1, could be due to activation of the IRP/IRE system by the generalized increase in oxidative stress in the cell. Mitochondrial inhibition may also result in specific functional iron deficits within the mitochondria that signal for an increase in cellular and mitochondrial iron uptake (Carroll et al., 2011). Similar results have also been shown with the pesticide, rotenone, which is another inhibitor of complex I that has been shown to destroy DA neurons and increase iron accumulation in rodents and nonhuman primates (Mastroberardino et al., 2009). Based on these models, MA induced inhibition of mitochondrial function may be capable of altering iron metabolism by causing increased production of oxidative species and by causing a functional iron deficiency in mitochondria, leading to alterations in the expression of iron regulatory proteins and increases iron accumulation as shown in **Figure 6**.

Glutamate and GABA

In addition to changes related to increased intracellular DA degradation,
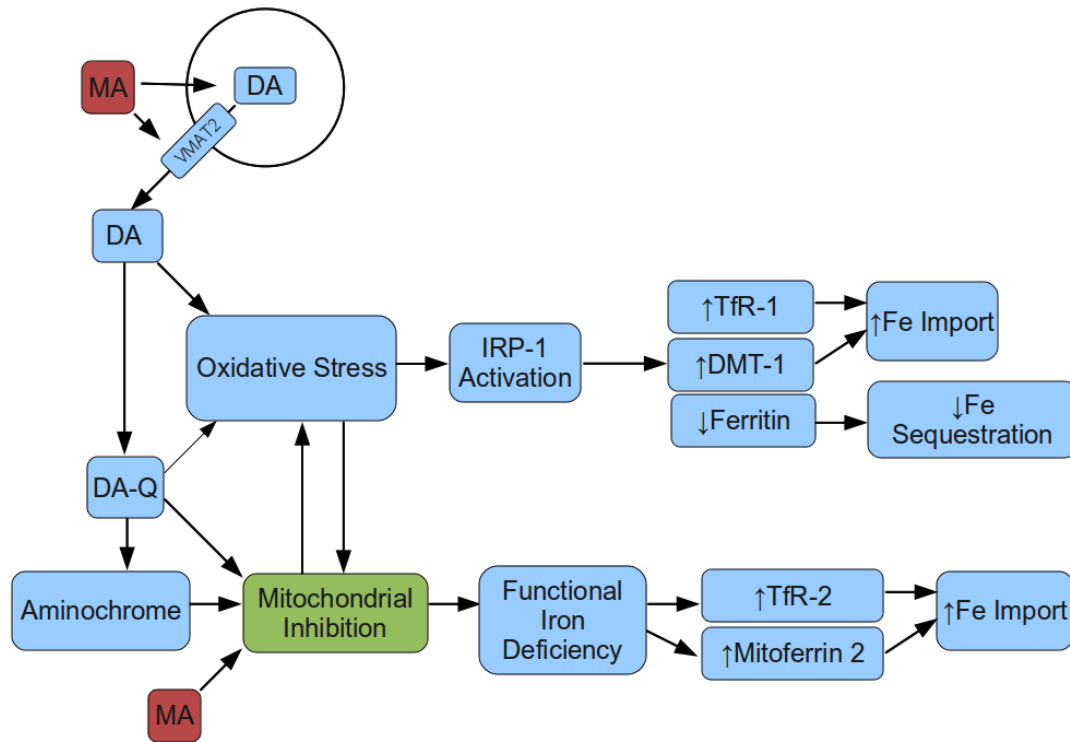
Figure 6: Hypothetical model of MA induced mitochondrial inhibition on iron regulation.
MA induced cytosolic degradation of DA produces DA quinones and related oxidation products that are capable of inhibiting mitochondria and altering the expression of the iron regulatory proteins DMT-1 and ferroportin-1, resulting in increased iron accumulation. Mitochondrial inhibition may also result in functional iron deficits within the mitochondria that lead to increased expression of the mitochondrial iron import proteins, transferrin 2 and mitoferrin 2. DA=dopamine; DA-Q=dopamine quinones; DMT-1=divalent metal transporter 1; Fe=iron; IRP-1=iron regulatory protein 1; MA=methamphetamine; MAO=monoamine oxidase; TfR-1=transferrin receptor-1; TfR-2=transferrin receptor-2; VMAT2= vesicular monoamine transporter 2.

MA's ability to increase synaptic DA levels induces alterations in glutamate and gamma amino butyric acid (GABA) that may also affect iron regulation. In microdialysis experiments, MA has been shown to cause a delayed increase in striatal glutamate levels (Nash and Yamamoto, 1992; Abekawa et al., 1994; Stephans and Yamamoto, 1994). This increase in glutamate combined with

elevated intracellular and extracellular DA appears to mediate several aspects of MA toxicity (Nash and Yamamoto, 1992; Abekawa et al., 1994; Stephans and Yamamoto, 1994; Brown and Yamamoto, 2003; Brown et al., 2005). Glutamate binds to N-methyl-D-aspartate (NMDA) receptors on the DA terminal within the striatum, increasing calcium influx into the cells. This increase in cytosolic calcium stimulates nitric oxide (NO) synthase and leads to the production of NO (Garthwaite, 1991). This increased NO production has been implicated as the primary factor responsible for NMDA mediated excitotoxicity (Dawson et al., 1991; Ayata et al., 1997). NO is capable of interacting with superoxide to form the highly reactive oxidant peroxynitrite (Beckman et al., 1990). In mice, MA has been demonstrated to increase peroxynitrite formation in the striatum (Imam et al., 1999). Blocking activation of NMDA receptors with antagonists has been shown to significantly attenuate MA induced DA depletions (Sonsalla et al., 1989; Ali et al., 1994). NMDA antagonists have also been shown to prevent MA induced mitochondrial inhibition and microglial activation (Thomas and Kuhn, 2005a). Pretreatment with the NO synthase inhibitor, 7-Nitroindazole, has been shown to prevent MA induced depletions of DA in mice (Itzhak and Ali, 1996). Similarly, NO synthase knockout mice display resistance to MA induced DA depletions (Itzhak et al., 1998). Additionally, treatment with the peroxynitrite scavenger, 5,10,15,20-tetrakis (2,4,6-tri-methyl-3,5-sulphonatophenyl) porphinato iron III (FeTMPyP), has been shown to prevent or attenuate several aspects of MA toxicity including hyperthermia, DA depletions, and mitochondrial inhibition, demonstrating the

important roles of NO and RNS in MA toxicity (Imam et al., 1999; Brown et al., 2005).

This MA induced increase in glutamate is thought to occur indirectly as a result of increased GABAergic transmission from the striatum to the substantia nigra pars reticulata, reducing GABAergic signaling to the thalamus, disinhibiting thalamocortical glutamate release and increasing glutamatergic transmission via corticostriatal pathways (Mark et al., 2004). Microdialysis experiments have demonstrated increased extracellular GABA in the substantia nigra pars reticulata during acute neurotoxic doses of MA (Mark et al., 2004). Seven days after this drug administration procedure, increased levels of glutamic acid decarboxylase (GAD65) mRNA were found in the striatum, suggesting increased GABA synthesis consistent with increased GABAergic transmission (Mark et al., 2004). Altered presynaptic GABA immunoreactivity has also been demonstrated in the striatum and globus pallidus following a neurotoxic dose of MA (Burrows and Meshul, 1999). In this experiment, in both the globus pallidus and striatum, there was an initial decrease in presynaptic GABA seven days after drug administration, followed by an increase in presynaptic GABA four weeks after administration. These findings are consistent with increased GABA release followed by compensatory changes in synthesis to accommodate the increased GABAergic outflow (Burrows and Meshul, 1999).

Changes in glutamate and GABA levels have been shown to alter brain iron metabolism. The ability of glutamate to stimulate NO production in the

striatum could directly activate the IRP/IRE system, leading to an increase in the expression of DMT-1 and the transferrin receptor and decreases in the expression of ferritin, resulting in increased iron accumulation (Weiss et al., 1993; Pantopoulos et al., 1996). In cultured neurons, NMDA activation has been shown to increase iron uptake via increased NO production and subsequent interactions with DMT-1 (Cheah et al., 2006). In rats, glutamate injections in the substantia nigra resulted in increased striatal iron content and DMT(-IRE) expression several hours after injection (Wang et al., 2010). Injection of other excitatory amino acids, including quinolinate, ibotenate and kainate, into the striatum of rats has been shown to cause a delayed (1 month) increase in iron levels in areas receiving GABAergic output from the striatum, including the substantia nigra pars reticulata and the globus pallidus (Shoham et al., 1992; Sastry and Arendash, 1995). This pattern of iron accumulation is very similar to the one seen in vervet monkeys treated with MA (Brown et al., 2005; Melega et al., 2007) and suggests a relationship between alterations in GABAergic outflow from the striatum and increased iron accumulation. There is a high degree of anatomical similarity between brain regions that receive GABAergic projections and those that accumulate high levels of iron, however, the mechanisms underlying this relationship are not known. Inhibition of GABA catabolism by injecting the GABA-transaminase inhibitor, vigabatrin, into the striatum and pallidum was shown to reduce iron levels in the ventral pallidum, globus pallidus and substantia nigra; however, it is not clear if this result was due to an overall increase in GABA levels
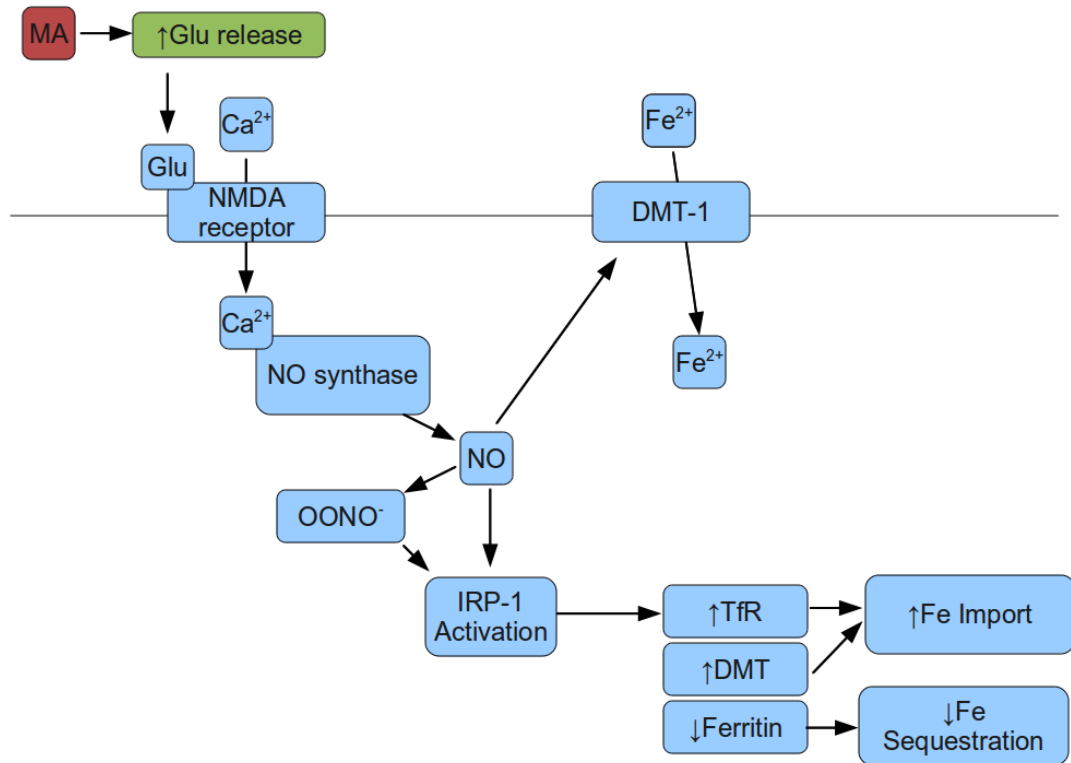
Figure 7: Hypothetical model of glutamate mediated alterations in iron regulation in response to MA.
Glutamate binds to NMDA receptors within the striatum, increasing calcium influx into the cells. This calcium increase stimulates nitric oxide (NO) synthase and leads to the production of NO. NO interacts with DMT-1 and stimulates iron import. NO is also capable of activating IRP-1 to increase the expression of iron import proteins. Ca2+=calcium; DA=dopamine; DMT-1=divalent metal transporter 1; Fe=iron; Glu=glutamate; IRP-1=iron regulatory protein 1; MA=methamphetamine; NMDA=N-methyl-D-aspartate; O=nitric oxide; OONO-=peroxynitrite; TfR=transferrin receptor; VMAT2= vesicular monoamine transporter 2.

or a decrease in GABA degradation or due to another nonspecific effect of

vigabatrin (Perry et al., 1979; Hill, 1985).[1] If it was due to a decrease in GABA

---

1. In addition to reducing iron accumulation (Hill, 1985), vigabatrin has also been shown to decrease DA release in the nucleus accumbens, attenuate decreases in TH activity in response to MA and block MA triggered reinstatement of conditioned place preference (Gerasimov et al., 1999; DeMarco et al., 2009). These findings have lead to the suggestion that vigabatrin might be a useful treatment for MA users (Brodie et al., 2005; Garza et al., 2009).

catabolism, an MA induced increase in GABA outflow may result in increased GABA degradation and increased iron accumulation. While the specific mechanisms underlying the relationship between GABA utilization and iron accumulation remain unknown, MA induced changes in GABA metabolism may have a direct effect on iron accumulation in regions receiving GABAergic outflow as suggested by the Melega et al. (2007) study. In addition, MA induced glutamate release could also lead to increased iron accumulation within the striatum through increased NO production as shown in **Figure 7**.

Microglial activation

MA administration has been shown to activate microglia and this process may be associated with increased brain iron content (LaVoie et al., 2004; Thomas et al., 2004b; Sekine et al., 2008). Microglia serve as phagocytic immune cells in the brain that become activated in cases of brain injury and inflammation. While the roles of microglia include several beneficial processes that facilitate regeneration and repair, there is also growing evidence that overactive microglia can contribute to neurotoxicity through their release of ROS and RNS (Block et al., 2007). In rats and mice, neurotoxic dosing regimens of MA have been shown to produce microglial activation in the striatum and in cortical and brainstem regions (LaVoie et al., 2004; Thomas et al., 2004b, a). This increase in microglial activation may precede some aspects of MA toxicity and has been proposed to be a contributing factor to MA induced damage (LaVoie et

al., 2004; Thomas et al., 2004a). In these animal models, microglial activation has been shown to peak 48 hours after MA administration and then subside and return to control levels after seven days (Thomas et al., 2004a). Interestingly, repeated administration of MA after an initial dosing several days before results in an attenuated microglial response suggesting a potential relationship between the microglial response and the development of tolerance to MA toxicity (Thomas and Kuhn, 2005b) or alternatively, an altered immune response (Buchanan et al., 2010). In humans, increased levels of activated microglia have been reported in abstinent MA users using the PET radiotracer [11C](R)-PK11195, suggesting sustained microglial activation (Sekine et al., 2008). Increased binding of this tracer was seen in all regions analyzed, including the striatum, midbrain, thalamus, insular cortex and orbitofrontal cortex (Sekine et al., 2008). Increased microglial activation may also be related to the findings of increased echogenicity in the substantia nigra of stimulant users (Block et al., 2007; Todd et al., 2013)as postmortem studies have shown positive correlations between microglial activation and substantia nigra echogenicity (Berg et al., 2010). In contrast, a recent postmortem study of chronic MA users who died of MA intoxication found an increase in microglia number in the striatum, but failed to detect a significant increase in activated microglia levels (Kitamura et al., 2010).

MA induced microglia activation may cause alterations in iron handling and storage. Microglial activation may be the result of MA induced increase in DA quinones (LaVoie and Hastings, 1999; Miyazaki et al., 2006), which have been

shown to activate microglia in vitro (Kuhn et al., 2006). Activation might also be secondary to increased glutamate signaling as NMDA antagonists have been shown to attenuate this microglial activation (Thomas and Kuhn, 2005a). Activated microglia attracted to areas of MA toxicity could cause a redistribution of iron in the brain as microglia contain high levels of ferritin and iron (Kaneko et al., 1989; Connor et al., 1990; Jellinger et al., 1990). Migration of iron loaded monocytes across the BBB to regions of MA induced damage could also represent a mechanism of increased brain iron delivery (Weinstein et al., 2010). Increased levels of ferritin positive microglia have been shown to be associated with degenerated DA neurons in Parkinson's disease, however, it is unknown whether this association is causative of or in response to cellular damage (Jellinger et al., 1990). The high levels of microglial iron are linked to the microglial ability to produce and release ROS and RNS (Rathnasamy et al., 2011). Uptake of these reactive compounds by neurons or glia could activate the IRP/IRE system and signal for increased iron uptake (Rathnasamy et al., 2011). Additionally, superoxide released from activated microglia has been shown to be capable of releasing iron from ferritin (Yoshida et al., 1995; Yoshida et al., 1998), potentially promoting the production of additional oxygen free radicals. These studies suggest that MA induced microglial activation may be associated with alteration in iron handling and storage as shown in **Figure 8.**

Blood brain barrier disruption

The blood brain barrier (BBB) represents an important mechanism to regulate brain iron influx and efflux and MA has been shown to disrupt BBB function in both in vitro and in vivo models (Kiyatkin et al., 2007; Ramirez et al.,
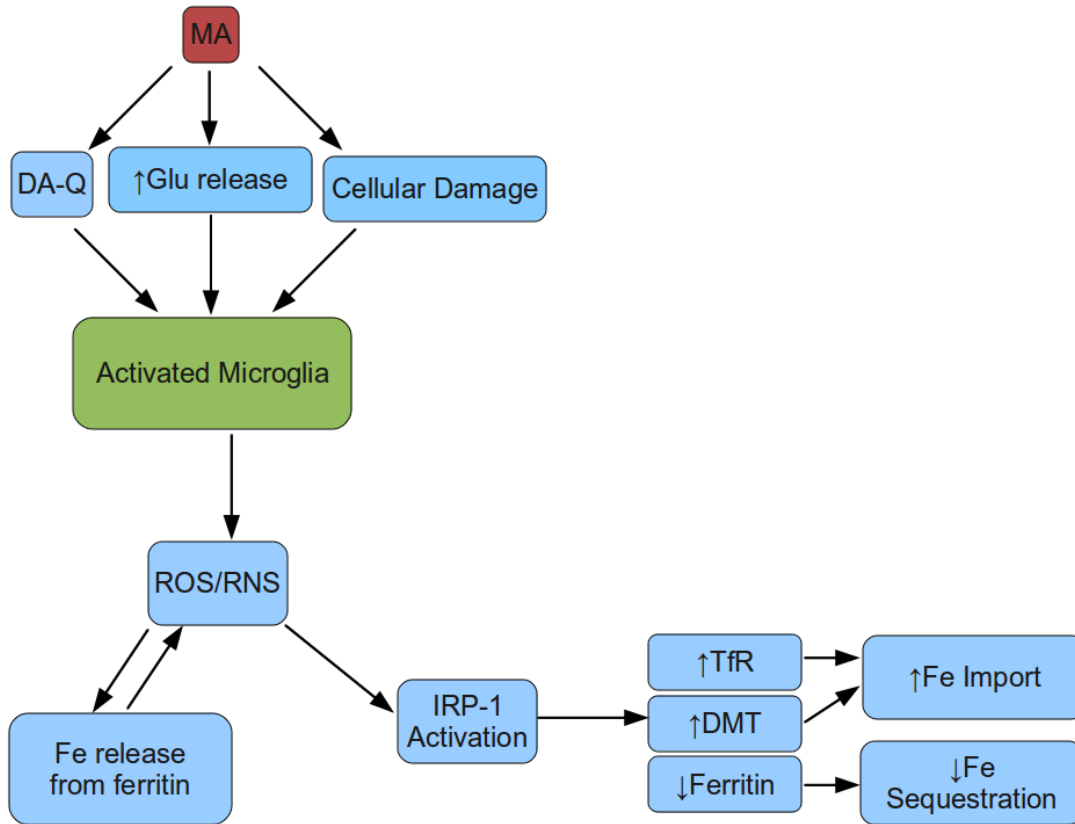
Figure 8: Hypothetical model of alterations in iron regulation in response to MA induced microglial activation.
Microglial activation may be the result of MA induced increase in DA quinones, increased glutamate signaling or a generalized response to MA induced cellular injury. Activated microglia release a variety of ROS and RNS, including superoxide, which is capable of releasing iron from ferritin. These reactive compounds could activate the IRP system and signal for increased iron uptake. DA-Q=dopamine quinones; DMT=divalent metal transporter; Fe=iron; Glu=glutamate; IRP-1=iron regulatory protein 1; MA=methamphetamine; RNS=reactive nitrogen species; ROS=reactive oxygen species; TfR=transferrin receptor.

2009; Sharma and Kiyatkin, 2009; Muneer et al., 2011; Northrop and Yamamoto, 2012; Park et al., 2012; Toborek et al., 2013). Under normal conditions, brain iron uptake is regulated primarily by transferrin receptor mediated transfer through brain capillary endothelial cells (Zecca et al., 2004; Moos et al., 2007; Mills et al., 2010; Weinreb et al., 2013). There is also evidence of transferrin independent mechanisms operating as well (Beard et al., 2005; Mills et al., 2010). Studies using brain microvascular endothelial cells that are devoid of monoaminergic cells to model BBB function have shown that MA is capable of down regulating tight junction proteins, increasing monocyte migration and increasing ROS (Ramirez et al., 2009; Muneer et al., 2011; Park et al., 2012). The increase in oxidative stress may be due to activation of NAD(P)H oxidase and inhibition of this enzyme was shown to reduce ROS production, monocyte migration and tight junction protein alterations (Park et al., 2012). Similar attenuations of BBB disruption were also seen with antioxidant treatment, suggesting a critical role of ROS in BBB disruption (Ramirez et al., 2009). In mice, MA has been shown to increase BBB permeability, increase brain capillary superoxide levels, and reduce tight junction proteins and many these effects were attenuated with antioxidant treatment (Ramirez et al., 2009; Toborek et al., 2013). In rats, several studies have shown that acute doses of MA increase BBB permeability and cause edema (Kiyatkin et al., 2007; Sharma and Kiyatkin, 2009; Kousik et al., 2011; Northrop and Yamamoto, 2012). In many of these models, BBB disruption was shown to be closely associated with MA induced hyperthermia (Kiyatkin et

al., 2007; Sharma and Kiyatkin, 2009). Additionally, there may be a synergistic effect of repeated unpredictable stress and MA treatment on measures of BBB function (Northrop and Yamamoto, 2012).

MA induced BBB disruption may cause alterations in iron accumulation by increasing brain uptake of iron. Disruption of the BBB has been used to deliver iron based contrast agents into the CNS (Muldoon et al., 2005; Ramirez et al.,
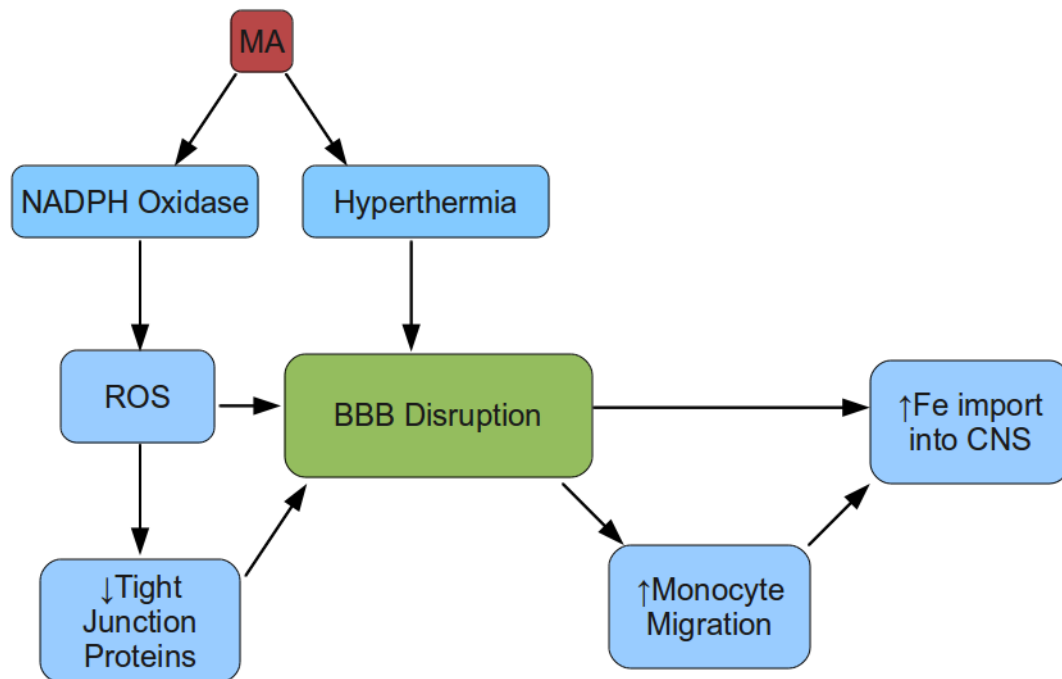
Figure 9: Hypothetical role of blood brain barrier (BBB) disruption in MA induced iron accumulation.
MA induced BBB disruption has been associated with increased NADPH oxidase activity resulting in increased ROS in brain capillary endothelial cells. This leads to a reduction in tight junction proteins which increases BBB permeability. MA induced hyperthermia has also been shown to be involved in causing BBB disruption. A compromised BBB may allow for increased iron import into the CNS. Additionally, BBB dysfunction combined with MA toxicity may promote the migration of iron containing monocytes into the CNS. BBB=Blood Brain Barrier; CNS=central nervous system; Fe=iron; MA=methamphetamine; ROS=reactive oxygen species.

2009; Ramirez et al., 2009; Muneer et al., 2011; Muneer et al., 2011; Park et al., 2012; Park et al., 2012)and conversely, iron based contrast agents have been used to assess BBB function and permeability (Weinstein et al., 2010). Transgenic mice that express interleukin-6 in astrocytes display a permanent BBB defect that is associated with increased brain iron accumulation (Castelnau et al., 1998). Disruption of the BBB by MA may also be associated with increased monocyte migration which could introduce excess iron to the CNS and provide an additional source of oxidative stress. BBB disruption has been proposed as a source of increased brain iron accumulation in Parkinson's disease (Gerlach et al., 2006), 6-OH-DA toxicity (Oestreicher et al., 1994), and neuroleptic treatment (Leenders et al., 1994) and studies in preclinical models suggest that BBB leakage may be a source of increased iron in MA toxicity as well as shown in **Figure 9**.

Iron as a source of toxicity

As we have seen, there are several possible mechanisms by which MA could alter brain iron handling, making increased iron accumulation a potential biomarker of MA toxicity. However, even without an increase in iron accumulation, brain iron may still contribute to MA toxicity through its ability to promote and catalyze the formation of highly reactive oxygen species as well as reactive DA quinones (Sulzer and Zecca, 2000). MA causes a dramatic release of DA from intracellular vesicles and nerve terminals; and this increase in DA

35

concentration may be capable of releasing iron from ferritin, increasing the labile pool of iron (Double et al., 1998). Evidence that this labile iron directly contributes to MA toxicity can be inferred from studies which use iron chelators to prevent markers of MA induced damage (Yamamoto and Zhu, 1998; Park et al., 2006). Rats pretreated with the iron chelator deferroxamine show attenuated levels of DA and 5-HT depletion after a neurotoxic dosing schedule of MA (Yamamoto and Zhu, 1998; Park et al., 2006). Similarly, rats pretreated with deferroxamine also show reduced levels of hyperthermia, reduced measures of lipid peroxidation, and reduced locomotor stimulation in response to MA (Park et al., 2006). Pretreatment with deferroxamine has also been shown to reduce measures of oxidative stress caused by d-amphetamine administration in rats (Valvassori et al., 2008). Additional evidence that iron enhances MA toxicity has been shown in cell culture models, in which co-administration of MA with iron to human mesencephalic neuron derived cells significantly increased neurite disintegration and cell death compared either treatment alone (Lotharius et al., 2005).

The role of free iron in MA toxicity may reflect a general feature of compounds which cause neurotoxicity to dopamine neurons. Indeed, pretreatment with deferroxamine attenuates the neurotoxicity of most dopaminergic toxins, including MPTP (Lan and Jiang, 1997; Matarredona et al., 1997; Kaur et al., 2003), rotenone (Xiong et al., 2012), 6-OHDA (Ben-Shachar et al., 1991; Youdim et al., 2004), and lactacystin (Zhang et al., 2005; Zhu et al., 2007). In addition, increasing brain iron content through dietary supplementation

has been shown to exacerbate the neurtoxicty of MPTP (Double et al., 1998; Kaur et al., 2007)and paraquat (Peng et al., 2007). While the mechanisms of toxicity in these different models do vary, they share a common cascade of events with MA toxicity including increases oxidative stress, proteosome impairment, mitochondrial inhibition and altered iron metabolism. These experiments suggest that iron may not only be a biomarker of DA toxicity in MA abuse, but may also play a key role in the general pathways that lead to dopaminergic neurotoxicity.

Conclusions

Emerging evidence suggests that brain iron accumulation plays an important role in MA toxicity, both as a biomarker of damage and a source of increased oxidative stress. Acute doses of MA have been shown to increase iron accumulation in non-human primates (Melega et al., 2007). There is also evidence from ultrasound measurements that stimulant users have altered substantia nigra morphology that is consistent with increased iron (Todd et al., 2013). The effects of MA could induce alterations in iron metabolism via several mechanisms. MA increases cytosolic concentrations of DA by destabilizing the vesicular storage of DA through its action on the VMAT2. This redistribution is followed by excess degradation of DA in the cytosol, leading to the production of H_2O_2, DA quinones, and other ROS. This increased oxidative stress could activate IRP-1 and lead to an increase in the expression of iron import proteins,

transferrin receptor and DMT, and a decrease in the iron sequestering protein, ferritin. ROS would also cause oxidative damage to functional groups on proteins, increasing demand on the ubiquitin proteasome system to degrade these proteins and impairing its ability to degrade IRP-2. Reactive DA metabolites are also capable of inhibiting complexes within mitochondria, causing functional iron deficits within mitochondria that lead to increased expression of iron import proteins. Nonenzymatic degradation of DA in the setting of increased levels of H_2O_2 and iron may allow for the formation of the highly reactive DA metabolite, 6-OHDA, which is capable of directly releasing stored iron from ferritin and has been shown to increase iron accumulation. The damaged neurons and glia release factors that activate and attract microglia to surround the injured cells. Activated microglia express high levels of ferritin that could be capable of safely sequestering some of the excess iron from degenerating cells, however, this process may also concentrate local brain iron concentrations to areas of damage. Activated microglia also release reactive oxygen and nitrogen species to the area increasing the oxidative stress. Finally, MA has been shown to disrupt the blood brain barrier and this may facilitate iron transport from systemic circulation into the central nervous system.

Unfortunately, the degree to which these processes occur in human MA users is largely unknown. Many of the studies that investigate mechanisms of MA toxicity use an acute neurotoxic dosing schedule that is typically four 5-10 mg/kg doses spaced out over 6-8 hours in drug naïve animals (Davidson et al., 2001;

Cadet et al., 2003; Cadet et al., 2011). It has been suggested that this approach may more accurately model an accidental MA overdose as opposed to effects from chronic MA abuse (Davidson et al., 2001). Other animal models using escalating doses over longer periods of time often see attenuation of some of the measures of MA neurotoxicity and this may represent a more accurate version of the changes that would be seen in human MA users (Cadet et al., 2011). While there is evidence that some of these processes (e.g. oxidative stress, proteasome impairment and microglial activation) do occur in human MA users, most of this evidence comes from postmortem cases of fatal MA overdoses, making it difficult to generalize these results to chronic MA users. Therefore, there is a need to utilize in vivo methods to investigate brain iron accumulation in human MA users to elucidate the relevance of these preclinical findings.

Imaging brain iron content

Introduction

Growing evidence suggests that brain iron accumulation may play a role in a number of neurological and psychiatric disease conditions both as a biomarker of damage and a potential source of increased oxidative stress (Schenck and Zimmerman, 2004). Magnetic Resonance Imaging (MRI) provides several noninvasive methods to investigate this possibility (Dusek et al., 2013). Iron is paramagnetic, and its presence shortens the transverse relaxation time constant (T_2) of nearby water protons causing a loss of signal intensity on T_2-weighted images. Measuring this effect using quantitative imaging techniques can be used to investigate the spatial distribution of iron in the brain. These techniques have been used in several studies to investigate brain iron accumulation in healthy aging (Bartzokis et al., 1997; Martin et al., 1998; Bartzokis et al., 2007a; Xu et al., 2008; Pfefferbaum et al., 2009), Multiple Sclerosis (MS) (Ceccarelli et al., 2009), and several neurodegenerative diseases (Bartzokis et al., 1994; Atasoy et al., 2004; Ding et al., 2009) and have been validated in postmortem studies in both humans (Langkammer et al., 2010) and nonhuman primates (Hardy et al., 2005). In this chapter, I will review basic MRI concepts that can be applied to measuring brain iron content with a focus on T_2 based methods and discuss the development of a novel approach to create parametric maps of iron distribution.

40

Magnetic resonance imaging contrast mechanisms

MRI allows researchers to investigate extensive properties of the brain, such as anatomical structure and volume, and intensive properties of brain tissue composition, which include water content, chemical components (using MR spectroscopy) and the concentration of paramagnetic substances like iron. The vast majority of MR neuroimaging applications are based on the signal from protons (^{1}H) contained in water. As we will see, this signal can be strongly affected by small variations in the physical properties of the surrounding tissue that interacts with these protons. By taking advantage of these effects, MRI can produce detailed images that highlight and contrast specific differences in brain tissue composition. The major mechanisms for producing these tissue contrasts include longitudinal (T_1) and transverse (T_2 and $T_2{}^*$) relaxation and proton density (PD); yielding images that are weighted based on one or more of these contrast mechanisms (e.g. T_2-weighted image)(see **Figure 10**).

Protons (^{1}H) have a net magnetic moment and in the presence of a strong magnetic field ($\mathbf{B}_0$), they will precess at the Larmor frequency (ω), which is defined as the product of the gyromagnetic ratio (γ) of the proton ($\gamma = 267.513 \times 10^6$ rad s^{-1} T^{-1} or $\gamma/2\pi = 42.576$ MHz T^{-1}) and the strength of the field ($\mathbf{B}_0$), $\omega = \gamma \mathbf{B}_0$. These spinning protons will align themselves to the field either parallel to the direction of $\mathbf{B}_0$ (conventionally termed, z) or antiparallel to the field (-z). These two states are very stable; and at first, equal proportions of nuclei will occupy

41
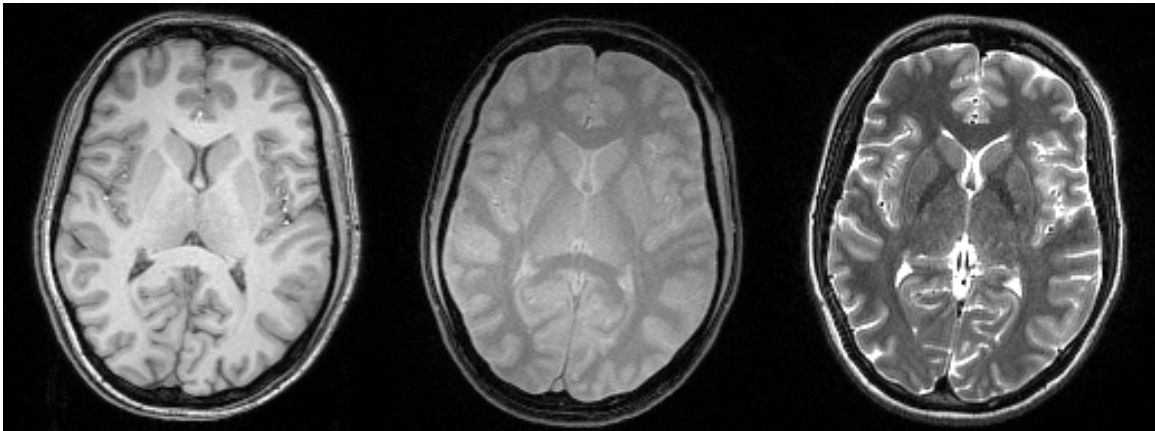
Figure 10: Examples of Magnetic Resonance Imaging Tissue Contrast.
From left to right: T_1, proton density and T_2-weighted images acquired at 3 Tesla. T_1 images provide excellent contrast between gray matter and white matter and are often used to highlight anatomical features of the brain. Both proton density and T_2 weighted images can be used to identify areas of edema, which appear bright or hyperintense on these scans. In addition, T_2 weighted images can also be used to identify areas of iron accumulation that result in signal hypointensities.

each state. However, over time, slightly more nuclei will orient themselves in the parallel direction due to the slightly lower energy associated with this orientation; resulting in a net magnetic moment in the direction of z. The excess nuclei that are spinning parallel to $\mathbf{B_0}$ create a net magnetic moment in the direction of $\mathbf{B_0}$ (z), termed $\mathbf{M_0}$. The magnitude of $\mathbf{M_0}$ at a given field strength is proportional to the number of protons in the sample and this determines the maximum possible MRI signal (S_0) from a given sample ($S_0 \propto M_0$). In the brain, this is proportional to the fractional water content of the tissue, giving rise to the contrast known as proton density (PD).

The process of $\mathbf{M_0}$ reaching its full magnitude along z is termed longitudinal or T_1 relaxation. It is due to the spinning nuclei gradually exchanging

42

their excess energy with the surrounding "lattice;" molecules that act as thermal sinks. The time it takes this process to reach thermal equilibrium state can be quantified by the following exponential equation:

$$M_z(t) = M_0 - \left[M_0 - M_z(0) \right] e^{\left(\frac{-t}{T_1} \right)} \tag{1}$$

M_z *(t)* represents the magnitude of the net magnetic moment in the direction of *z* at time *t*, M_0 represents the magnitude of the net magnetic moment in the direction of *z* at equilibrium and T_1 represents the time constant to reach equilibrium. As we will see, T_1-weighted MRI sequences are often used to create high resolution anatomical images of the brain, taking advantage of the fact that the longitudinal relaxation rate constant ($R_1 \equiv 1/T_1$) of white matter is greater than the rate for gray matter at all clinically approved MRI field strengths (Rooney et al., 2007)[2].

The magnitude of $\mathbf{M_0}$ at equilibrium is very small relative to the main external field $\mathbf{B_0}$, and this makes it very difficult to detect $\mathbf{M_0}$ in the z direction. However, by applying a radio frequency (RF) pulse at the resonant frequency of these protons (ω), it is possible to rotate this magnetization away from the parallel axis (z) and into the transverse (*x,y*) plane. Applying an excitation pulse sufficient to tilt the magnetization vector perpendicular to the *z* axis (a 90º pulse) results in a magnetization vector with magnitude equal to $\mathbf{M_0}$ rotating in the

---

[2] Exceptions to this statement include areas of white matter disease, such as in seen in Multiple Sclerosis, and in studies of infants less than 8 months old who have not yet fully myelinated their white matter tracks (Barkovich, 2005).

transverse plane around *z* at the Larmor frequency (ω). If an RF coil is placed perpendicular to the *x, y* plane, this rotating magnetization will induce a periodic change in the voltage of that coil, allowing the magnetization in the *x,y* plane (**M**$_{x,y}$) to be detected. Immediately after the pulse, the excited nuclei rotate in phase with each other. However, as the spinning nuclei interact they slightly modify the total local magnetic field they are experiencing, causing them to change their angular velocity slightly (recall *ω=γ**B**$_0$*). After this interaction, the nuclei begin spinning at the same angular velocity once again, but now they have slightly different phases. These spin-spin interactions lead to a gradual dephasing of the spins in the transverse plane and a reduction of the net magnetic moment in the *x,y* plane due to incoherent summation. This transverse relaxation follows an exponential decay given by the equation:

$$M_{x,y}(t) = M_0 e^{\left(\frac{-t}{T_2}\right)} \tag{2}$$

where **M**$_{x,y}$ *(t)* represents the magnitude of the magnetic moment in the x,y plane at time t after excitation; **M**$_0$ represents the magnitude of the net magnetic moment in the direction of z immediately prior to excitation; and T$_2$ represents the time constant of the decay. In practice, the decay of **M**$_{x,y}$ is much faster than predicted by spin-spin interactions alone, because local field inhomogeneities also contribute to the dephasing of spins in the transverse plane in a process termed T$_2$* relaxation. The rate constant of T$_2$* effects (1/T$_2$*≡R$_2$*) can be represented by the sum of the relaxation rate constant of the spin spin

44
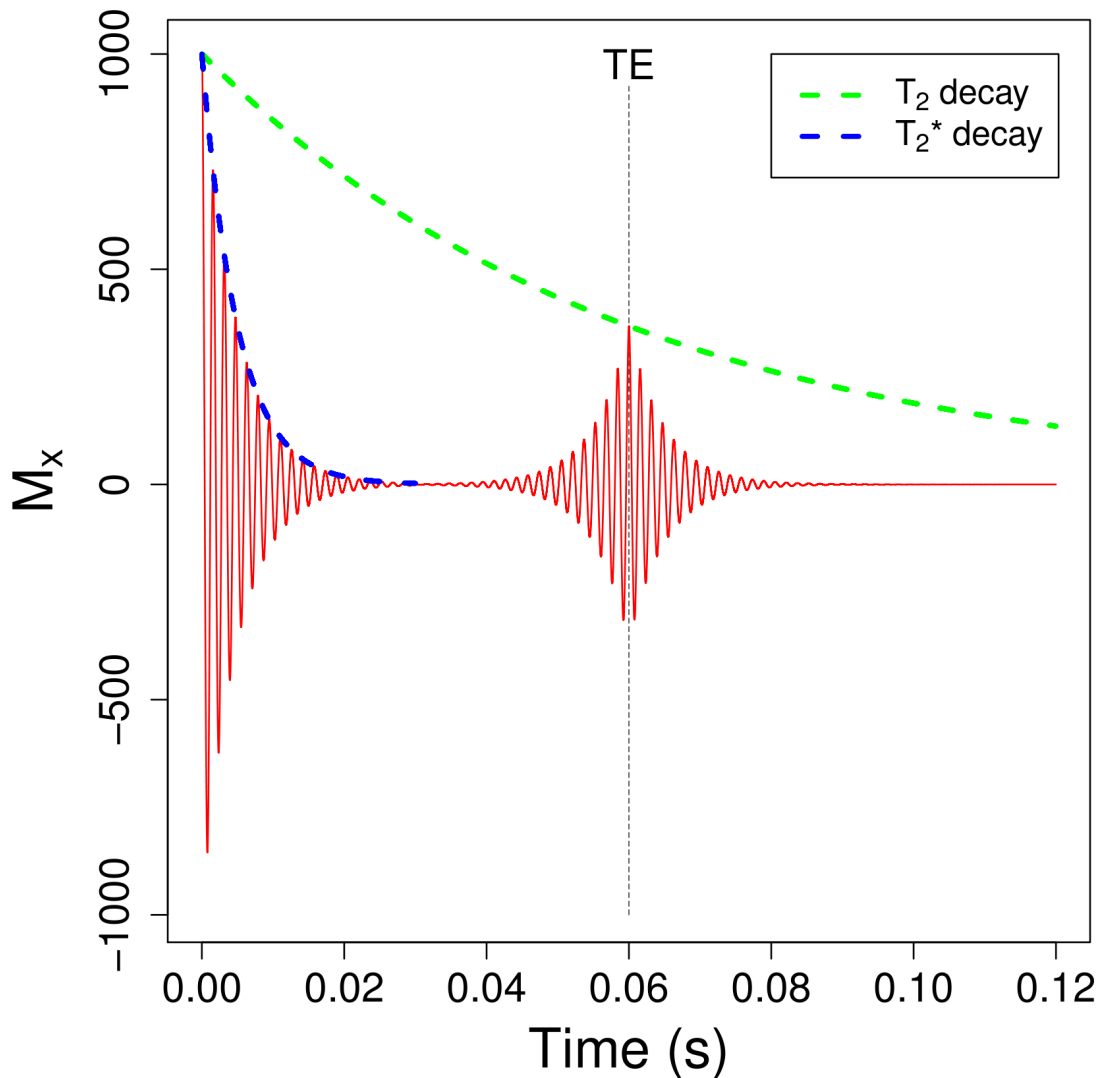
Figure 11: T_2 and T_2* decay.
T_2* decay is caused by a combination of spin spin interactions and local field inhomogeneities that both lead to dephasing of spins in the transverse plane. Using a 180º radio frequency pulse at time, TE/2, it is possible to reverse the effects of decay due to field inhomogeneities and refocus the coherence of spins in the x,y plane, creating a spin echo. The magnitude of this spin echo will reflect the irreversible dephasing due to T_2 decay. In this example, T_2*=0.005s and T_2=0.06s, TE=0.06s, M_0=1000 arbitrary units. M_x=magnetization in x; TE=echo time.

interactions $(1/T_2 \equiv R_2)$ plus the rate constant due to local field inhomogeneities (R_2'); therefore R_2^* is always greater than or equal to R_2. However, it is possible to reverse the effects of decay due to field inhomogeneities and refocus the coherence of spins using a 180º RF pulse, creating a spin echo as shown in **Figure 11**. The magnitude of the echo will reflect the irreversible dephasing due to spin-spin interactions, thus providing an approach to measure T_2 in the presence of an inhomogeneous magnetic field. T_2-weighted MRI images are often used to detect neuropathology that results in an excess of tissue water (edema), which reduces the rate of transverse relaxation and produces the so-called T_2 hyperintensities, such as those associated with white matter lesions in patients with MS. These same scans can also be used to detect the presence of agents which facilitate T_2 relaxation, such as iron.

Iron and relaxation parameters

Iron is paramagnetic; it becomes magnetized in the presence of a magnetic field and thus has positive magnetic susceptibility (Schenck, 2003; Dusek et al., 2013). At higher magnetic fields, the induced magnetization of iron is increased (Bartzokis et al., 1993; Schenck, 2003). In contrast, most other tissue components are primarily diamagnetic; they reduce the magnetization of the field and have negative susceptibility. Most of the iron in the body is contained within hemoglobin. In its oxygenated form hemoglobin is diamagnetic, however, when it is de-oxygenated, it becomes paramagnetic and this forms the

basis for Blood Oxygen Level Dependent (BOLD) contrast used in functional MRI studies (Ogawa et al., 1992). Of the remaining tissue (or "non-heme") iron, most is stored within ferritin and its breakdown product, hemosiderin (Hallgren and Sourander, 1958). Ferritin is composed of a protein shell surrounding a core of iron in the form of ferrihydrite ($5Fe_2O_3$-$9H_2O$) that can store as many as 4500 iron atoms (Schenck and Zimmerman, 2004). In tissue with high concentrations of iron, such as the basal ganglia regions, ferritin is capable of enhancing both the transverse and longitudinal relaxation rates of water protons. Other non-heme iron containing molecules and other non-heme sources of iron, such as transferrin and non-bound iron, are not found in high enough concentrations in tissue to affect relaxation (Schenck, 2003). This ability to enhance relaxation is termed relaxivity and is denoted by a little "r" (r_{2Fe} and r_{1Fe}). The relaxivity of ferritin iron can be expressed as a linear model as follows:

$$\frac{1}{T_i} = R_i = R_i^0 + r_{iFe}[Fe] \tag{3}$$

Where i denotes either 2 or 1 for transverse (T_2) or longitudinal (T_1) relaxation; R_i^0 represents the relaxation rate constant due to factors other than iron, such as the relative water and macromolecular content; and r_{iFe} represents the relaxivity due to ferritin iron concentration [Fe]. The relaxivity of ferritin iron is more pronounced on T_2 relaxation compared to T_1 relaxation (Vymazal et al., 1999). Protons near a ferritin cluster are dephased without requiring direct interaction with the iron ions through the outer sphere mechanism (Schenck, 2003). Although the effects of

ferritin iron on T_1 relaxation are relatively small, they have been demonstrated for brain tissue (Vymazal et al., 1996; Rooney et al., 2007). For T_2 measurements, postmortem studies in both humans (Langkammer et al., 2010) and nonhuman primates ((Schenck and Zimmerman, 2004; Schenck and Zimmerman, 2004; Hardy et al., 2005)have validated the linear relationship between iron concentration and R_2. In addition, several studies have shown a similar relationship using literature values of brain iron content (see Table 5 in (Haacke et al., 2005)). This relationship is particularly strong within subcortical gray matter regions, however, for the case of T_1, it has been argued that this relationship could also be due to differences in relative water content and macromolecules (Gelman et al., 2001). Expanding the relaxivity model to include a term for the effects of macromolecules on tissue relaxation rates has been shown to significantly improve the fits of these models for T_1 and T_2 measurements (Rooney et al., 2007; Mitsumori et al., 2009).

$$\frac{1}{T_i} = R_i = R_i^0 + r_{if_M} f_M + r_{iFe}[Fe] \tag{4}$$

In this expanded model proposed by Rooney et al. (Rooney et al., 2007) for T_1 relaxation and later applied to T_2 relaxation by Mitsumori et al. (Mitsumori et al., 2009), R_i^0 represents the relaxation rate constant of pure saline; and r_{ifM} represents the relaxivity due to the macromolecular volume fraction, f_M, is defined as 1 – fractional water content (f_W), ($f_M = 1 - f_W$). The r_{ifM} term could be further expanded to account for differences in the macromolecular composition

associated with different tissue types such as those associated with gray matter and white matter. The model could also include terms for other factors that also enhance relaxation such as contrast agents that are administered clinically or experimentally; or other paramagnetic elements that could be present in sufficient quantities in certain pathological conditions, such as manganese poisoning.[3] However, under normal circumstances, the model in **equation 4** accounts for the majority of the variance in relaxation measurements. Thus, the relaxation rate constants, above those seen in saline, can be thought of as the linear combination of relaxivity effects due to iron and macromolecular content.

T_2 weighted signal intensity

In a T_2-weighted image acquired at a single echo time (TE), the signal intensity (S) of a voxel at location x,y reflects both T_2 and M_0 ($S_0 \propto M_0$) at that location, according to equation:

---

3. The possible role of manganese poisoning is especially relevant in the context of this dissertation examining the effects of methamphetamine on brain iron content, because the illicit use of the closely related stimulant, methcathinone, the beta ketone of methamphetamine, has been associated with manganese induced parkinsonism; resulting in dramatic enhancement of T_1 weighted MRI signal within the globus pallidum (de Bie et al., 2007, Sikk et al., 2007, (Stepens et al., 2008)Sikk et al., 2013). These cases of methcathinone associated manganese poisoning are believed to be due to the presence of manganese in methcathinone preparations as opposed to a result of methcathinone itself. The illicit synthesis of methcathinone uses potassium permanganate and this is likely the source of manganese contamination (Sikk et al., 2007). Although methamphetamine abuse has not been linked with manganese poisoning, polysubstance abuse or drug substitution among stimulant users might put methamphetamine users at a greater risk of methcathinone use and associated manganese toxicity. Unlike an increase in ferritin iron, manganese toxicity would enhance T_1 more than T_2 relaxation.

$$S_{(x,y)}(TE) = S_{0(x,y)} e^{\left(\frac{-TE}{T_{2(x,y)}}\right)} \tag{5}$$

In an image with multiple voxels with similar water content and thus similar proton density, the log of the signal intensity of different voxels will be inversely related to R_2 (**Figure 12**):

$$\ln\left(S_{x,y}(TE)\right) = \ln\left(S_{0(x,y)}\right) + \left(\frac{-TE}{T_2}\right) = -R_2(TE) + \ln\left(S_{0(x,y)}\right) \tag{6}$$

$$if : S_{0(x_1,y_1)} = S_{0(x_n,y_n)}, then : \ln\left(S_{x,y}(TE)\right) = -R_2(TE) + C \tag{7}$$

where C represents the constant value of $\ln(S_0)$. In these cases, voxels with lower T_2-weighted signal intensity values have shorter T_2 (and higher R_2) compared to voxels with higher signal intensity. This relationship provides a basis for using T_2-weighted signal intensity as a surrogate marker for T_2 and R_2 within a
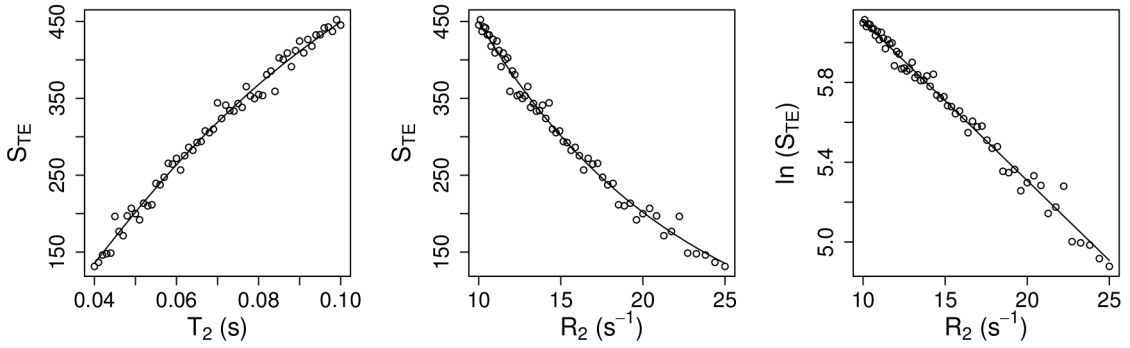
Figure 12: Simulated relationships between T_2, R_2, and signal intensity (S) at a fixed echo time (TE).
In general, S_{TE} is lower for voxels with shorter T_2 and higher R_2. This relationship becomes linear between R_2 and the $\ln(S_{TE})$. The solid line represents this relationship in the absence of noise. The open circles demonstrate the effects of adding Gaussian noise; simulating the degree of deviation from this relationship that could be expected to occur in an image. In this example, S_0 is held constant at 1000 arbitrary units, the standard deviation of the noise (σ) is set to 10, TE = 80 ms and the Signal to Noise Ratio (SNR) = 100 at S_0 (SNR=S_0/σ).

single image. While this approach does not provide an absolute measurement of T_2 or R_2, linear correlations can be found by comparing the log of signal intensity measurements from a T_2 weighted image to calculated R_2 values obtained using images from multiple echoes. However, when applying this technique across subjects, slight differences in coil loading and subsequent RF calibration as well as other differences in hardware or acquisition parameters can also affect the T_2-weighted signal intensity values. Modern MRI scanners often attempt to reduce this variation by adjusting the scaling of signal intensity values. Alternatively, some researchers have used the ratio of signal intensities from two regions to normalize measurements obtained from T_2-weighted images (Tjoa et al., 2005; Brass et al., 2006). Unfortunately, these approaches still result in a somewhat arbitrary scaling of the signal intensity values and qualitative measurements.

Quantifying T_2

In order to obtain quantitative measures of T_2 and R_2, T_2-weighted images need to be acquired at multiple echo times to characterize the decay. As with any MR measurement, the accuracy and precision of T_2 quantification is dependent on the signal to noise ratio (SNR) of the base images and the sampling strategy. The simplest strategy uses only two echo times. As discussed above, taking the log of the signal intensities from these images transforms the mono-exponential decay curve into a linear form from which a slope can be estimated using the following formula:

51

$$R_{2(x,y)} = \frac{ln\left[S_{TE_1(x,y)}\right] - ln\left[S_{TE_2(x,y)}\right]}{\left(TE_2 - TE_1\right)} \qquad (8)$$

where $S_{TE1(x,y)}$ and $S_{TE2(x,y)}$ are the signal intensities of voxel x,y at TE_1 and TE_2, respectively; and TE_2-TE_1 is the difference in echo times in seconds. Adding a third additional echo time allows a mono-exponential T_2 decay to be fit using nonlinear curve fitting on the original (i.e. non-transformed) intensity values. This increases the signal to noise ratio of the fit and increases the precision of the estimate. It also ensures that the residuals of the fit correspond to the actual SNR distribution. In **Figures 13** and **14**, I illustrate the calculation of R_2 maps using both of these approaches.

I conducted a simulation experiment to compare these two approaches using the statistical software package R (R Development Core Team, 2010). In this simulation, I modeled signal intensity values at three echo times (24 ms, 73
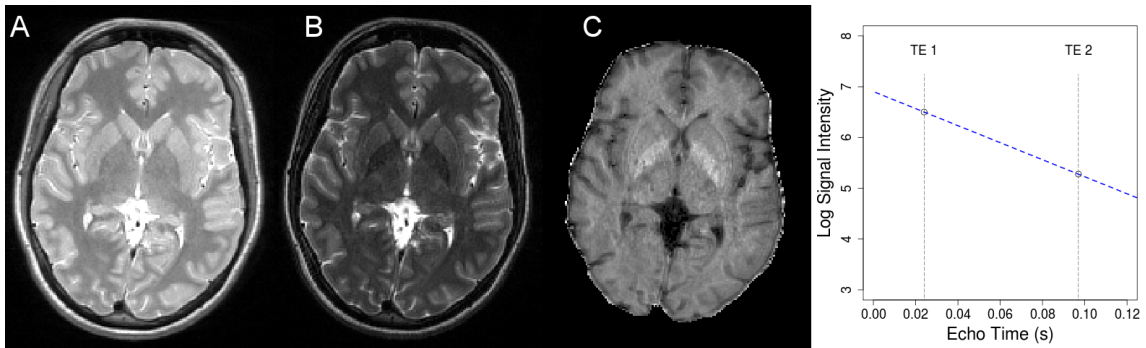
Figure 13: Example of two-point fit used to calculate R_2.
Log transforming the intensity values from the turbo spin echo images, converts the mono-exponential decay into a linear function with a slope equal to -R_2. Therefore, an R_2 map (C) can be calculated using two T_2-weighted images acquired at two different echo times (in this example 24 ms (A) and 97 ms (B) according to **equation 8**. The plot on the right illustrates the slope estimate for a single voxel. The plot on the right illustrates the slope estimate for a single voxel.
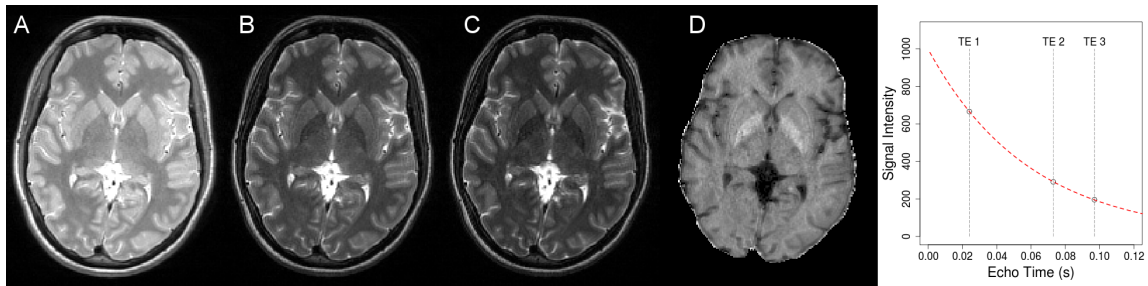
Figure 14: Example of three-point fit used to calculate R_2.
With images from three different echo times (A: 24 ms; B: 73 ms; C: 97 ms), an R_2 map (D) can be calculated by fitting the mono-exponential decay curve described in **equation 5** at each voxel using nonlinear least squares. This three point approach increases the precision of the estimated R_2.

ms, and 97 ms) using a mono-exponential decay with added Gaussian noise, setting M_0 to 1000 and the standard deviation of the noise (σ) to either 10, 7 or 5; corresponding to SNR (S/σ) values of 100, 142.9 (~$100*\sqrt{2}$: an approximation of the SNR increase obtained by acquiring an additional average) and 200. I then fit the mono-exponential decay using either two (the first and last) or three echo times with 1000 replications at every integer T_2 time constant between 20 ms and 100 ms for each SNR condition. In **Figure 15** (left panel), I plotted the standard deviation of these fits normalized to the T_2 value; creating a measure that is similar to a coefficient of variation metric. This simulation demonstrates that the three-point nonlinear fit provides a more precise measure of T_2 compared to the two-point approach at any given base image SNR. It also demonstrates that the two-point method can be just as precise as the three-point approach provided that the base image SNR is high enough. Finally, it illustrates that the precision of these measurements varies with T_2 values and choice of echo times.

In an MRI experiment, there are always compromises between the time of the imaging experiment, SNR, resolution and coverage. (Jones et al., 1996; R Development Core Team, 2010) proposed a strategy to optimize sampling for T_2 measurements given a limited number of sampling times. For a two point approach, they calculated maximum reliability when the first echo was as early as possible and the second echo was collected at 1.11 times the T_2 value. For a three point approach, the maximum reliability was found when the first echo was again as early as possible and the second and third were both at 1.19 times the T_2 value. Having the first echo as early as possible maximizes the SNR of the
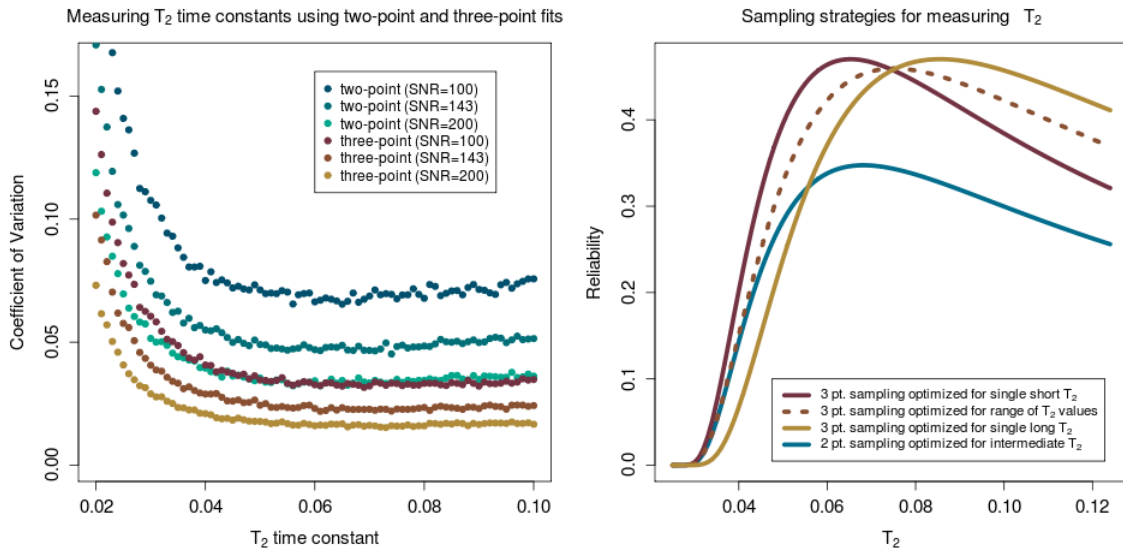
Figure 15: Two-point and three-point measurements of T_2
Left: Coefficient of Variation for two-point and three-point measurements of T_2. At any given signal to noise ratio (SNR), a three-point nonlinear fit has greater precision than a two-point fit using the log transformation. Right: The relative efficiency and fractional reliability of sampling strategies using three-point measurements of T_2. This plot illustrates an experimental sampling scheme designed to optimize T_2 measurement reliability over the range of 55 ms to 100 ms, using TE values of 24,73, and 97 ms.

first image and is clearly desirable. For a variety of technical reasons, it is often not possible to set the first echo at zero and Jones et al. suggest using their calculations from the earliest echo time used.[4] Unfortunately, choosing the optimal later sampling time in both strategies presented by Jones et al. requires prior knowledge of the T_2 value you would like to measure and does not address the situation in which there is a range of T_2 values of interest. The resulting efficiency curves peak near the optimal T_2 value and then fall off. A compromise to this situation for a three point measurement involves setting the second and third echoes to values slightly above both the lowest and highest T_2 values of interest. Using the efficiency equation from Jones et al. for echoes at 24, 73, and 97 ms demonstrates that this strategy results in a more even efficiency across the range of 55 ms to 100 ms (**Figure 15** (right panel)).

---

4. One of the complicating factors is that most T_2 weighted imaging sequences use multiple 180° refocusing pulses to create an image. This approach goes by several names and acronyms including Rapid Acquisition with Relaxation Enhancement (RARE), Fast Spin Echo (FSE) and, on the Siemens system we use, Turbo Spin Echo (TSE) (Hennig1986). The advantage of using multiple 180° refocusing pulses is an acceleration of image acquisition time by a factor equal to the number of refocusing pulses used (the echo train length). However, the complication of these Turbo Spin Echo approaches in the quantification of T_2 arises from the fact that the echoes later in the echo train receive some stimulated echoes from the refocusing pulses in addition to the signal from the primary echo. This results in a curve that deviates from the expected mono-exponential decay, characterized by signal intensity at the first echo that is composed only of the primary echo followed by signal intensities of later echoes that are a combination of the primary and stimulated echoes. One simple solution to this problem is setting the first sampling time to be the second echo of the echo train and fitting the mono-exponential decay to intensity values which are all composed of both primary and stimulated echoes. This results in a very reasonable mono-exponential decay curve.

Quantifying the macromolecular mass fraction

As we have seen, the macromolecular fraction, f_M, also contributes to R_2. Many common pathological processes can lead to decreased f_M, including inflammation, edema, and tissue loss; resulting in signal hyperintensities on T_2-weighted images and reduced R_2 ($1/T_2 \equiv R_2$). In healthy subjects, some researchers have simply used literature values to account for f_M when applying the expanded relaxivity models presented in equation 3 (Rooney et al., 2007; Mitsumori et al., 2009). However, for patient populations, the assumption that f_M will be constant in different regions does not always apply. Furthermore, conditions that could lead to decreased f_M may also be associated with increased iron accumulation and this could potentially cancel out effects seen using an R_2 analysis. Therefore, it is necessary to include an independent measure of f_M when investigating brain iron content.

Recall that the maximum MRI signal is dependent on the number of protons giving rise to the signal, creating the contrast referred to as proton density (PD). In the brain this is proportional to the tissue water fraction (f_W). By using a gradient echo sequence with a very low flip angle combined with a short echo time and short repetition time, such as the Fast Low Angle SHot (FLASH) sequence, it is possible to create an MR image that has minimal effects from T_1 and T_2 relaxation and instead represents a proton density weighting, in which the intensities are proportional to the fractional water (f_W) content in the image.

However, it is important to recognize that effects from saturation and T_2^* decay will still affect these values according to the following equation (Volz et al., 2012):

$$S_{PD} = S_0 \left| \frac{1 - e^{\left(\frac{-TR}{T_1}\right)}}{1 - e^{\left(\frac{-TR}{T_1}\right)} \cos\alpha} \sin\alpha \right| \left(e^{\left(\frac{-TE}{T_2^*}\right)} \right) \tag{9}$$

Where S_{PD} represents the signal of the PD image; α represents the flip angle; TR represents the repetition time; TE represents the echo time; and T_1 and T_2^* are the corresponding relaxation time constants. Using T_1 and T_2^* values from previous studies we conducted at 3T (Berlow et al., 2012b) along with literature values (Jones et al., 1996; Wansapura et al., 1999)and applying this formula to the 3D FLASH sequence we use at 3T (TR = 50 ms, flip angle = 3 degrees, TE = 3.9 ms), results in relative signal reduction equal to approximately 86.1% of $M_0(\sin\alpha)$ in CSF, 89.9% in gray matter and 89.7% in white matter. Since the combined effects of saturation and T_2^* decay are very similar in gray matter and white matter, applying a single correction factor of 1.042 to the CSF intensity values results in relative values that are very closely proportional to the proton density and fractional water content. A simple scaling to the adjusted CSF values then produces an image with values equal to the estimated f_W. In these images, there are also substantial and spatially varying effects of the receiver sensitivity using this sequence. This low spatial frequency variance can be modeled and corrected using a linear combination of Gaussian functions as implemented in the Unified Segmentation approach in SPM 8 (Ashburner and Friston, 2005; Volz

et al., 2012). This 3D FLASH sequence also has relatively low signal to noise and this can be improved using the nonlinear noise reduction algorithm SUSAN, which applies a Gaussian weighted median filter (sigma = 1 mm) within edge defined boundaries (Smith and Brady, 1997). Finally, this map of f_W can be
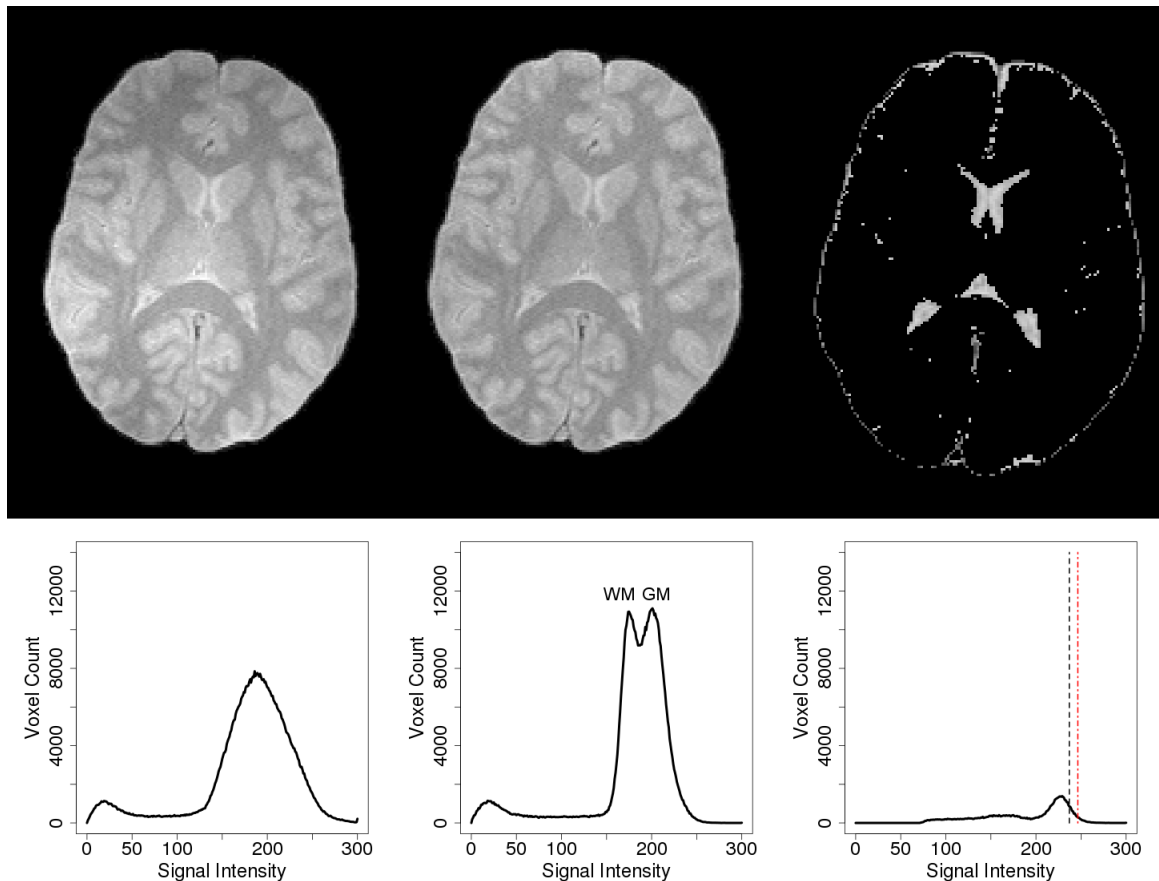
Figure 16a: Estimating the Macromolecular Fraction Using Proton Density Imaging.
The original proton density weighted image (left top) contains bias field inhomogeneities which limit its use as a parametric map. Estimation and removal of this bias field results in a much flatter image (middle top) in which anatomical features of gray matter (GM) and white matter (WM) are visible on the histogram. Voxels representing cerebrospinal fluid (CSF) are automatically identified (right top) and the intensity of the 90th percentile voxel within this class is recorded (dark dashed line) and a correction factor adjusting for saturation and T_2^* effects is applied to estimate an intensity value of pure CSF (red dashed line).

converted into an f_M map using the following equation:

$$f_M = 1 - f_W = 1 - \frac{S_{PD}}{S_{PD_{CSF}}}$$ (10)

Where $S_{PD\ CSF}$ represents the intensity of CSF voxels corrected for effects of

saturation and T_2^* decay; S_{PD} represents the intensity values of the PD image; f_W
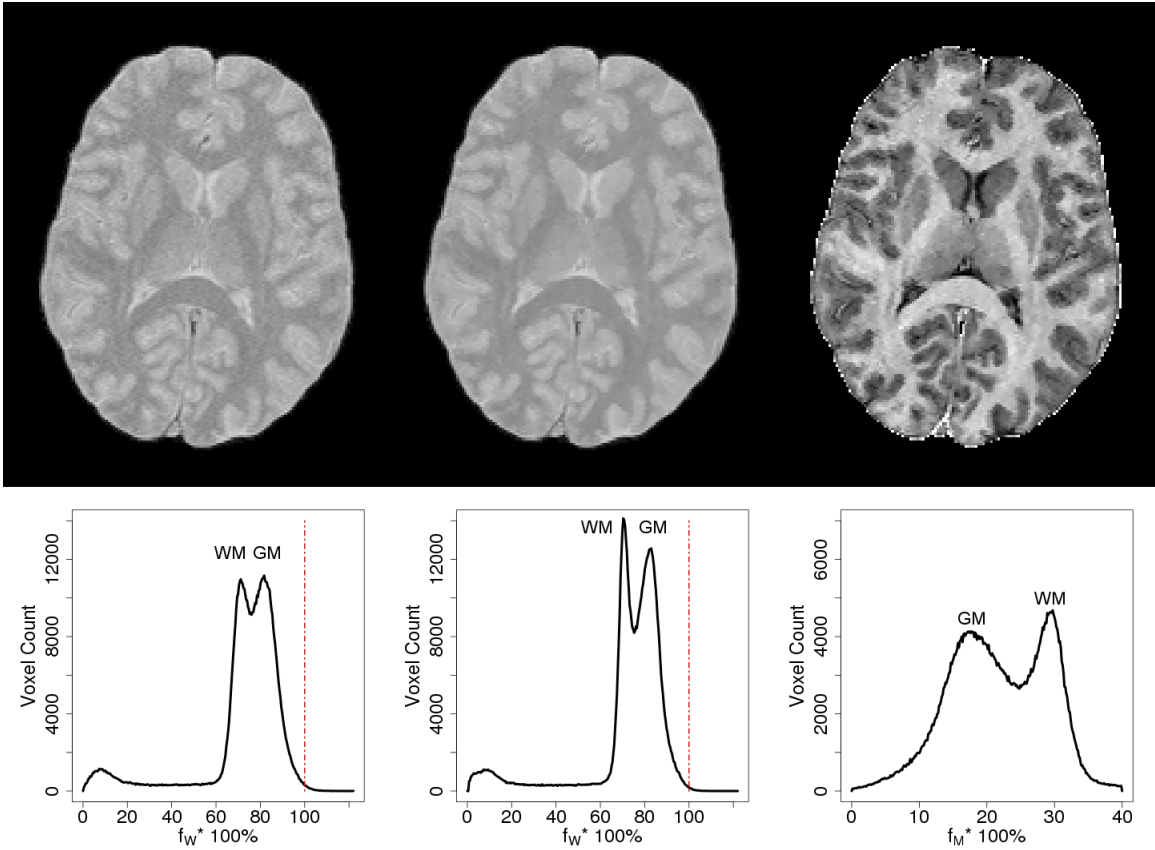
Figure 16b: Estimating the Macromolecular Fraction Using Proton Density Imaging.
The bias corrected image is scaled by setting the CSF intensity value to 100%, creating a water fraction (f_W* 100%) image (left top). This image is filtered with a nonlinear noise reduction algorithm to improve separation between tissue classes (i.e. gray matter (GM) and white matter (WM)) within edge defined boundaries (middle top). This final image is then converted into a map of fractional macromolecular (f_M * 100%) content (right top) using **equation 10**.

represents the fractional water content; and f_M represents the fractional macromolecular content. These steps are each illustrated in **Figures 16 a and b.**

Creating parametric maps of iron content

With reliable techniques to measure R_2 and f_M, it becomes possible to use the expanded relaxivity model for R_2 to calculate regional iron concentration. Values for the relaxivity constants r_{2fM} and r_{2Fe}, as well as the constant R_2^0 can be estimated by empirically modeling the measured R_2 values in several regions of interest (ROI) (caudate, putamen, pallidum, thalamus, white matter, gray matter) as a linear combination of the effects of both f_M, measured from the PD image; and iron concentration (Fe), estimated from postmortem literature values (Hallgren and Sourander, 1958).

$$R_2 = R_2^0 + r_{2f_M} f_M + r_{2Fe}[Fe] \qquad (11)$$

To do this, I used a mixed effect linear model with measured R_2 as the dependent variable; measured f_M values and estimated Fe concentrations (Hallgren and Sourander, 1958) as the independent fixed effects; R_2^0 as the intercept; and subject as the random effect in 20 healthy control subjects. This model yielded a fit that accounted for 91.5% of the variance in R_2 (adjusted R^2 =0.915, p < 0.0001) and resulted in the following beta estimates: $R_2^0 = 7.66$ s^{-1}; $r_{2fM} = 16.66$ s^{-1} f_M; and $r_{2Fe} = 0.2369$ s^{-1} mg Fe/100g^{-1}. With these estimates, the measured R_2 and f_M values can then be entered into a rearranged version of Equation 11 to solve for iron concentration, as shown in **Equation 12**.

$$[Fe] = \frac{\left[R_2 - \left(R_2^0 + r_{2M}\, f_M\right)\right]}{r_{2Fe}} \tag{12}$$

This formula can be applied to individual ROI measures to obtain regional iron estimates. This could also be applied at the voxelwise level using co-registered maps of R_2 and f_M with the same resolution, to create parametric maps of the distribution of estimated iron content as shown in **Figure 17**. Such maps would allow for voxelwise analysis of regional iron content, which could be used to investigate brain development and aging, as well as disease processes that are thought to alter brain iron handling.
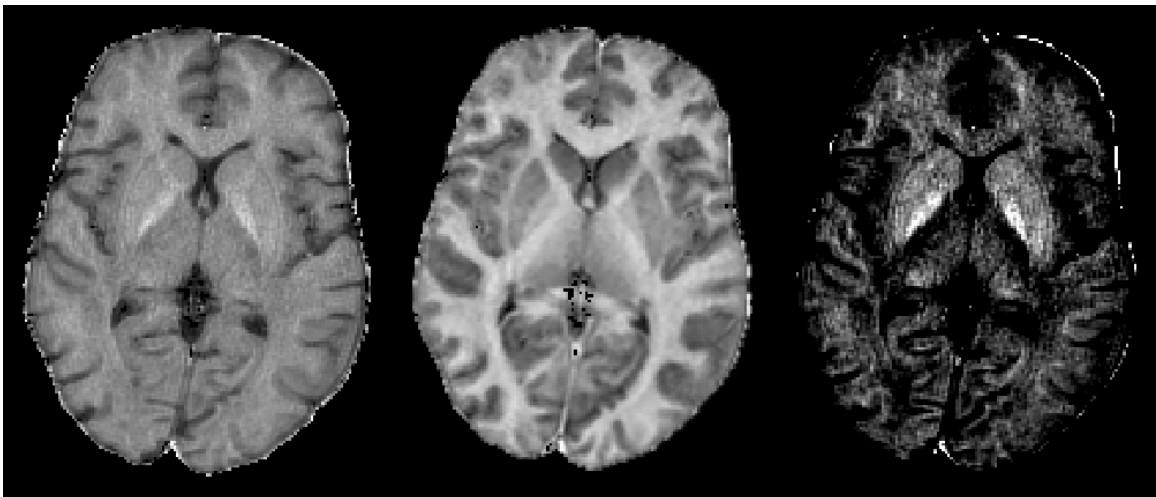
Figure 17: Creating parametric maps of iron content
Parametric map of iron content (right) created by applying a relaxivity model to the R_2 map (left) that incorporates the effects due to iron and macromolecular content (f_M)(middle) and then solving for iron at each voxel using equation 12. Grayscale values range from 0 to 25 s^{-1} for the R_2 map, 0 to 0.40 for the f_M map and 0 to 30mg Fe/100g tissue for the iron map.

Conclusions:

The analysis of MRI contrast mechanisms can be applied to investigate

and quantify many intrinsic properties of brain tissue including iron and tissue water content. While most MRI images reflect contributions from multiple factors, it is possible to isolate some of these effects and obtain relatively pure measurements of the relaxation rate constants and proton density. Since the transverse relaxation rate constant (R_2) is linearly proportional to tissue iron content, several researchers have used R_2 measurements to quantify iron content (Haacke et al., 2005; Dusek et al., 2013). However, R_2 is also affected by the fractional macromolecular content (f_M), making R_2 measurements alone a relatively nonspecific measure of iron content (Mitsumori et al., 2009). This fact is an especially important consideration when applying R_2 methods to investigate iron content in conditions that are associated with decreased f_M, including inflammation, edema, and tissue loss. In this chapter, I discuss methods to quantify and create maps of both R_2 and f_M. These methods utilize MRI sequences that are widely available and require minimal scan time (total scan time ~ 10-15 minutes), making them easy to incorporate into a clinical or experimental protocol. I also show how the information from these maps can be integrated using the expanded relaxivity model (Rooney et al., 2007; Mitsumori et al., 2009) to create parametric maps of the estimated brain iron content, which can be used for voxel-wise analysis of iron content. These methods can be applied to a variety of psychiatric and neurological disorders in which altered brain iron accumulation is believed to play a role.

MRI assessment of brain iron content in methamphetamine users

Introduction

Emerging evidence suggests that iron may play a role in MA toxicity both as biomarker of damage (Haacke et al., 2005; Melega et al., 2007; Dusek et al., 2013; Todd et al., 2013)and a potential source of toxicity (Yamamoto and Zhu, 1998; Park et al., 2006). Magnetic resonance imaging (MRI) provides noninvasive methods to investigate this possibility *in vivo* in human subjects. Iron is paramagnetic, and its presence shortens the transverse relaxation (T_2) time constant of nearby water protons causing decreased signal intensity on T_2 weighted images (Haacke et al., 2005; Dusek et al., 2013). Measuring this effect using quantitative MRI techniques can be used to assess the spatial distribution of iron. If MA increases brain iron accumulation to a similar extent as aging as has been reported in nonhuman primates (Melega et al., 2007), this effect would be readily detectable using quantitative T_2 MRI approaches. Increased iron levels measured with MRI have been shown to be associated with cognitive and motor impairment due to aging (Pujol et al., 1992; Cass et al., 2007; Sullivan et al., 2009), Alzheimer's disease (Ding et al., 2009), and Parkinson's disease (Atasoy et al., 2004) and have been implicated as a risk factor for developing neurodegenerative dementias (Gerlach et al., 1994; Bartzokis et al., 2007a). If present, increased iron levels in MA users may provide an MRI biomarker of MA toxicity that may reflect some of the changes to the DA system that contribute to

the psychiatric and cognitive symptoms associated with chronic MA exposure. In addition, the finding of increased brain iron would also impact the interpretation and planning of other MRI studies investigating the effects of MA, as increased iron content would affect the signal properties used in diffusion tensor imaging, functional MRI and structural imaging protocols (Berman et al., 2008; Sullivan et al., 2009; Pfefferbaum et al., 2010). This specific concern has been raised as a possible explanation for the inconsistencies and variability seen in studies investigating the structural abnormalities in MA users (Berman et al., 2008).

A preliminary retrospective study from our group found that former MA users have decreased T_2-weighted signal intensities in the striatum compared to aged-matched, healthy controls (Berlow et al., 2011). These preliminary results are consistent with other studies (Melega et al., 2007; Todd et al., 2013), which suggest that MA increases brain iron accumulation and support the hypothesis that brain iron content is increased in human MA users. However, while signal intensities on a T_2-weighted image are primarily determined by T_2, they can also reflect effects due to hardware and acquisition parameters. In addition, the transverse relaxation time constants (T_2 and T_2^*) reflect tissue composition effects from both the relative water content and tissue iron content ; and some studies have suggested that MA abuse is associated with alterations in water content within the striatum (Chang et al., 2005; Chang et al., 2007; Kiyatkin et al., 2007; Alicata et al., 2009; Kiyatkin and Sharma, 2009; Sharma and Kiyatkin, 2009). Therefore, a prospective study is necessary to replicate these preliminary

findings using MRI techniques that are more sensitive and quantitative for iron. The current study investigated regional brain iron content in healthy controls and subjects with a history of MA abuse using quantitative T_2 measurements combined with measurements of the relative tissue water content. It was predicted that subjects with a history of MA abuse would have increased brain iron concentrations in basal ganglia regions.

Methods:

Subjects

Imaging datasets were acquired from 27 abstinent MA users and 27 control subjects that participated in a study conducted at Oregon Health & Science University and the Portland VA hospital investigating the effects of MA on decision making, psychosis and criminal system involvement. MA subjects were recruited from treatment programs in Portland, OR and had been abstinent from all drugs for at least 2 weeks. Each subject completed a urine drug screen at the time of MRI examination. All MA subjects met DSM-IV (American Psychiatric Association (APA), 1994; Rooney et al., 2007; Mitsumori et al., 2009)criteria for MA dependence based on interview and chart review of available records. Extent of MA abuse was based on interview and corroborated, where available, by the medical records. Duration of MA use ranged from 2 years to 26 years with a median length of 8 years. Daily dosage estimates ranged from 0.4 g/day to 3.5 g/day, with a median daily dosage estimate of 1.25 g/day. Most of the subjects in

Table 1. Subject demographics

	MA dependent (n=27)	Controls (n=27)
Age (years)±SD	32.2±8.6	34.5±12.5
Age Range (years)	22-51	18-55
Sex (females/males)	8/19	10/17
Handedness (right/left)*	21/4	21/1
Education (years)±SD	12.2±1.6	14.0±1.2
Smokers	26	12

Table 1a. Demographics of subjects with complete TRSE images

	MA dependent (n=26)	Controls (n=25)
Age (years)±SD	32.3±8.8	34.7±12.9
Age Range (years)	22-51	18-55
Sex (females/males)	8/18	8/17
Handedness (right/left)*	21/4	21/1
Education (years)±SD	12.2±1.2	14.0±1.6
Smokers	25	12

Table 1b. Demographics of subjects with complete PD images

	MA dependent (n=20)	Controls (n=21)
Age (years)±SD	30.4±7.5	34.2±12.9
Age Range (years)	22-46	18-55
Sex (females/males)	5/15	8/13
Handedness (right/left)*	14/4	19/0
Education (years)±SD	12.3±1.1	14.3±1.5
Smokers	19	9

Table 1c. Demographics of subjects with complete R_2 images

	MA dependent (n=21)	Controls (n=20)
Age (years)±SD	31.4±8.6	34.6±13.1
Age Range (years)	22-51	18-55
Sex (females/males)	6/15	8/12
Handedness (right/left)*	15/4	18/0
Education (years)±SD	12.4±1.1	14.4±1.6
Smokers	20	9

*Handedness data was not available for 3 controls and 2 MA subjects
*Fe images were created from subjects with both complete R_2 and complete PD image sets

the MA group began using the drug by smoking or intranasal insufflation. About half of the subjects later administered the drug intravenously. Most were using daily or several times a day before going to treatment. The duration of abstinence from MA use ranged from 28 days to 444 days with a median length of 58 days. Control subjects were recruited from the general public or were non-drug using family members of an MA subject. Control subjects' drug use history was assessed by interview. Control subjects were excluded if they had ever met criteria for dependence on any substance except tobacco (subjects were considered smokers if they currently reported smoking). Subject demographic data are shown in Table 1. All participants provided informed consent (approved by the Portland VA Institutional Review Board) and were given a copy of the consent form.

Magnetic resonance imaging

All MRI data were acquired on a Siemens 3T TIM Trio at the Advance Imaging Research Center at Oregon Health & Science University. Acquisitions used in this study included a high-resolution, T_1-weighted, whole-brain 3D Magnetization Prepared Rapid Acquisition Gradient Echo (MPRAGE) sequence (field of view = 256 mm x 224 mm x 176 mm, matrix 256 x 224 x 176, TE=3.4ms, TI=1200ms, TR=2300ms, flip angle=12º), and a T_2-weighted, axial 2D, twice-refocused spin echo (TRSE), echo planar imaging sequences (field of view = 256mm x 256mm, matrix 128 x 128, 72 2mm thick slices, 2mm gap width, TR =

9400 ms, TE = 90ms). T_2-weighted TRSE images were originally collected to serve as baseline images in a diffusion tensor imaging series (i.e., b=0 acquisition). Subjects also received a 2D Turbo Spin Echo (TSE) sequences acquired with three different echoes (field of view = 192 mm x 256 mm, matrix 192x256, 65 2mm thick slices, TR 12 s, TEs = 24 ms, 73 ms and 97 ms) and a 3D Proton Density (PD) weighted, Fast Low Angle Shot (FLASH) sequence (field of view=192 mm x 256 mm x 192 mm, matrix 192 x 256 x 96, TR 50 ms, TE = 3.9 ms, flip angle=3 degrees). Many of the imaging series were not collected from all subjects and the number of subjects included in each analysis is detailed below. Demographics for each subject subset is detailed in Table 1. All images were converted to NIFTI format using dcmstack (dcmstack.readthedocs.org/en/v0.6.1/). One control subject was excluded from analysis due to motion artifacts. All image processing was carried out using tools from the Functional Magnetic Resonance Imaging of the Brain (FMRIB) Software Library (FSL)(Smith et al., 2004) and Statistical Parametric Mapping (SPM-8) (Ashburner and Friston, 2005).

T_2-weighted TRSE image processing and registration

T_2-weighted TRSE images were available for 51 subjects (26 MA and 25 Controls). Six T_2-weighted TRSE images from each subject were co-registered and averaged (Jenkinson et al., 2002). Voxels representing skull, skin and other nonbrain tissue were removed from the MPRAGE and the averaged TRSE

images using FSL's Brain Extraction Tool (BET)(Smith, 2002). The averaged T_2-weighted TRSE images were then registered to the anatomical MPRAGE images using a boundary-based registration approach that incorporated fieldmap-based distortion correction (Jenkinson and Smith, 2001; Jenkinson et al., 2002). The intensity values of the T_2-weighted TRSE images were log transformed to provide a linear inverse correlation with R_2 values (see below).

Quantitative mapping of R_2 and macromolecular content

Multi-echo T_2-weighted TSE images were collected from 41 subjects (21 MA, 20 Controls). The TSE images from different echo times were co-registered using linear transformation (Jenkinson and Smith, 2001; Jenkinson et al., 2002) and brain extracted using BET (Smith, 2002). T_2 maps and the corresponding R_2 (=$1/T_2$) maps were calculated by fitting the mono-exponential decay curve described in equation 1 at each voxel using nonlinear least squares (**Figure 14**).

$$S_{(x,y,z)}(TE) = S_{0(x,y,z)} e^{\left(\frac{-TE}{T_{2(x,y,z)}}\right)} \tag{13}$$

PD images were collected from 41 subjects (20 MA, 21 Controls). PD images were segmented and bias corrected using the Unified Segmentation approach implemented in SPM8's New Segment, which integrates registration to a standard space atlas, segmentation, and bias correction into a single model (Ashburner and Friston, 2005). The bias field full width half maximum (FWHM) cutoff was set to 30 mm. Bias corrected PD images were brain extracted using

BET (Smith, 2002; Greve and Fischl, 2009)and filtered with the nonlinear noise reduction algorithm SUSAN, which applies a Gaussian weighted median filter (sigma = 1 mm) within edge defined boundaries (Smith and Brady, 1997). The PD images were then scaled by setting the signal intensity of voxels representing cerebrospinal fluid to 100% to create maps of the fractional water content (f_W) and corresponding fractional macromolecular content (f_M) as shown in the following equation :

$$f_M = 1 - f_W = 1 - \frac{S_{PD}}{S_{PD_{CSF}}} \qquad (14)$$

Where $S_{PD\ CSF}$ represents the intensity of CSF voxels corrected for effects of saturation and T_2* decay[5]; S_{PD} represents the intensity values of the PD image; f_W represents the fractional water content; and f_M represents the fractional macromolecular content. This approach is illustrated in **Figures 16 a and b**. Calculated R_2 and f_M maps and segmented volumes were then registered to the MPRAGE images using rigid body transformations (Jenkinson and Smith, 2001; Jenkinson et al., 2002).

---

[5] While the signal intensities of the PD image are roughly proportional to the relative water content, saturation and T_2* decay will affect these values. The calculated combined effects of saturation and T_2* decay at 3T (TR = 50 ms, flip angle = 3 degrees, TE = 3.9 ms) reduce the signal to approximately 86.1% of M_0 in cerebrospinal fluid, 89.9% in gray matter and 89.7% in white matter. Applying a correction factor to the CSF results in intensity values that are more closely proportional to the proton density and relative water content.

Subcortical Region of Interest Identification

Bilateral, subcortical regions of interest (ROI) including caudate, putamen, and pallidum were identified on the MPRAGE images using FMRIB's Integrated Registration and Segmentation Tool (FIRST)(Patenaude et al., 2011). This program registers the brain to the Montreal Neurological Institute 152 subject (MNI152) standard space template and applies shape and intensity based models to segment subcortical brain structures (Gelman et al., 2001; Rooney et al., 2007; Patenaude et al., 2011). For two subjects without MPRAGE images (1 MA, 1 Control), FIRST was run using the f_M maps (Patenaude 2011d). These identified ROI's were applied to the registered T_2-weighted TRSE images, R_2 maps and f_M maps and to obtain regional values of log transformed T_2-weighted intensity, R_2 and f_M. Upper and lower thresholds were applied to these measurements to remove partial volume effects from cerebrospinal fluid. Additional summary images were created to allow for visual inspection of each step of the processing including brain extraction, registration and ROI placement. The reliability of this automated approach to assess regional measurements was assessed in separate dataset of 60 subjects (described in appendix 1 (Berlow et al., 2011)) who had two TRSE scanning sessions available. Using intraclass correlations (ICC(A,1)) with an absolute agreement criterion, the reliability of these measurements was found to be high (ICC(A,1) range: 0.96-0.98)(McGraw and Wong, 1996).

Creation of Parametric Maps of Iron Content

Parametric maps of brain iron content were calculated for the 40 subjects with both f_M and R_2 maps (20 MA, 20 Controls). R_2 was modeled as a linear combination of the relaxivity effects of f_M and iron (Fe) as follows:

$$\frac{1}{T_2}=R_2=R_2^0+r_{2f_M}f_M+r_{2Fe}[Fe] \tag{15}$$

where R_2^0 represents the region independent transverse relaxation rate constant; r_{2Fe} represents the transverse relaxivity due to ferritin iron concentration [Fe]; and $r_{if}M$ represents the relaxivity due to the macromolecular volume fraction, f_M *(Rooney et al., 2007)*(Mitsumori et al., 2009). The relaxivity values for the macromolecular fraction (r_{2M}) and iron content (r_{2Fe}) along with an estimate of R_2^0 were calculated by empirically modeling the measured R_2 values in several ROIs (caudate, putamen, pallidum, thalamus, white matter, gray matter) as a function of the combined effects of both f_M, measured from the PD image; and iron concentration (Fe), estimated from postmortem literature values (Hallgren and Sourander, 1958). Rearranging Equation 15 to solve for iron concentration, as shown in Equation 16, then allows for the calculation of iron content within ROIs and at the voxel level, creating parametric maps of the distribution of iron content as seen in **Figures 17 and 18**.

$$[Fe]=\frac{\left[R_2-\left(R_2^0+r_{2M}f_M\right)\right]}{r_{2Fe}} \tag{16}$$

72
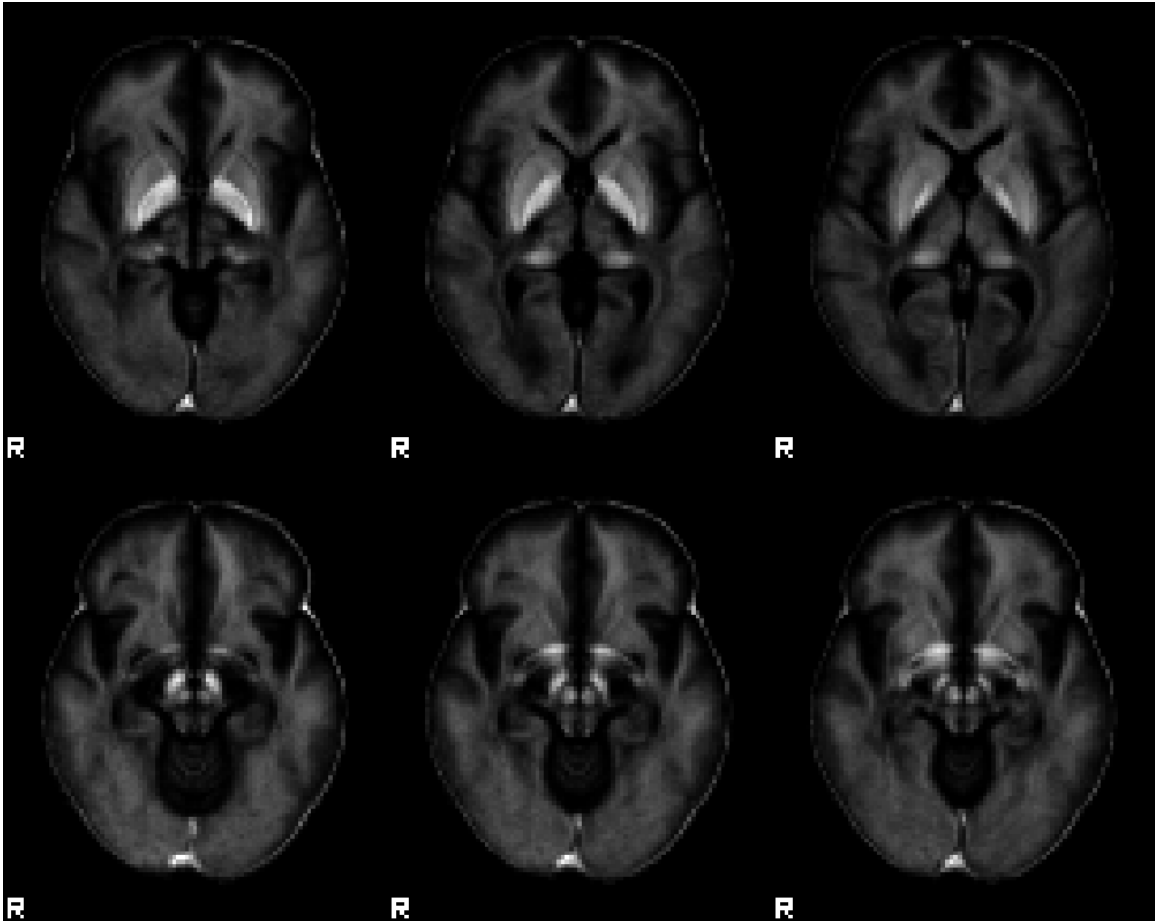
Figure 18: Averaged Fe map from 40 subjects
Averaged Fe map from 40 subjects, demonstrating areas of high iron content in basal ganglia and thalamic regions (top row) and in midbrain structures (bottom row). Grayscale values range from 0 to 25 mg Fe / 100 g tissue.

Nonlinear registration and voxel-wise analysis

MPRAGE images were nonlinearly registered to MNI152 space using FMRIB's Nonlinear Image Registration Tool (FNIRT) (Andersson et al., 2007a, b). The calculated warp fields were then applied to the log transformed T_2-weighted TRSE images using the previously acquired transformations as starting points. A study specific template of the TSE images was created by applying the warp

73

fields to the TSE base images and averaging these warped images to create a TSE template in MNI152 space. All TSE images were then nonlinearly registered to this template. The final calculated warp fields were then applied to the log transformed T_2-weighted TRSE images, f_M maps, R_2 maps and parametric iron maps using the previously acquired linear transformations as starting points.[6]

Statistical Analysis

Demographic data between groups was assessed using standard parametric and nonparametric analyses (T-tests, Wilcoxon rank sum (W), Fisher's exact test (FET) and chi-squared (X^2)).

Mixed effect linear models were constructed using MRI measurements and calculated values (R_2, f_M, log transformed T_2-weighted signal intensity, calculated iron content) as dependent variables, ROI (Caudate, Putamen, and Pallidum), Hemisphere (Left and Right), Group (MA and Controls), Sex and Age as independent variables and Subject as the random variable. The interaction of Age X Group was included to assess the effects of MA on the rate of age related increases in iron. An additional interaction term of Age X ROI was also included, as this interaction has previously been demonstrated (Pfefferbaum et al., 2009). Similarly, the inclusion of Hemisphere and Sex into the model was based on previous findings of the effects of Hemisphere and Sex on iron deposition, with left subcortical regions showing increased iron content compared to right regions

---

6. This two step procedure, involving both template creation and registration to the template, allowed for the inclusion of two subjects with R_2 and f_M maps that did not have MPRAGE images while using the same registration approach for all subjects.

(Xu et al., 2008) and men showing increased iron levels compared to women (Bartzokis et al., 2007b). Similar mixed linear models were also constructed for each ROI to examine effects in individual regions. The significant α level was set to p=0.05. All mixed effects models were fitted by restricted maximum likelihood (REML) as implemented in the Linear and Nonlinear Mixed Effects Models library in R (Pinheiro et al., 2009; R Development Core Team, 2010).

Voxel-wise linear regression models assessing age and group status were created using FSL's general linear model (Smith et al., 2004). Brain masks were created by thresholding the averaged 4d datasets to reduce effects of partial voluming (R_2 map threshold: 8 s-1; f_M map threshold: 0.10; Fe map threshold: 5 mg Fe/100g). Nonparametric permutation tests were performed to estimate the null distributions of these models using Randomise with 5,000 or 10,000 permutations (Nichols and Holmes, 2002). Resulting p values were adjusted using the cluster based thresholding method in Randomise to maintain a family-wise error (FWE) rate of 0.05 (t > 2.2). Resulting clusters were reported using the cluster and atlasquery functions in FSL (Smith et al., 2004). As an exploratory analysis, voxels within the substantia nigra were also inspected using the uncorrected t statistic maps to investigate potential group differences within this small brainstem region that may not have survived cluster based corrections for multiple comparisons.

Results:

The MA and control subjects did not differ by age (t(52)=0.80, p=0.43), sex ratio (X^2=0.08, p=0.77) or handedness (p=0.35, FET). The proportion of smokers in the MA group (26/27) was significantly larger than the proportion in the control group (12/27) (p<0.001, FET). Years of education attained was also significantly lower in the MA group (MA median 12 years vs. Control 14 years) (W=598, p<0.001).

Regional values from the f_M maps were in close agreement with previous studies as shown in **Table 2**. A linear mixed effect model using only estimates of iron concentration (Hallgren and Sourander, 1958; Nichols and Holmes, 2002; Smith et al., 2004)to explain R_2 values in multiple regions yielded a significant fit, explaining 75% of the variance in R_2 (Model 1 adjusted R^2=0.75, p<0.0001). Adding measured f_M values to this model (as shown in **Equation 15**) significantly improved this fit, accounting for 89% of the variance (Model 2 adjusted R^2=0.89, p<0.0001, ANOVA of Model 1 vs. Model 2 (F(1,237)=281.86, p<0.0001)); yielding the following estimated values: r_{2fM} = 16.0 s^{-1} f_M^{-1}; r_{2Fe} = 0.236 s^{-1} mg Fe/100g^{-1}; and R_2^0 = 7.85 s^{-1}. Fe measurements calculated from the resulting relaxivity model were very consistent with previous studies, especially for regions with high iron content, as shown in **Table 3**. Using similar linear models, a strong inverse correlation was found between the log of the T_2-weighted signal intensity measurements and measure R_2 values (R^2=0.86, p<0.0001)(**Figure 19**). The strength of this relationship was reduced when examining individual regions;

Table 2. Macromolecular fraction (f_M) measurements by brain region

	MRI Studies				Postmortem Studies			Average f_M values from previous studies	Current study f_M values ± sd
	Neeb 2008	Gelman 2001	Fatrousos 1999	Whittall 1997	Himwich 1955	Koch 1922	Randall 1938		
Gray Matter[a]	18.4[a]	13.8[a]	-	16.8	17.6	17.4	15.88[a]	16.80	16.75 ± 0.86
White Matter[b,c]	30.9[b]	-	31.3[b]	29.2	-	30.5[c]	29.36[b]	30.48	29.55 ± 0.09
Caudate	15.2	18.4	19.7	12.6	17.6	-	18.57	16.70	18.17 ± 0.84
Putamen[d]	16.8	21.2	22.9[d]	16.9	20.1	-	-	19.58	21.87 ± 0.65
Pallidum	-	26.7	-	-	-	-	-	26.70	27.91 ± 0.56
Thalamus	-	26.6	24.2	20.2	21.5	-	24.21	23.13	24.11 ± 0.57

a:prefrontal cortex
b:frontal white matter
c:corpus collosum
d: lentiform nucleus

Table 3. Calculated Iron measurements by brain region

	Iron Concentration (mg/100g wet weight)			Calculated Fe values from the current study[a]
	Langkammer et al. 2010	Hallgren and Sourander 1958[a]	Mitsumori, Wantanbe and Takaya 2009[a]	
Gray Matter	-	2.92 ± 0.41[b]	4.1 ± 1.2[b]	1.1 ± 1.3
White Matter	4.8 ± 1.4	4.24 ± 0.88[b]	4.0 ± 1.7[b]	3.3 ± 1.4
Caudate	9.2 ± 1.5	9.28 ± 2.14	8.8 ± 2.3	8.6 ± 1.6
Putamen	15.3 ± 2.9	13.32 ± 3.43	11.6 ± 2.4	12.6 ± 2.4
Pallidum	20.5 ± 3.2	21.30 ± 3.49	22.5 ± 4.6	19.1 ± 4.1
Thalamus	4.9 ± 1.1	4.76 ± 1.16	4.9 ± 2.0	6.2 ± 2.0

a: The iron measurements from the Hallgren & Sourander paper were used to estimate the relaxivity values for iron in the models used in the current study as well as the study by Mitsumori et al. 2009
b: Values for prefrontal gray matter and white matter

Table 4. Regional values for R_2, f_M, T_2-weighted signal intensity, and calculated iron content

	R_2 (s^{-1}) (mean±sd)	
	Control Subjects	Methamphetamine Users
n	20	21
Left Caudate	12.76±0.27	12.75±0.39
Right Caudate	12.86±0.34	12.79±0.38
Left Putamen	14.32±0.62	14.25±0.60
Right Putamen	14.43±0.56	14.27±0.52
Left Pallidum	16.69±1.14	16.77±1.02
Right Pallidum	16.92±0.98	16.94±0.79
Left Thalamus	13.12±0.29	13.01±0.56
Right Thalamus	13.29±0.36	13.23±0.57

	f_M * 100% (mean±sd)	
	Control Subjects	Methamphetamine Users
n	21	20
Left Caudate	18.27±0.83	18.11±0.66
Right Caudate	18.26±0.80	18.05±1.46
Left Putamen	21.95±0.66	21.91±0.72
Right Putamen	21.92±0.76	21.69±0.68
Left Pallidum	27.70±0.77	27.84±0.59
Right Pallidum	27.99±0.78	28.11±0.42
Left Thalamus	24.66±0.45	23.85±0.52
Right Thalamus	24.20±0.44	23.71±0.67

	log(T_2-weighted Signal Intensity) (mean±sd)	
	Control Subjects	Methamphetamine Users
n	25	26
Left Caudate	5.85±0.124	5.84±0.086
Right Caudate	5.81±0.097	5.81±0.076
Left Putamen	5.77±0.169	5.79±0.098
Right Putamen	5.58±0.129	5.57±0.106
Left Pallidum	5.27±0.224	5.24±0.130
Right Pallidum	5.20±0.172	5.19±0.128
Left Thalamus	5.66±0.105	5.67±0.100
Right Thalamus	5.60±0.101	5.62±0.084

	Calculated Fe content (mg/100g wet tissue) (mean±sd)	
	Control Subjects	Methamphetamine Users
n	20	20
Left Caudate	8.41±1.17	8.42±1.82
Right Caudate	8.85±1.60	8.61±2.05
Left Putamen	12.54±2.51	12.23±2.58
Right Putamen	13.03±2.31	12.48±2.24
Left Pallidum	18.68±4.71	18.92±4.44
Right Pallidum	19.46±4.20	19.42±3.51
Left Thalamus	5.60±1.33	5.78±2.57
Right Thalamus	6.66±1.52	6.78±2.61

however, even in individual ROIs, the correlations remained highly significant (Caudate: R^2=0.19, p=0.0031; Putamen: R^2=0.38, p<0.0001; and Pallidum: R^2=0.53, p<0.0001).

Summary data of regional R_2, f_M, T_2-weighted signal intensity and calculated iron content (Fe) measures are shown for each group in **Table 4**. For each of these measures, the Methamphetamine group had very similar values to
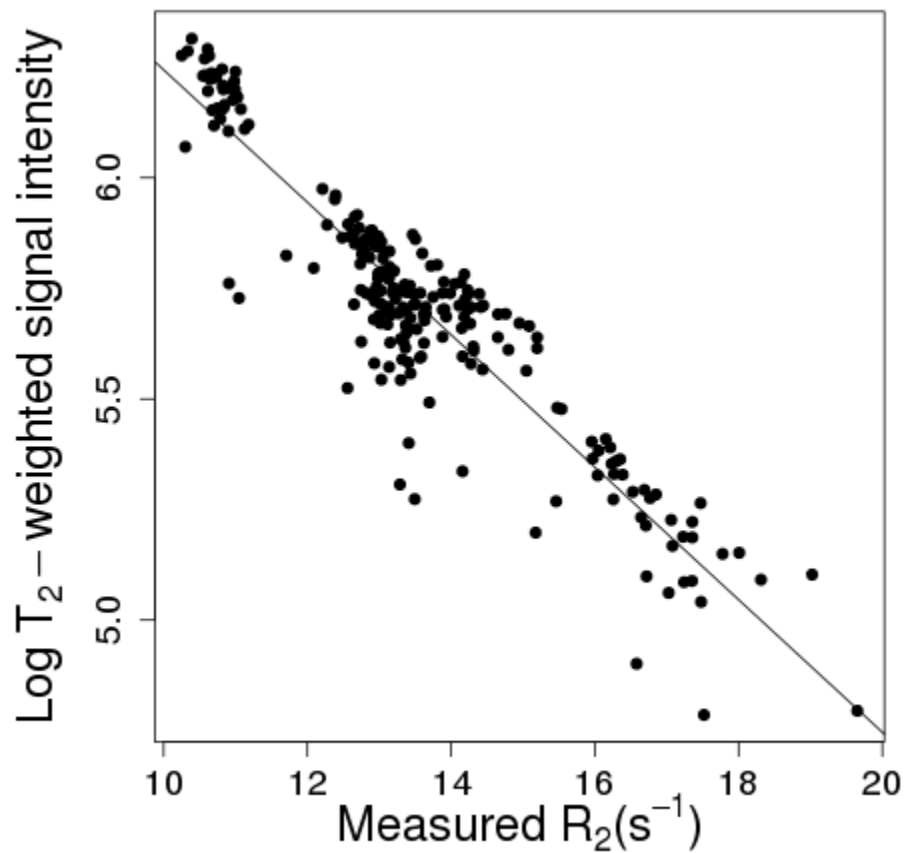
Figure 19: Correlation of the measured R_2 values and the log of the T_2-weighted signal intensity measurements across multiple regions of the brain (R^2=0.86, p<0.0001)

Table 5. Mixed effect models assessing regional differences in R_2, f_M, T_2 signal intensity and calculated Fe.

R_2				
	numDF	denDF	F-value	p-value
(Intercept)	1	198	1033.2279	<.0001
Gender	1	36	2.0589	0.16
Side	1	198	3.8127	0.0523
Age	1	36	1.9169	0.1747
Region	2	198	142.5786	<.0001
Group	1	36	0.2865	0.5957
Age:Region	2	198	2.9155	0.0565
Region:Group	2	198	0.5017	0.6063
Age:Group	1	36	0.2643	0.6103

f_M				
	numDF	denDF	F-value	p-value
(Intercept)	1	198	1999.2427	<.0001
Gender	1	36	3.0297	0.0903
Side	1	198	0.2922	0.5894
Age	1	36	3.4703	0.0707
Region	2	198	490.2394	<.0001
Group	1	36	4.0629	0.0513
Age:Region	2	198	4.3429	0.0143
Region:Group	2	198	0.7875	0.4564
Age:Group	1	36	4.1805	0.0483

T_2				
	numDF	denDF	F-value	p-value
(Intercept)	1	248	7077.408	<.0001
Gender	1	46	1.257	0.2681
Side	1	248	124.482	<.0001
Age	1	46	8.595	0.0052
Region	2	248	118.166	<.0001
Group	1	46	1.822	0.1837
Age:Region	2	248	1.311	0.2715
Region:Group	2	248	0.65	0.5227
Age:Group	1	46	1.558	0.2183

Calculated Fe				
	numDF	denDF	F-value	p-value
(Intercept)	1	193	18.79517	<.0001
Gender	1	35	1.23753	0.2735
Side	1	193	3.68449	0.0564
Age	1	35	0.79833	0.3777
Region	2	193	47.71733	<.0001
Group	1	35	0.34086	0.5631
Age:Region	2	193	3.3039	0.0388
Region:Group	2	193	0.24601	0.7822
Age:Group	1	35	0.30181	0.5862

numDF=numerator degrees of freedom
denDF=denominator degrees of freedom

the Control group in every region analyzed. The results of the planned comparisons are detailed below.

Region of Interest Analysis

Mixed effect linear models assessing the effect of Region (Caudate, Putamen, and Pallidum), Group (MA and Control), Sex, Hemisphere and Age yielded significant overall fits for all dependent variables (T_2-weighted signal intensity, R_2, f_M and calculated iron content (Fe)); with all models accounting for greater than 95% of the variance. The details of these models are presented in **Table 5**. As expected, the main effects of Region and the interactions of Region X Age were significant for most of these models, (the interaction of Region X Age was not detected in the T_2-weighted signal intensity model, however, this model did detect large main effects for both Region and Age). Main effects of Hemisphere reached trend levels of significance for the R_2 model and Fe model and were highly significant in the T_2-weighted signal intensity model. There were no significant main effects of Sex detected. There were no main effects of Group or interactions of Group X Region detected. The f_M model yielded a significant Group X Age interaction ($F(1,36)=4.18$, $p=0.048$).

In order to assess these measures at the regional level, additional mixed effects models were constructed testing the effects of Group (MA and Control), Age and Hemisphere at each ROI, using subject as the random variable. Based on the larger models, the interaction term for Group * Age was also included in

81

the f_M models.

In the R_2 models, significant age effects were seen in the Caudate ($F(1,38)=2.35$, $p=0.0243$) and Putamen ($F(1,38)=11.53$, $p=0.0016$), with increasing age associated with increasing R_2. There was also a significant main effect of hemisphere on R_2 values in the Pallidum ($F(1,38)=10.62$, $p=0.0023$) with greater R_2 values seen in the right hemisphere. No Group differences in R_2 values were seen for any of these regions.

The f_M models also detected a significant age effect in the Putamen ($F(1,37)=5.62$, $p=0.023$) and a significant effect of side in the Pallidum ($F(1,40)=10.20$, $p=0.0027$), with increasing age associated with increasing f_M and the right Pallidum associated with increased f_M. No Group differences or Group X Age interactions were detected in the f_M models for any of the regions.

Models assessing the log of T_2-weighted signal intensity measurements detected significant Side and Age effects for all three regions; with increasing Age associated with decreasing T_2-weighted signal intensity in the Caudate ($F(1,48)=15.37$, $p=0.0003$), Putamen ($F(1,48)=17.93$, $p=0.0001$) and Pallidum ($F(1,48)=7.02$, $p=0.011$); and lower intensity values in the right hemisphere for the Caudate ($F(1,50)=17.59$, $p=0.0001$), Putamen ($F(1,50)=253.02$, $p<0.0001$) and Pallidum ($F(1,50)=15.81$, $p=0.0002$). No Group differences in T_2-weighted signal intensity were detected for any region.

Similar main effects of Age and Hemisphere were seen in the models assessing calculated iron content. Increased iron content estimates were seen
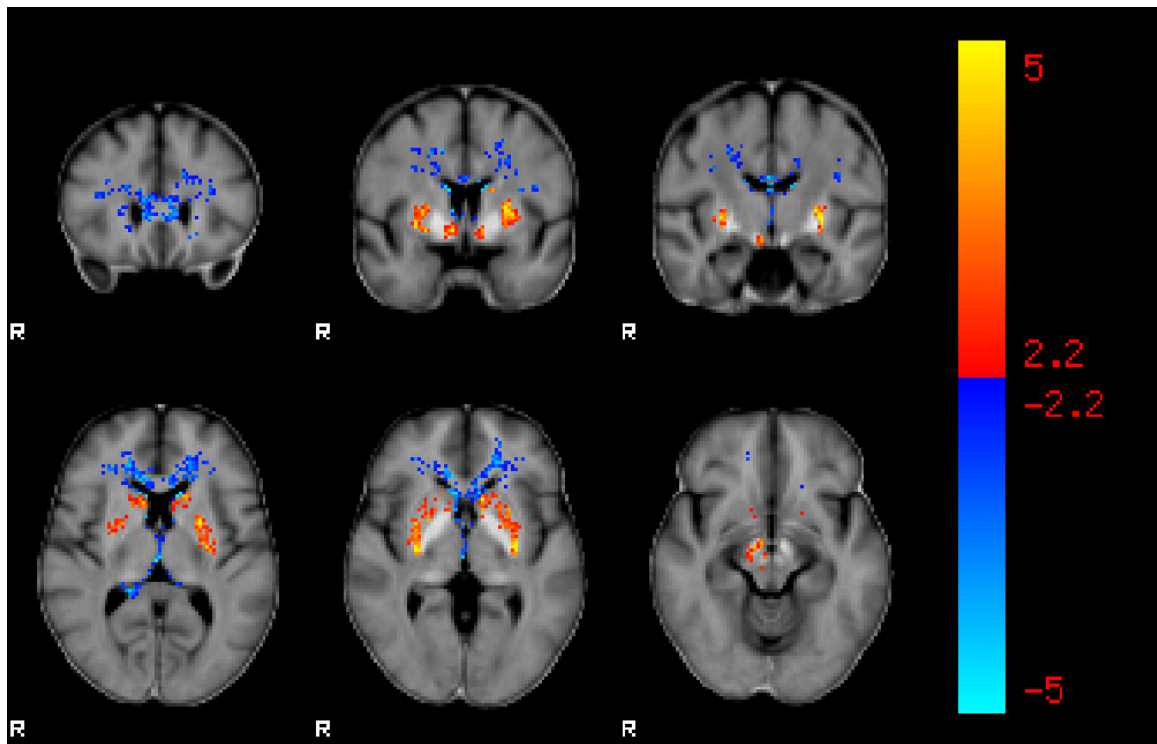
Figure 20: Age associated changes in R_2.
Age was associated with increased R_2 (t values shown in red-yellow) in the caudate, putamen and substantia nigra and decreased R_2 (t values in blue-lightblue) in the frontal white matter. Statistical results are displayed on the average R_2 map in MNI152 space.

on the right side in the Caudate $(F_{(1,39)}=4.21, p=0.047)$, Putamen $(F_{(1,39)}=4.92, p=0.033)$ and Pallidum $(F_{(1,39)}=6.41, p=0.016)$. Increasing iron content estimates were also associated with increasing Age in the Putamen $(F_{(1,37)}=7.68, p=0.0087)$. No significant differences in calculated iron content were seen between the MA group and Control subjects.

Voxelwise Analysis

The voxelwise analysis of the R_2 maps confirmed many of the findings from the ROI analysis as shown in **Figure 20**. Significant positive correlations of
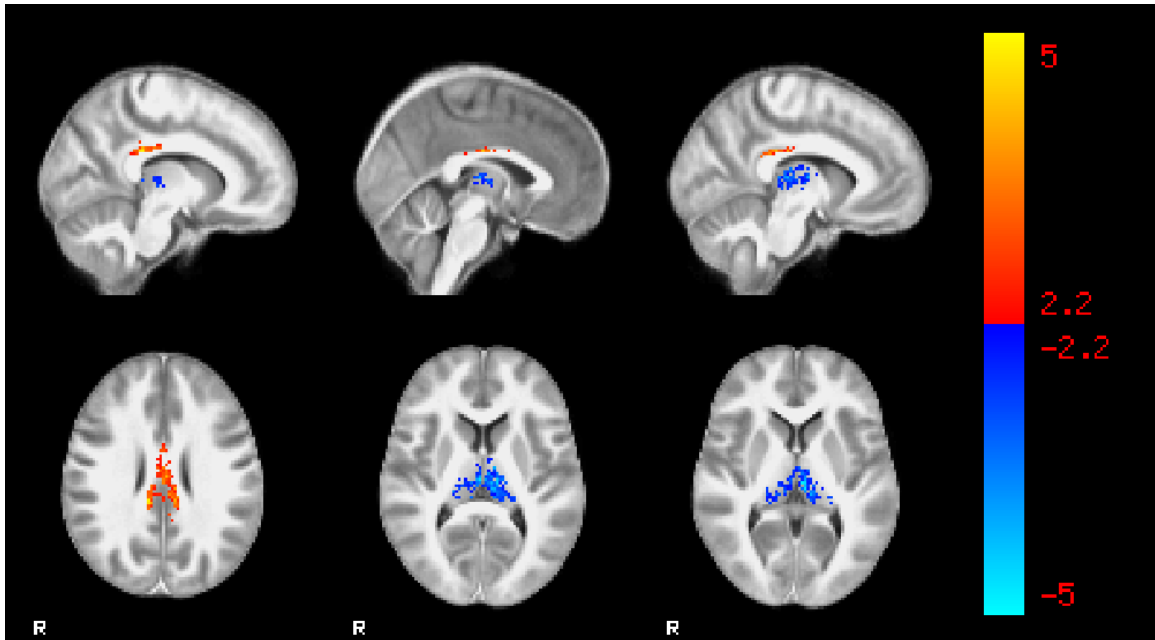
Figure 21: Group differences in fractional macromolecular (f_M) content.
Subjects in the MA group had higher f_M (t values shown in red-yellow) along the superior body of the corpus callosum and extending to superior portions of the splenium and posterior portions of the cingulum. The MA group had lower f_M values (blue-lightblue) in a cluster that included large portions of the left and right thalamus. Statistical results are displayed on the average f_M map in MNI152 space.

age and R_2 were seen bilaterally in the caudate and putamen and extending inferiorly to the right substantia nigra and red nucleus, consistent with age-associated iron accumulation in these regions. Additionally, increasing age was associated with decreased R_2 within several white matter tracts, including
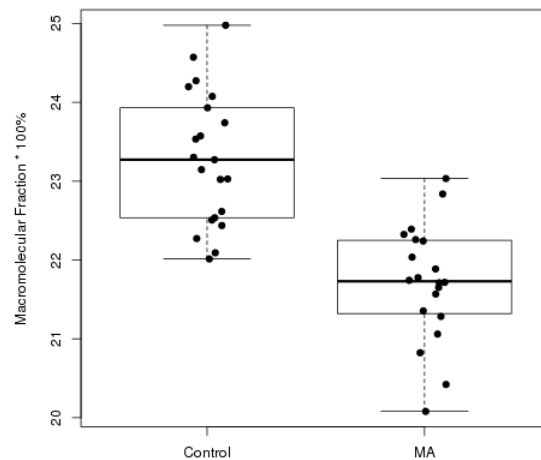
Figure 22: Average f_M values from the thalamus cluster identified in the voxelwise analysis of f_M maps.

the genu and body of the corpus callosum; bilateral aspects of the anterior and superior corona radiata; and bilateral portions of the superior longitudinal fasciculus. No group differences in R_2 were found.

Analysis of the f_M maps also confirmed the findings from the ROI analysis and identified two additional regions with group differences. The MA group had higher f_M values in a white matter region that included the superior body of the corpus callosum and extended to superior portions of the splenium and posterior portions of the cingulum. The MA group had lower f_M values in a cluster that
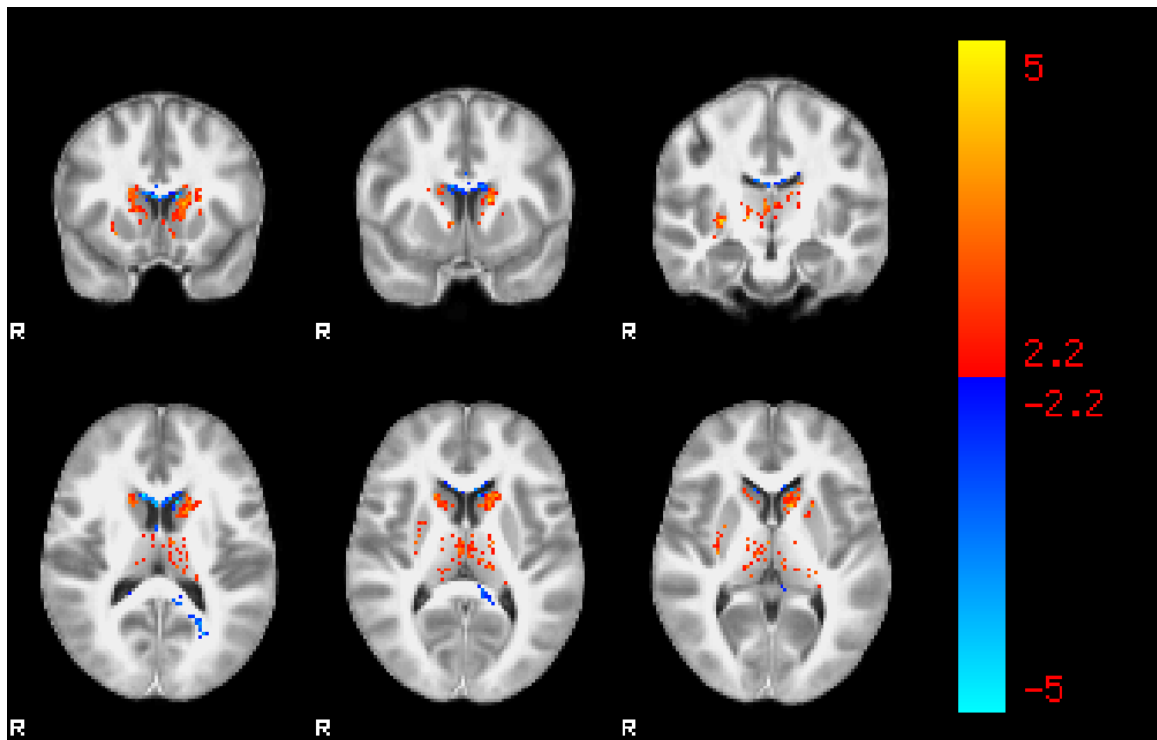
Figure 23: Age associated changes in fractional macromolecular (f_M) content.
Age was associated with increased f_M (t values shown in red-yellow) in the caudate, putamen and thalamus and decreased f_M (blue-lightblue) at the inferior border of the corpus callosum and extending to the splenium and left posterior white matter. Statistical results are displayed on the average f_M map in MNI152 space.
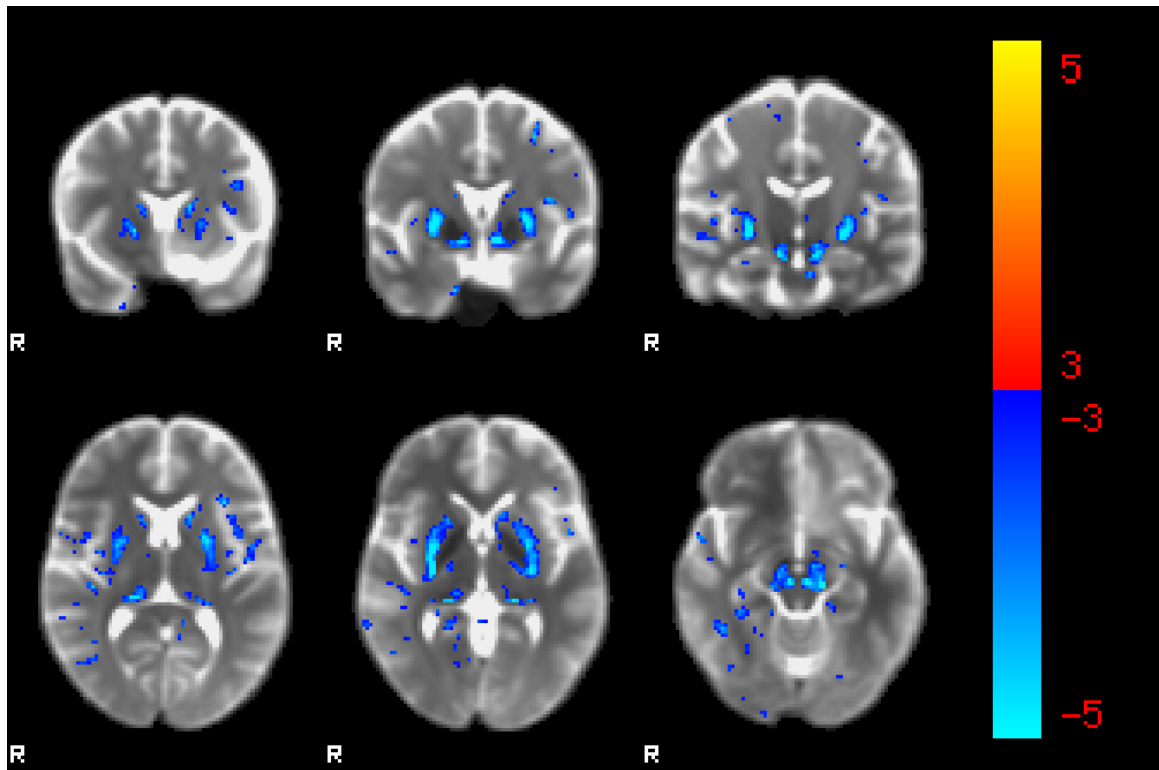
Figure 24: Age associated changes in the log of T$_2$-weighted signal intensity values.
Age was associated with decreased T$_2$ weighted signal intensity values (t values shown in blue-lightblue) in the caudate, putamen, pulvinar nucleus of the thalamus, substantia nigra, red nucleus and cortical gray matter regions. Statistical results are displayed on the average TRSE T$_2$-weighted image in MNI152 space.

included large portions of the left and right thalamus (**Figures 21 and 22**).

Increasing age was associated with increasing f$_M$ values bilaterally in the caudate, putamen and thalamus and decreasing f$_M$ values along the inferior border of the body of the corpus callosum (**Figure 23**).

The voxelwise analysis of the log T$_2$-weighted signal intensity images did not detect any group differences. There was a large region identified that was negatively correlated with increasing age that included bilateral basal ganglia
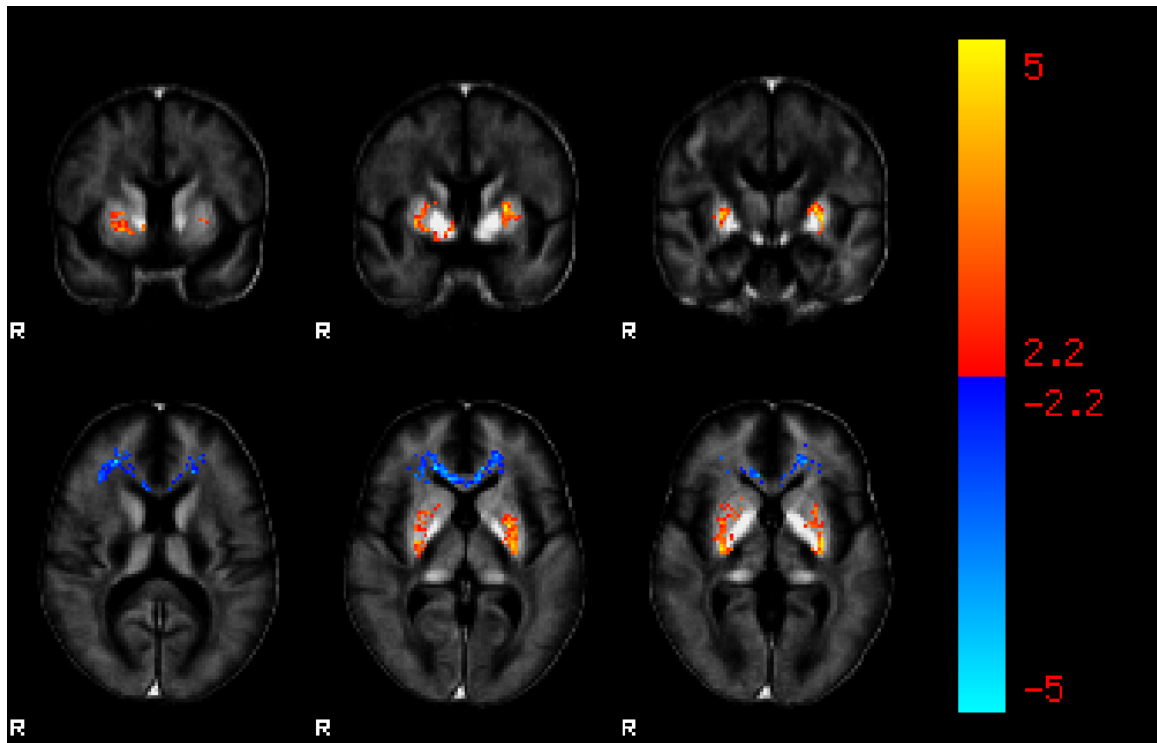
Figure 25: Age associated changes in calculated iron content.
Age was associated with increased iron content (t statistics shown in red-yellow) in the caudate, putamen and ventral striatum and decreased iron content (t statistics in blue-lightblue) in the frontal white matter. Statistical results are displayed on the average Fe map in MNI152 space.

regions including the caudate, putamen and substantia nigra, the pulvinar nucleus of the thalamus, and extended to surrounding cortical areas in the temporal and parietal lobes as shown in **Figure 24**.

The calculated iron content maps also showed no group differences. As in the previous models, significant age effects were seen primarily in left and right putamen with increasing age associated with increasing calculated iron content as shown in **Figure 25.** Additionally, increasing age was associated with decreased iron content in the frontal white matter, including the genu of the

corpus callosum and extending to the left and right anterior corona radiata.

As shown in **Figure 26**, additional inspection of the uncorrected t statistic maps from both the R_2 and iron map voxelwise analyses within the substantia
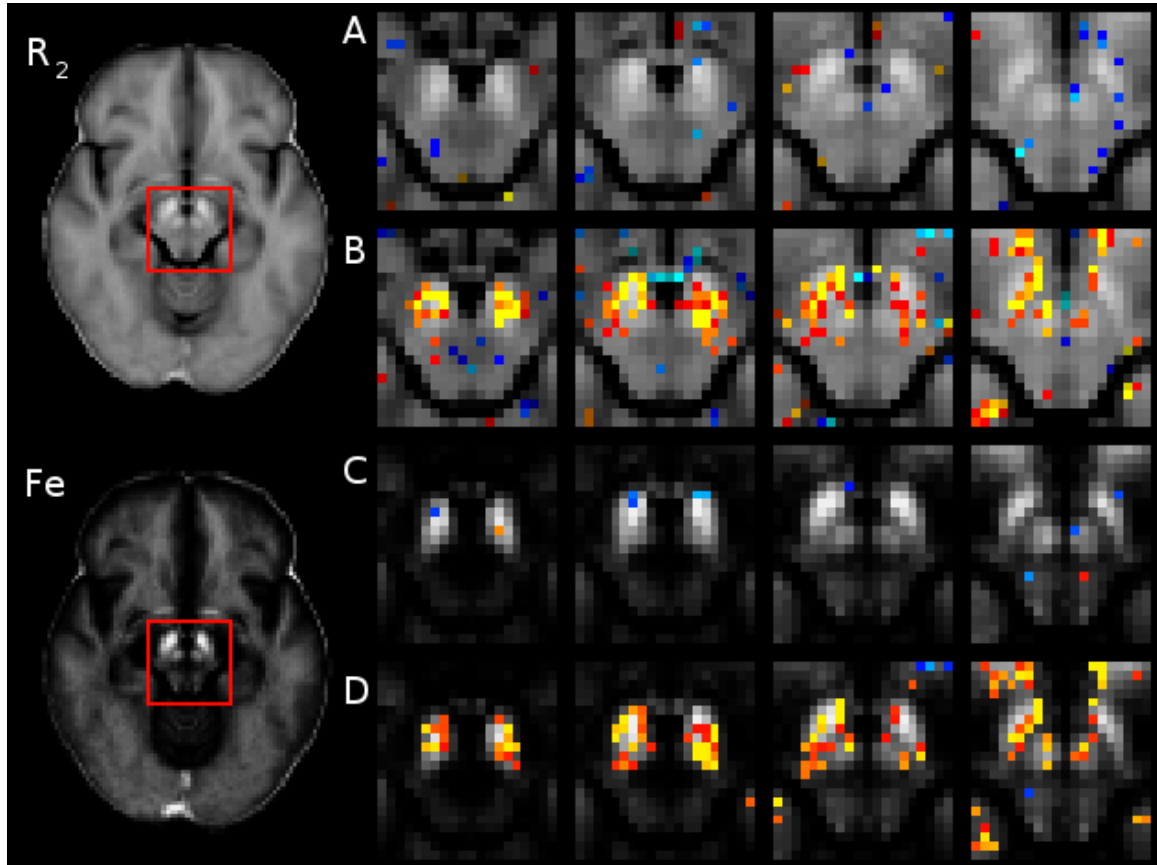
Figure 26: Exploratory analyses of group differences in R_2 and Fe within the substantia nigra (SN).
Row A shows four contiguous slices of the uncorrected t statistic map (t > 2.0) for group differences in R_2 within the SN with red-yellow voxels showing areas of increased R_2 in the MA group and blue-lightblue voxels showing areas of increased R_2 in the controls. No consistent patterns of group differences are evident. In contrast, Row B demonstrates a clear bilateral pattern of increasing R_2 with increasing age in the SN (red-yellow). Similarly, Row C displays group differences in calculated Fe within the same axial slices through the SN and again, no consistent patterns are seen that would suggest group differences in Fe, however, clear patterns of increasing Fe with increasing age are seen in Row D.

nigra revealed no consistent trends or patterns for an effect of group within the substantia nigra. In contrast, similar inspection of the substantia nigra for effects of age yielded similar but more inclusive regions of increased R_2 and increased Fe in the substantia nigra associated with increasing age as was found with the whole brain voxelwise analysis of R_2 described above.

Discussion

This study utilized multiple *in vivo* MRI measures to investigate regional brain iron content in human subjects with a history of MA abuse. Quantitative relaxometry measures that are specific for iron were unable to detect any differences in regional iron content in former MA users when compared to aged-matched healthy control subjects. These results are in contrast to our preliminary retrospective study that used T_2-weighted signal intensity measurements as a surrogate for T_2 and R_2 (Berlow et al., 2011)(appendix 1). Using a similar T_2-weighted signal intensity approach with consistent acquisition parameters and improved registration and distortion correction techniques (Greve and Fischl, 2009), the current study was unable to replicate these initial findings. Strong inverse linear correlations were found between the log of the T_2-weighted signal intensity measurement and the measured R_2 when assessing a broad range of tissue types, however, these correlations fell when assessing individual regions, explaining only 19% of the variance in the caudate and 38% of the variance in the putamen. These results highlight that T_2-weighted signal intensity is not a

quantitative measurement of T_2; and some of the variability in T_2-weighted signal intensity measurements is due to factors other than T_2, such as coil loading and subsequent RF calibration. In contrast, measuring T_2-weighted signal intensities at multiple echo times provides a method to precisely characterize the T_2 decay while correcting for many of these subject specific differences that affect single echo intensity values. Furthermore, while ferritin iron has a strong effect on T_2 and R_2, other changes in tissue composition will also affect these values. The current study demonstrated that the fractional macromolecular content also contributes to the measured R_2. Applying a relaxivity model which incorporates terms for the effects of both iron content and macromolecular content on R_2 (equations 3 and 4), thus provides a more specific measure of iron content than only measuring R_2 (Rooney et al., 2007; Mitsumori et al., 2009). This model allows for the detection of changes in R_2 due to ferritin iron even in the presence of excess tissue water that would decrease f_M and reduce measured R_2. Using these more specific and quantitative techniques for assessing brain iron content, the current study was unable to detect any significant differences between former MA users and age-matched healthy controls.

The failure to detect significant group differences in brain iron content between MA users and controls using null hypothesis testing does not provide evidence that the two groups are the same; however, equivalence testing can provide support that the two groups do not differ by a specified amount (ε). The two one-sided test (TOST) provides a method to demonstrate that it is unlikely

Table 6. Equivalence testing for R_2, f_M, and calculated iron content

	R_2 (s^{-1}) (mean±sd)					TOST
	Controls	MA Users		Mean	90% Confidence	p
n	20	21	ε	difference	Interval	equivalence
Left Caudate	12.76±0.27	12.75±0.39	0.5	0.008	-0.16 to 0.18	<0.00010
Right Caudate	12.86±0.34	12.79±0.38	0.5	0.067	-0.12 to 0.25	0.00019
Left Putamen	14.32±0.62	14.25±0.60	0.75	0.19	-0.25 to 0.39	0.00049
Right Putamen	14.43±0.56	14.27±0.52	0.75	0.16	-0.37 to 0.50	0.00067
Left Pallidum	16.69±1.14	16.77±1.02	1.1	-0.08	-0.65 to 0.48	0.0022
Right Pallidum	16.92±0.98	16.94±0.79	1.1	-0.028	-0.50 to 0.44	0.00024
Left Thalamus	13.12±0.29	13.01±0.56	0.35	0.10	-0.13 to 0.34	0.041
Right Thalamus	13.29±0.36	13.23±0.57	0.35	0.15	-0.19 to 0.31	0.028

	f_M * 100% (mean±sd)					TOST
	Controls	MA Users		Mean	90% Confidence	p
n	21	20	ε	difference	Interval	equivalence
Left Caudate	18.27±0.83	18.11±0.66	0.50%	0.16	-0.23 to 0.56	0.078
Right Caudate	18.26±0.80	18.05±1.46	0.50%	0.20	-0.42 to 0.84	0.22
Left Putamen	21.95±0.66	21.91±0.72	0.50%	0.031	-0.36 to 0.40	0.019
Right Putamen	21.92±0.76	21.69±0.68	0.50%	0.23	-0.15 to 0.61	0.11
Left Pallidum	27.70±0.77	27.84±0.59	0.50%	-0.14	-0.50 to 0.22	0.049
Right Pallidum	27.99±0.78	28.11±0.42	0.50%	-0.12	-0.45 to 0.21	0.029
Left Thalamus	24.66±0.45	23.85±0.52	0.50%	0.81	0.55 to 1.06	0.98
Right Thalamus	24.20±0.44	23.71±0.67	0.50%	0.49	0.18 to 0.79	0.47

	Calculated Fe content (mg/100g wet tissue) (mean±sd)					TOST
	Controls	MA Users		Mean	90% Confidence	p
n	20	20	ε	difference	Interval	equivalence
Left Caudate	8.41±1.17	8.42±1.82	2.1	-0.012	-0.83 to 0.81	<0.00010
Right Caudate	8.85±1.60	8.61±2.05	2.1	0.24	-0.74 to 1.22	0.0014
Left Putamen	12.54±2.51	12.23±2.58	3.1	0.31	-1.04 to 1.67	0.00068
Right Putamen	13.03±2.31	12.48±2.24	3.1	0.54	-0.67 to 1.75	0.00051
Left Pallidum	18.68±4.71	18.92±4.44	4.6	-0.24	-2.68 to 2.20	0.0023
Right Pallidum	19.46±4.20	19.42±3.51	4.6	0.045	-2.02 to 2.11	0.00033
Left Thalamus	5.60±1.33	5.78±2.57	1.4	-0.18	-1.27 to 0.92	0.034
Right Thalamus	6.66±1.52	6.78±2.61	1.4	-0.12	-1.26 to 1.03	0.033

that the difference between groups exceeds a certain range within which it could be considered equivalent (Schuirmann, 1987; Hoenig and Heisey, 2001). This is similar to traditional null hypothesis testing except that now, H_0 assumes that a specified difference (ε) exists and this hypothesis is rejected if the 90% confidence interval of the difference is less than the specified amount, corresponding to $1 - 2\alpha$ (Schuirmann, 1987; Hoenig and Heisey, 2001). In the study by Melega et al. (2007) they found a 2.5 fold increase in iron staining in both the globus pallidus and a 3 fold increase of ferritin immunoreactivity in the substantia nigra of monkeys that received two doses of MA (each 2 mg/kg).[7] If one assumes that MA causes a similar but attenuated effect in human users resulting in a 25% increase in brain iron content, this would be equivalent or less than the expected age-associated increase from 20 years old to 40 years old in the three basal ganglia regions used in the current study (Hallgren and Sourander, 1958). Using these assumptions for the change in brain iron content along with the estimated relaxivity values for ferritin iron (r_{2Fe}=0.2358 s^{-1} mg Fe/100 g^{-1}), TOST tests were conducted for both R_2 measurements and calculated iron content for every region. As shown in **Table 6**, the confidence intervals for group differences in R_2 and calculated iron all include zero and do not exceed ε; suggesting rejection of the difference hypotheses and adoption of the equivalence hypotheses, which state that human MA users do not have increased brain iron accumulation in these regions.

---

7. For comparison, the median dose taken by the MA group in the current study was 15.8 mg/kg/day for several years (median 8 years, mean 10 years).

This conclusion is in stark contrast to the nonhuman primate study conducted by Melega et al. (2007) in which two doses of MA (2 mg/kg) were shown to increase ferritin immunoreactivity and iron levels within the pallidum and substantia nigra of young vervet monkeys (5-9 years) to levels seen in aged monkeys (19-22 years). The discrepancy could be due to interspecies differences in iron accumulation within the pallidum, differences in the relative age ranges of the two studies as well as differences in the exposure pattern to MA and other substances. In humans, iron accumulation in the pallidum occurs rapidly in the first two decades and then plateaus with little to no increase (Hallgren and Sourander, 1958; Pujol et al., 1992; Pfefferbaum et al., 2009). This pattern is very consistent with the findings of the current study in which age effects were not often seen within the pallidum. However, this pattern is different in nonhuman primates. In rhesus and Japanese macaques, iron levels in the pallidum continue to rise even into late age and greatly exceed iron levels seen in humans (Hardy et al., 2005; Berlow et al., 2012a)[appendix 2]. In addition, the animals in the nonhuman primate study were relatively younger than the subjects in the current study. Using the approximation that one vervet year equals roughly three human years (adapted from comparisons of human aging with rhesus macaques (Zhang et al., 2000; Hardy et al., 2005; Cass et al., 2007)), this suggests that the monkeys were comparable in age to a human cohort aged 15 to 27, somewhat younger than the current cohort, aged 18-55. It is possible that MA accelerates normal age associated iron accumulation only in earlier phases of rapid iron

accumulation, and such an effect may only be observable in very young MA users.

Finally, differences in the exposure pattern to MA and other substances, especially tobacco and nicotine, may attenuate and alter the expression of increased iron accumulation in human MA users (Caligiuri and Buitenhuys, 2005). It is likely that many of the MA users in this study initially began with small doses and gradually escalated to higher doses, developing tolerance to some of the neurotoxic effects (Kramer et al., 1967; Cho and Melega, 2002; Segal et al., 2003). Escalating dosing models have consistently been shown to result in reduced measures of MA toxicity compared to acute challenges in naïve animals (Segal et al., 2003; Cadet et al., 2011). In addition, the vast majority of former MA users in this study were also current smokers and pretreatment with either nicotine or tobacco smoke has also been shown to attenuate some measures of MA toxicity (Bondy et al., 2000; Ryan et al., 2001). These two factors have been suggested as potential explanations for some of the discrepancies between preclinical studies of MA toxicity and the relative lack of Parkinsonian symptoms in human MA users (Caligiuri and Buitenhuys, 2005). However, given the large effect on iron accumulation seen in response to small doses in the vervet monkeys compared to the null effect in the current study cohort with much greater total exposure to MA, it is likely that interspecies differences in brain iron accumulation explain the lack of effect in human MA users.

The current findings also relate to the interpretation of the study by Todd et

al. (2013) which reported that stimulant users show larger areas of echogenicity in the substantia nigra by ultrasound. In this report, they suggested that the increased echogenicity may be due to increased iron accumulation. Although echogenicity measures have been demonstrated to correlate with iron content in the substantia nigra, this association accounts for less than 10% of variance in substantia nigra iron content, suggesting it is not a very specific measure of iron (Zecca et al., 2004). The results of the current study suggest that the changes detected by ultrasound in stimulant users are not due to an increase in iron content and could be explained by other factors (Berg et al., 2010).

The MRI measures used in this study yielded values for iron content that were in substantial agreement with literature values (Table 4)(Hallgren and Sourander, 1958; Mitsumori et al., 2009; Langkammer et al., 2010). An exception to this was seen in the calculated whole-brain gray matter Fe values which were lower than expected based on literature values. The calculated relaxivity values for both r_{2fM} and r_{2Fe} were based on mean values of R_2 and f_M within identified ROIs and literature values of iron (Hallgren and Sourander, 1958), giving equal weighting to each region regardless of size. This modeling biases the iron estimates to be more precise for subcortical gray matter structures with high iron content compared to cortical areas. A more complete model could be obtained by parcellating cortical gray matter regions and applying region specific iron estimates for each cortical region (Hallgren and Sourander, 1958). The model estimates could also be improved by using values from individual voxels to

calculate relaxivity values as opposed to mean values within ROIs.

While this study was unable to detect group differences in brain iron content, it was able to detect age related changes in iron content consistent with previous studies, providing a positive control for this approach (Hallgren and Sourander, 1958; Bartzokis et al., 1997; Martin et al., 1998; Bartzokis et al., 2007a; Pfefferbaum et al., 2009). In this study, strong age associated increases in iron were seen consistently in the putamen. In this age range, the putamen has repeatedly been demonstrated to exhibit continued iron accumulation (Hallgren and Sourander, 1958; Schenker et al., 1993; Bartzokis et al., 1997; Bartzokis et al., 2007b; Xu et al., 2008; Pfefferbaum et al., 2009). Additionally, age related increases in R_2 and decreases in signal T_2-weighted signal intensity were also seen in other iron rich regions including the caudate and substantia nigra which have both been shown to accumulate iron over this age range (Hallgren and Sourander, 1958; Bartzokis et al., 2007a; Pfefferbaum et al., 2009), (however, some MRI methods have been unable to detect these changes (Xu et al., 2008; Pfefferbaum et al., 2009)). There was also a significant age associated decrease in the calculated iron in the frontal white matter, a finding consistent with multiple studies (Bartzokis et al., 2007b; Pfefferbaum et al., 2009). This study was unable to detect significant sex effects in any basal ganglia regions. Sex effects have been reported in the caudate, with men having higher levels of iron (Bartzokis et al., 2007b), but other studies have been unable to replicate this effect (Xu et al., 2008). This study also found effects of hemisphere on iron

96

measurements with the right hemisphere basal ganglia regions displaying increased iron content. While some studies have been unable to detect hemispheric differences using MRI measurements of iron (Vymazal et al., 1999; Wansapura et al., 1999; Pfefferbaum et al., 2009; Langkammer et al., 2010), others have reported left sided increases (Xu et al., 2008). Considering these slight discrepancies, the method of iron calculation used in this study yielded results that are in substantial agreement with other studies.

Similarly, the current approach to measuring f_M yielded measurements that were very consistent with previous reports (Table 3) (Koch, 1922; Randall, 1938; HIMWICH et al., 1955; Whittall et al., 1997; Gelman et al., 2001; Neeb et al., 2008; Abbas et al., 2014). Additionally, the age-associated increases of f_M closely mirror studies using quantitative T_1 and R_1 measurements (Agartz et al., 1991; Breger et al., 1991; Cho et al., 1997; Steen et al., 1997). While T_1 and R_1 are affected by both changes in iron and changes in f_M, the effect of f_M predominates (Rooney et al., 2007). Using these methods, several studies have shown that T_1 values in the caudate and thalamus decrease rapidly from birth through adolescence and continue to decrease through early adulthood, reaching a minimum in the fourth or fifth decade of life, followed by an increase in T_1 after the fifth decade (Agartz et al., 1991; Breger et al., 1991; Cho et al., 1997; Steen et al., 1997). This pattern is very consistent with the current findings of increased f_M (decreased f_W) over the study's age range (18-55).

Two unexpected group differences were seen in the voxelwise analysis of

f_M. MA subjects had a region of increased f_M on the superior aspect of the body of the corpus callosum and decreased f_M within thalamus compared to controls. The significant region on the superior corpus callosum appears to represent the gray white boundary between corpus callosum and cingulate cortex with most control subjects having f_M values more similar to gray matter and MA subjects having values that are closer to white matter. This finding is likely related to slight morphological differences in this region. The nonlinear registration approach used in this study is able to account for many variations in brain shape, however, this algorithm also utilizes a regularization component to the warp field, limiting the resolution of small deformations (Andersson et al., 2007a, b). If significant and systematic shape differences exist in this region, it is possible that the non-linear displacements used in the registration were inadequate to accurately account for this difference. Morphological differences in the shape of the corpus callosum have been reported in MA users, with MA users displaying increased curvature in genu and decreased width in the posterior midbody compared to controls (Oh et al., 2005). This latter finding corresponds well with the location of increased f_M in MA users found in the current study. Other studies have reported both cingulate atrophy and white hypertrophy which would both be consistent with this observed effect if it is due to systematic morphological differences between groups (Thompson et al., 2004).

However unlike this white matter finding, the group difference in thalamus f_M does not appear to be due to partial volume or edge effects from nearby

structures; instead, it appears to represent a substantial difference in tissue composition within the thalamus, with MA subjects having decreased f_M values and therefore increased tissue water content. In rodent models, acute MA toxicity has been shown to increase brain water content in several brain regions including the thalamus (Kiyatkin et al., 2007; Kiyatkin and Sharma, 2009; Sharma and Kiyatkin, 2009). This effect was highly correlated with both MA induced hyperthermia and blood brain barrier disruption, however, it is unclear if this effects persist past the acute phase (Kiyatkin and Sharma, 2009; Sharma and Kiyatkin, 2009). Using the positron emission tomography (PET) radio tracer [^{11}C] (R)-PK11195 in abstinent MA users, increased microglial activation has been demonstrated in several subcortical gray matter structures including the striatum and thalamus (Sekine et al., 2008), suggesting prolonged inflammatory processes in these regions. The thalamus has also been identified as a region with relative hypometabolism during early abstinence (<6 months) (Volkow et al., 2001; Rooney et al., 2007) followed by recovery during prolonged abstinence (>12 months) (Wang et al., 2004). The majority of the MA subjects in this study were abstinent less than 100 days, suggesting that if these two findings are related, changes in thalamus f_M may normalize with extended abstinence. Increased water content due to inflammation has also been proposed to explain increased striatal volumes (Chang et al., 2005; Chang et al., 2007) and altered diffusion characteristics of the putamen (Alicata et al., 2009) in former MA users. However, the current study was unable to detect decreased f_M in either of these

regions. Unlike measurements of iron, equivalence testing of the f_M measures was unable to rule out difference hypotheses in several of these regions as shown in **Table 6**. Additional confirmatory measures using similar proton density and T_1 approaches may be able to elucidate whether there are inflammatory changes leading to increased water content that persist in these regions.

In conclusion, this study demonstrated that human MA users do not have increased brain iron levels within basal ganglia regions compared to aged-matched healthy controls. This finding was supported by both quantitative R_2 measurements and additional calculations of iron content taking into consideration potential changes in brain water content that may accompany MA toxicity. This finding does not rule out a potential role of a small labile iron pool participating in MA induce oxidative stress, as suggested by preclinical studies (Yamamoto and Zhu, 1998; Park et al., 2006), however, it does suggest that in humans, MA exposure in not accompanied by a large change in brain iron accumulation as was previously reported in nonhuman primates (Melega et al., 2007). This study also demonstrated a novel approach to investigate alterations in brain iron content at the voxelwise level through the creation of parametric maps of iron distribution, integrating MRI information from both R_2 measurements and PD weighted images. Using this approach, an unexpected finding of increased tissue water was seen in the thalamus of MA users that may be related to prolonged inflammatory processes and additional studies are needed to confirm this finding.

Summary and Discussion

Methamphetamine (MA) abuse causes long term changes to the dopamine system that may result in addiction, mood disturbances, psychosis, and cognitive impairment. Damage to DA neurons is often accompanied by an increase in iron accumulation and evidence from preclinical studies suggests that iron is involved in MA toxicity. This project represents the first clinical investigation of the possible role of brain iron accumulation in MA toxicity in human subjects. In this project, I developed a novel method for creating parametric maps of iron content based on established quantitative MRI techniques; and used these techniques to determine if iron accumulation represents a functionally significant biomarker of MA toxicity. Contrary to my predicted hypothesis, I was unable to detect any group differences in regional brain iron content in abstinent MA users compared to aged-matched control subjects. In this chapter, I will review the accomplishments of this project and discuss the implications for future studies.

In **Chapter 1**, I reviewed the current evidence that iron is involved in MA toxicity; and explored several possible mechanisms by which MA could bring about alterations in iron handling; ultimately, leading to an increase in brain iron accumulation. In 2007,[8] Melega et al. demonstrated that acute administration of MA is able to dramatically increase iron and ferritin content within the pallidum

---

[8]   This project was originally presented 10 years before this publication at the annual meeting for the Society for Neuroscience (Burrows and Meshul, 1997) .

and substantia nigra in nonhuman primates. Their report represents the only study that has directly investigated the effects of MA on brain iron accumulation. However, indirect evidence that iron plays a role in MA toxicity has been shown in studies using the iron chelator, deferroxamine, as pretreatment (Yamamoto and Zhu, 1998; Park et al., 2006) as well as studies which indicate alterations in the expression of the iron storage protein, ferritin, following MA treatment (Cai et al., 2006; Sun et al., 2011; Shah et al., 2013). Increased iron accumulation was also offered as an explanation for a finding of increased substantia nigra echogenicity in stimulant users (Todd et al., 2013). In addition, there is a substantial body of literature which demonstrates that alterations in iron metabolism are common features of other dopaminergic neurotoxins (MPTP, 6-OHDA, lactacystin, aminochrome, etc.)(Salazar et al., 2008; Jiang et al., 2010; Carroll et al., 2011). Furthermore, preclinical studies suggest that MA toxicity is associated with several mechanisms that could potentially increase iron accumulation, including increased oxidative stress, proteasome impairment, mitochondrial dysfunction, microglial activation, and BBB disruption (Fornai et al., 2004a; Yamamoto and Raudensky, 2008; Kiyatkin and Sharma, 2009). These mechanisms are capable of altering the activity and availability of iron regulatory proteins, increasing iron accessibility and redistributing iron (Gerlach et al., 2006). However, most of the studies that investigate these mechanisms of MA toxicity use an acute neurotoxic model that may not accurately reflect the processes that are seen in human MA users (Davidson et al., 2001; Cadet et al., 2003; Segal et al., 2003; Cadet et al.,

2011). An exception to this is the study by Melega et al. (2007), which showed dramatic increases in iron accumulation in response a relatively small dose of MA (2 x 2 mg/kg). In their conclusion, they suggest the next logical study to follow up on this finding is to assess "whether a similar pattern...of iron accumulation occurs in basal ganglia of humans after METH or amphetamine exposure...with quantitative studies of iron content using MRI."

In **Chapter 2**, I reviewed basic MRI principles and quantitative techniques that can be applied to investigate brain iron content in human subjects and discussed the development of a novel approach to create parametric maps of iron distribution (**Figures 17 and 18**). Iron increases the transverse relaxation rate constant ($R_2 \equiv 1/T_2$) of nearby water protons; causing a loss of signal intensity on T_2-weighted images. The linear relationship between R_2 and brain iron content has been validated in postmortem studies (Hardy et al., 2005; Langkammer et al., 2010) and has enabled several researchers to investigate brain iron accumulation in aging and neurodegenerative diseases (Haacke et al., 2005; Dusek et al., 2013). Quantitative R_2 measurements require multiple T_2-weighted images acquired at different echo times in order to characterize the T_2 decay curve (**Figures 13 and 14**). While R_2 is strongly affected by iron content, it is also affected by the relative macromolecular fraction (f_M). A relaxivity model that incorporates terms for both of these effects can be shown to account for a greater portion of the variance in R_2 (Mitsumori et al., 2009). The f_M term is especially important when assessing conditions that could be associated with

increased tissue water content, including inflammation, edema, and tissue loss. Measurement of f_M can be accomplished using a proton density weighted image scaled by the intensity of cerebrospinal fluid to provide a map of the relative water content (f_W). This f_W map can then be transformed into a f_M map by simply subtracting it from unity ($1 - f_W \equiv f_M$) (**Figures 16a and 16b**). The relaxivity values for iron (r_{2Fe}) and f_M (r_{2fM}) can be estimated empirically using the measured R_2 and f_M values along with literature values of brain iron content (Hallgren and Sourander, 1958). Applying the expanded relaxivity model to these measures then allows for estimation of the regional iron content. This approach can then be applied at each voxel to create parametric maps of iron distribution (**Figures 17 and 18**); which allows for voxelwise analysis of regional iron content that could be used to investigate various disease processes that are thought to alter brain iron handling.

In **Chapter 3**, I described the prospective study in which I applied multiple *in vivo* MRI measures to investigate regional brain iron content in individuals with a history of MA abuse and aged matched, healthy control subjects. This study followed up preliminary findings from our group, which indicated that MA users had decreased T_2-weighted signal intensity in the striatum compared to age-matched controls (Berlow et al., 2011)(appendix 1). In the prospective study, MRI datasets were acquired from 27 currently abstinent MA users and 27 controls. Quantitative R_2 maps were created for 41 subjects (21 MA, 20 controls) using T_2-weighted, TSE images collected at three echo times. Calculated maps of f_M were

created from proton density weighted, 3D FLASH images that were obtained in 41 subjects (20 MA, 21 controls). Parametric maps of iron distribution were created, as described above, in 40 of these participants (20 MA, 20 controls). In addition, T_2-weighted signal intensity measurements were obtained from TRSE images from 51 of the subjects (26 MA and 25 controls) in an attempt to replicate and investigate our preliminary findings (Berlow et al., 2011). The effect of MA on these MRI measures was assessed using both region of interest analysis and voxel-wise linear models. It was predicted that subjects with a history of MA abuse would have evidence of increased brain iron content in basal ganglia regions using these MRI metrics. Using this approach, I was unable to detect any group differences in any of the MRI measures that would be consistent with differences in regional iron content. Equivalence testing was then used to provide support that the groups do not differ in their brain iron content by more than 25%, indicating that if there is an effect of MA on iron accumulation, it is small relative to the variance in brain iron content seen in individuals who do not use MA ($p_{equivalence}$ < 0.005 for all basal ganglia regions; **Table 6**)(Schuirmann, 1987; Hoenig and Heisey, 2001). The MRI techniques used in this study yielded measures of iron and f_M that were in substantial agreement with literature values. Also consistent with previous reports, strong age associated increases in iron content within basal ganglia regions were detected providing a positive control for these methods. These results imply that brain iron accumulation as assessed by MRI is not a robust biomarker of MA toxicity in human subjects.

This study was unable to replicate our preliminary retrospective study that utilized T_2-weighted signal intensity measurements as a surrogate for T_2 and R_2 in subjects with and without a history of MA abuse. In chapters 2 and 3, I highlight the limitations of T_2-weighted signal intensity measurements and demonstrate that they do not represent a quantitative measurement of R_2. T_2-weighted signal intensity measurements can be shown to track measured R_2 values, however, they also display additional variance due to unrelated factors, such as coil loading and RF calibration, and these factors may have played a role in the previous retrospective study. The current study used consistent acquisition parameters and improved registration and distortion correction techniques and was unable to detect any differences in T_2-weighted signal intensity between MA users and controls. Furthermore, using quantitative measurements of R_2 and f_M along with relaxometry models that are more specific for measuring iron content, the current study found no evidence of increased brain iron content in MA users.

This conclusion is in stark contrast to the nonhuman primate study conducted by Melega et al. (2007) that inspired this investigation. This discrepancy is likely due to interspecies differences in brain iron accumulation. In some old world monkey species, there is evidence that the pattern of age associated iron accumulation is notably different than the pattern seen in humans (Hardy et al., 2005; Berlow et al., 2012a). I investigated these patterns in 88 Japanese macaques and 43 human subjects using R_2 methods at 3T (Berlow et al., 2012a). In both species, iron increases rapidly in basal ganglia regions during

106

the first two decades of life and then begins to plateau. I modeled this pattern as an exponential function based on the models of Hallgren and Sourander (1958):

$$[Fe] = a\left[1 - e^{\left(\frac{-age}{k}\right)}\right] + c \tag{17}$$

Where a represents the asymptote of the maximum iron concentration in a given region; k represents the rate constant describing the speed with which the value a is approached as a function of age; and c represents the intercept for a given region (i.e iron concentration at birth). In the caudate, putamen and pallidum, the rate constants in the Japanese macaques were found to be similar to the rate constants seen in humans (Berlow et al., 2012a), implying that the rate of iron accumulation is dependent on calendar years as oppose to relative age. This means that unlike humans who reach their iron accumulation plateau in early adulthood, the macaques continue to be in a phase of rapid iron accumulation throughout their adulthood and into old age. In addition, the values for a, the maximum iron level for a given region, are much greater in macaque than those seen in humans. In the pallidum, the R_2 values are almost double those seen in humans, suggesting that these nonhuman primates attain brain iron concentrations that are much greater than the concentrations seen in human brains. Similar results have also been reported in another old world monkey species, the Rhesus macaque (Hardy et al., 2005). These studies suggest that there are significant species specific differences in brain iron accumulation patterns in old world monkeys when compared to humans.

These differences may explain the large discrepancy between the findings

of the (Hallgren and Sourander, 1958; Melega et al., 2007)study compared to the

current study in human primates. If vervet monkeys display a similar pattern of

iron accumulation as other old world monkey species, it is likely that young adult

monkeys (5 to 9 years old) would be in a phase of rapid brain iron accumulation,

during which changes to the rate or capacity of iron accumulation would be

readily evident. If MA affects the rate constant of iron accumulation (k) without

affecting maximum iron capacity of a given region (a), such an effect would be

detable only in that early phase of rapid iron accumulation and not observable

after the accumulation plateau is reached, which in humans is approximately 20

years old for the pallidum. In contrast, an increase in iron storage capacity (or an
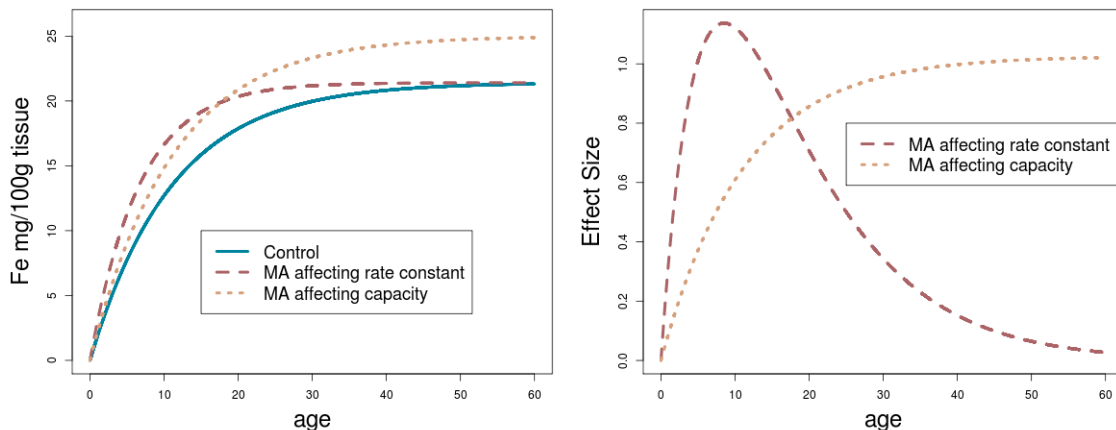
Figure 27:Hypothetical effects of methamphetamine (MA) on the pattern of iron accumulation in the pallidum.

If MA only affects the rate constant of iron accumulation (red), large group differences in iron levels would be seen at young ages, but not at later ages. If MA changed the maximum capacity of storage (yellow), then these differences would be expected to persist into adulthood. Estimated effect sizes from these two models (right) demonstrate the relative ability to detect these two effects at different ages.

increase in both rate and storage capacity) would result in group differences that would persist through adulthood. In **Figure 27**, I plot both of these possibilities for the human pallidum using estimates from Hallgren and Sourander (1958). This figure suggests that a change in the rate constant of iron accumulation would dramatically increase iron levels at very young ages (~5-15 years old), but would have little effect on iron levels in older individuals. This interpretation would explain the discrepancy between the current study and the findings of the Melega et al. (2007). It would also suggest that an effect of MA on iron accumulation may be detectable in adolescent MA users. However, the functional significance of this effect is still unclear because it would not be expected to result in a difference in adult levels of brain iron content.

Exposure to other substances, especially tobacco, may also play a role in brain iron accumulation associated with MA abuse. The prevalence of current tobacco use among MA users has been reported to be between 86-92% and the prevalence of lifetime history of regular tobacco use among MA users approaches 94% (Grant et al., 2007; Weinberger and Sofuoglu, 2009). Consistent with these findings, almost all of the MA subjects in this study were also current smokers. The effects of cigarette smoking on brain iron accumulation are largely unknown; and the effects of the combination of MA and smoking are completely unknown. Preclinical studies suggest that pretreatment with either nicotine or tobacco smoke attenuates some measures of MA toxicity (Ryan et al., 2001). Additionally, epidemiological studies suggest that smoking is associated

with decreased risk of Parkinson's disease, suggesting a protective role of smoking on dopamine neurons (Morens et al., 1995). If increased brain iron accumulation is primarily a response to damaged neurons and tobacco and nicotine provide some protection against MA induced toxicity in these neurons, the co-administration of tobacco and MA may result in protection from both neuronal damage and subsequent brain iron accumulation. Findings from the current study are consistent with this hypothesis and suggest that MA users who smoke do not have significantly increased brain iron levels compared to a mixed group of smokers and nonsmokers who don't use MA.

Alternatively, cigarette smoking may have other effects on systemic iron metabolism that could also affect brain iron handling. Cigarette smoke is a complex aerosol of over 4000 compounds resulting from the pyrolysis and partial combustion of tobacco, paper, and cigarette additives. Incomplete combustion of a cigarette results in multiple compounds with oxygen-containing functional groups that can complex with iron (Fe^{3+}) in the lung (Ghio et al., 2008). Some of this iron could come from the cigarette smoke itself, as tobacco contains small amounts iron (440-1150 ug/g) and mainstream smoke contains 0.06% of that iron (Mussalo-Rauhamaa et al., 1986). Additional iron is likely recruited to the lung from the body's iron pool stimulated by the oxidative stress of the particulate matter from the smoke via activated IRP-1. Regardless of the sources of this iron, smoking leads to accumulation of iron within the lung. Bronchoalveolar lavages from smokers contain significantly more iron than nonsmokers

(McGowan and Henley, 1988). This increase in lung iron has been shown to have a dose response relationship with pack years (McGowan and Henley, 1988). Smokers also show signs of systemic iron accumulation including increased serum iron and ferritin levels, increased transferrin saturation and decreased ceruplasmin ferroxidase activity (Ghio et al., 2008). Rats exposed to cigarette smoke displayed a 33% increase in their total brain iron content (Anbarasi et al., 2006). In a separate retrospective study, I investigated the relationship between smoking history and basal ganglia R_2 values in 83 healthy elderly subjects; and found that individuals with a long term smoking history (>23 years) had increased R_2 values in the caudate and putamen compared to nonsmokers and former smokers with shorter smoking histories; suggesting a potential relationship between smoking and increased brain iron content (Berlow et al., 2014). However, this effect was not seen in the current study. Nevertheless, the frequency of tobacco use among MA users necessitates increased consideration of the potential roles of nicotine and tobacco smoke in MA toxicity in both preclinical and clinical studies. One strategy for accomplishing this in human studies is to include three groups, MA, control smokers and control nonsmokers, as illustrated in the approach used by Morales et al. (2012).

While there were no group differences in measured iron content, an unexpected group difference was seen in thalamus f_M values, with MA subjects showing reduced f_M (**Figures 21 and 22**). This finding is consistent with an increase in the relative tissue water content in MA subjects. Alternatively, lower f_M

measurements may represent a delay or failure of normal brain maturation processes associated with myelination. Increased brain water content has been associated with BBB disruption and hyperthermia in rodent models of acute MA toxicity (Kiyatkin and Sharma, 2009). In addition, the thalamus has been identified as a region that undergoes metabolic changes during different periods of abstinence from MA, with relative hypometabolism in early abstinence followed by partial recovery with prolonged abstinence (Volkow et al., 2001; Wang et al., 2004). Increased microglial activation has also been reported in the thalamus of abstinent MA users using the PET tracer [^{11}C](R)-PK11195, indicating that inflammatory processes could still be occurring during abstinence (Sekine et al., 2008). The focal nature of this finding in the thalamus (**Figures 21)** along with a lack of differences in f_M in other regions suggests it is not due to a global change in tissue water content. Additional studies are needed to replicate and investigate this finding. One approach would be to use quantitative R_1 mapping which should yield very similar results if this finding represents a true difference in f_M (Rooney et al., 2007). Advantages of an R_1 approach over the current PD method include the fact that R_1 mapping is associated with increase signal to noise and it does not require a rescaling of intensity values.

This study did find strong age associated increases in iron that were seen in the basal ganglia regions, most strongly in the putamen. Iron affects the signal properties of most of the popular neuroimaging techniques used to investigate functional and structural aspects of the brain (Sullivan et al., 2009; Pfefferbaum

et al., 2010). Iron enhances transverse relaxation processes, reducing the signal to noise ratio of the base images used in diffusion tensor imaging and functional BOLD imaging. This effect needs to be considered when interpreting any study that reports differences in brain regions that could associated with systematic alterations in iron content, such as those seen in aging and development (Sullivan et al., 2009; Pfefferbaum et al., 2010). For example, decreased signal to noise due to iron could result in decreased ability to detect correlations among voxels in an fMRI study; leading to the misinterpretation that the data indicate reduced striatal activation in older individuals when this effect actually has nothing to do with differences in hemodynamic processes. One approach to control for this might involve creating maps of the signal to noise ratio (SNR) of the base images by dividing the base image by the standard deviation of the noise. This would allow researchers to ensure there are not systematic and regional differences in SNR between groups that could lead erroneous interpretation of group differences. Appreciation of this effect will likely grow with the gaining popularity of high field MRI scanners. Fortunately, the results of the current study do not indicate the need to re-evaluate all MA imaging studies for the role of systematic differences in iron content.

The methods developed during this project to create and analyze quantitative maps of brain iron content represent a significant advance in the field. The resulting maps created with this approach can be compared with the methods used by Bartzokis and collegues, in which R_2 maps are acquired at

different field strengths (1.5T and 3T) to create maps of the field dependent relaxation rate increase (FDRI) (Bartzokis et al., 1993; Bartzokis et al., 1994; Bartzokis et al., 1997; Bartzokis et al., 1999; Bartzokis et al., 2004; Bartzokis et al., 2007a; Bartzokis et al., 2011). The FDRI maps and the parametric iron maps used in this study both exhibit strong correlations with estimated brain iron levels (Hallgren and Sourander, 1958; Sekine et al., 2008) and visually appear to reflect the same specificity for iron. However, unlike the FDRI approach, the method used in this study requires only a single scanning session at a single field strength, limiting the demands on the subjects, reducing the cost of the study and making this approach more appropriate for the development of clinical applications.

The methods and findings from this project suggest several directions for future studies. First, the interaction between MA toxicity and iron handling is still poorly understood and largely uninvestigated at the basic science level. Several potential mechanisms are presented in **Chapter 1**, illustrating how MA toxicity could affect the expression and action of iron regulatory proteins, leading to altered iron levels. Each of these mechanisms could be investigated using approaches that have been successfully applied using other dopaminergic neurotoxins (Pantopoulos et al., 1996; Melega et al., 2007; Salazar et al., 2008; Jiang et al., 2010; Carroll et al., 2011)This project also suggests the application of MRI techniques in preclinical studies of MA administration. Such studies would allow for longitudinal assessment of MA induced iron accumulation and allow for

a behavioral assessment of the functional significance of this effect. Finally, given the possiblity that changes in the rate constant of brain iron accumulation may only be detectable in the first two decades of life, a study of adolescence MA users may be able to better characterize this effect.

The translation of research findings from preclinical studies to human subjects represents one of the ultimate goals of substance abuse research and an important step in the development of therapy and treatment strategies. Although, human subject research is often confounded by a lack of experimental control, it offers the possibility of very direct insight into the significant factors affecting individuals with substance abuse disorders. Results of such studies can then inform the design and implementation of more accurate and relevant models. In this project, I investigated the possible role of brain iron accumulation in individuals with MA dependence using MRI techniques in order to determine if a change in iron accumulation represents a functionally significant biomarker of MA toxicity. Increased brain iron content has been associated with a number of neurological disorders and findings from preclinical studies suggest that most substances which cause selective damage to dopaminergic neurons result in increased iron accumulation. To assess this in human subjects, I developed an approach to create maps of brain iron content based on relaxometry models that account for effects due to iron and the fractional macromolecular content. I applied this MRI approach to 20 abstinent MA users and 20 aged-matched control subjects and collected additional confirmatory MRI measures of iron (R_2

and T_2 signal intensity) in a larger cohort. Using both region of interest and voxelwise analyses, I was unable to detect any group differences in any of the MRI measures that would be consistent with differences in regional iron content. Subsequent equivalence testing confirmed that group differences if present are not large compared to the normal variation in brain iron content. These results strongly suggest that iron accumulation as assessed by MRI is not a robust biomarker of MA toxicity.

References

Abbas, Z., Gras, V., Möllenhoff, K., Keil, F., Oros-Peusquens, A.-M., and Shah, N.J. (2014) Analysis of proton-density bias corrections based on T1 measurement for robust quantification of water content in the brain at 3 Tesla.. Magn Reson Med, , .

Abekawa, T., Ohmori, T., and Koyama, T. (1994) Effects of repeated administration of a high dose of methamphetamine on dopamine and glutamate release in rat striatum and nucleus accumbens.. Brain Res, 643, 276-281.

Agartz, I., Sääf, J., Wahlund, L.O., and Wetterberg, L. (1991) T1 and T2 relaxation time estimates in the normal human brain.. Radiology, 181, 537-543.

Aguirre, P., Urrutia, P., Tapia, V., Villa, M., Paris, I., Segura-Aguilar, J., and Núñez, M.T. (2012) The dopamine metabolite aminochrome inhibits mitochondrial complex I and modifies the expression of iron transporters DMT1 and FPN1.. Biometals, 25, 795-803.

Ali, S.F., Newport, G.D., Holson, R.R., Slikker, W., and Bowyer, J.F. (1994) Low environmental temperatures or pharmacologic agents that produce hypothermia decrease methamphetamine neurotoxicity in mice.. Brain Res, 658, 33-38.

Alicata, D., Chang, L., Cloak, C., Abe, K., and Ernst, T. (2009) Higher diffusion in striatum and lower fractional anisotropy in white matter of methamphetamine users.. Psychiatry Res, 174, 1-8.

American Psychiatric Association (APA), (1994) *Diagnostic and statistical manual of mental disorders (4th ed.)*. American Psychiatric Association, .

Anbarasi, K., Vani, G., Balakrishna, K., and Devi, C.S.S. (2006) Effect of bacoside A on brain antioxidant status in cigarette smoke exposed rats.. Life Sci, 78, 1378-1384.

Andersson, J., Jenkinson, M., and Smith., S. (2007a) Non-linear registration, aka Spatial normalisation. FMRIB technical report TR07JA2 from www.fmrib.ox.ac.uk/analysis/techrep.

Andersson, J.L.R., Jenkinson, M., and Smith, S. (2007b) Non-linear optimisation..FMRIB technical report TR07JA1 from www.fmrib.ox.ac.uk/analysis/techrep.

Ares-Santos, S., Granado, N., Espadas, I., Martinez-Murillo, R., and Moratalla, R. (2014) Methamphetamine causes degeneration of dopamine cell bodies and terminals of the nigrostriatal pathway evidenced by silver staining.. Neuropsychopharmacology, 39, 1066-1080.

Ashburner, J., and Friston, K.J. (2005) Unified segmentation.. Neuroimage, 26, 839-851.

Atasoy, H.T., Nuyan, O., Tunc, T., Yorubulut, M., Unal, A.E., and Inan, L.E. (2004) T2-weighted MRI in Parkinson's disease; substantia nigra pars compacta

hypointensity correlates with the clinical scores.. Neurol India, 52, 332-337.

Ayata, C., Ayata, G., Hara, H., Matthews, R.T., Beal, M.F., Ferrante, R.J., Endres, M., Kim, A., Christie, R.H., Waeber, C., Huang, P.L., Hyman, B.T., and Moskowitz, M.A. (1997) Mechanisms of reduced striatal NMDA excitotoxicity in type I nitric oxide synthase knock-out mice.. J Neurosci, 17, 6908-6917.

Açikgöz, O., Gönenç, S., Kayatekin, B.M., Uysal, N., Pekçetin, C., Semin, I., and Güre, A. (1998) Methamphetamine causes lipid peroxidation and an increase in superoxide dismutase activity in the rat striatum.. Brain Res, 813, 200-202.

Barkovich, A.J. (2005) Magnetic resonance techniques in the assessment of myelin and myelination.. J Inherit Metab Dis, 28, 311-343.

Bartzokis, G., Aravagiri, M., Oldendorf, W.H., Mintz, J., and Marder, S.R. (1993) Field dependent transverse relaxation rate increase may be a specific measure of tissue iron stores.. Magn Reson Med, 29, 459-464.

Bartzokis, G., Beckson, M., Hance, D.B., Marx, P., Foster, J.A., and Marder, S.R. (1997) MR evaluation of age-related increase of brain iron in young adult and older normal males.. Magn Reson Imaging, 15, 29-35.

Bartzokis, G., Cummings, J.L., Markham, C.H., Marmarelis, P.Z., Treciokas, L.J., Tishler, T.A., Marder, S.R., and Mintz, J. (1999) MRI evaluation of brain iron in earlier- and later-onset Parkinson's disease and normal subjects.. Magn Reson Imaging, 17, 213-222.

Bartzokis, G., Lu, P.H., Tingus, K., Peters, D.G., Amar, C.P., Tishler, T.A., Finn, J.P., Villablanca, P., Altshuler, L.L., Mintz, J., Neely, E., and Connor, J.R. (2011) Gender and iron genes may modify associations between brain iron and memory in healthy aging.. Neuropsychopharmacology, 36, 1375-1384.

Bartzokis, G., Lu, P.H., Tishler, T.A., Fong, S.M., Oluwadara, B., Finn, J.P., Huang, D., Bordelon, Y., Mintz, J., and Perlman, S. (2007b) Myelin breakdown and iron changes in Huntington's disease: pathogenesis and treatment implications.. Neurochem Res, 32, 1655-1664.

Bartzokis, G., Sultzer, D., Mintz, J., Holt, L.E., Marx, P., Phelan, C.K., and Marder, S.R. (1994) In vivo evaluation of brain iron in Alzheimer's disease and normal subjects using MRI.. Biol Psychiatry, 35, 480-487.

Bartzokis, G., Tishler, T.A., Lu, P.H., Villablanca, P., Altshuler, L.L., Carter, M., Huang, D., Edwards, N., and Mintz, J. (2007a) Brain ferritin iron may influence age- and gender-related risks of neurodegeneration.. Neurobiol Aging, 28, 414-423.

Bartzokis, G., Tishler, T.A., Shin, I.-S., Lu, P.H., and Cummings, J.L. (2004) Brain ferritin iron as a risk factor for age at onset in neurodegenerative diseases.. Ann N Y Acad Sci, 1012, 224-236.

Beard, J. (2003) Iron deficiency alters brain development and functioning.. J Nutr, 133, 1468S-1472S.

Beard, J.L., Wiesinger, J.A., Li, N., and Connor, J.R. (2005) Brain iron uptake in hypotransferrinemic mice: influence of systemic iron status.. J Neurosci Res, 79, 254-261.

Beckman, J.S., Beckman, T.W., Chen, J., Marshall, P.A., and Freeman, B.A. (1990) Apparent hydroxyl radical production by peroxynitrite: implications for endothelial injury from nitric oxide and superoxide.. Proc Natl Acad Sci U S A, 87, 1620-1624.

Ben-Shachar, D., Eshel, G., Finberg, J.P., and Youdim, M.B. (1991) The iron chelator desferrioxamine (Desferal) retards 6-hydroxydopamine-induced degeneration of nigrostriatal dopamine neurons.. J Neurochem, 56, 1441-1444.

Ben-Shachar, D., and Youdim, M.B. (1991) Intranigral iron injection induces behavioral and biochemical "parkinsonism" in rats.. J Neurochem, 57, 2133-2135.

Ben-Shachar, D., Zuk, R., and Glinka, Y. (1995) Dopamine neurotoxicity: inhibition of mitochondrial respiration.. J Neurochem, 64, 718-723.

Berg, D. (2011) Substantia nigra hyperechogenicity is a risk marker of Parkinson's disease: yes.. J Neural Transm, 118, 613-619.

Berg, D., Behnke, S., Seppi, K., Godau, J., Lerche, S., Mahlknecht, P., Liepelt-Scarfone, I., Pausch, C., Schneider, N., Gaenslen, A., Brockmann, K., Srulijes, K., Huber, H., Wurster, I., Stockner, H., Kiechl, S., Willeit, J., Gasperi, A., Fassbender, K., Gasser, T., and Poewe, W. (2013) Enlarged hyperechogenic substantia nigra as a risk marker for Parkinson's disease.. Mov Disord, 28, 216-219.

Berg, D., Godau, J., Riederer, P., Gerlach, M., and Arzberger, T. (2010) Microglia activation is related to substantia nigra echogenicity.. J Neural Transm, 117, 1287-1292.

Berg, D., Roggendorf, W., Schröder, U., Klein, R., Tatschner, T., Benz, P., Tucha, O., Preier, M., Lange, K.W., Reiners, K., Gerlach, M., and Becker, G. (2002) Echogenicity of the substantia nigra: association with increased iron content and marker for susceptibility to nigrostriatal injury.. Arch Neurol, 59, 999-1005.

Berlow, Y.A., Kohama, S., Pollaro, J., Sammi, M., and Rooney, W. (2012a) Brain Iron Levels Across the Japanese Macaque Lifespan. Proceedings of the International Society for Magnetic Resonance in Medicine, 20: 3741, .

Berlow, Y.A., Lahna, D., Schwartz, D., Mitchell, A., Stevens, A., Rooney, W., and Hoffman, W. (2011) Increased striatal iron accumulation in human methamphetamine users.. Proceedings of the International Society for Magnetic Resonance in Medicine, 19, 2520.

Berlow, Y.A., Lahna, D.L., Schwartz, D.L., Woltjer, R.L., Guariglia, R.L., Silbert, L.C., Kaye, J.A., and Rooney, W.D. (2014) Brain Iron Content and Smoking History in Healthy Older Individuals. Proceedings of the International Society for Magnetic Resonance in Medicine, 22: 4677, .

Berlow, Y.A., Pollaro, J., Krisky, C., Grinstead, J., Snodgrass, M., Kohout, K., Lewis, M.S., Wilmington, D., Hutter, M., Casiana, L., Fitzpatrick, M., Lilly, D.J., Fausti, S., Folmer, R., Bourdette, D., and Rooney, W.D. (2012b) Magnetic Resonance Imaging Correlates of Dichotic Listening Performance in Multiple

Sclerosis. Seminars in Hearing, 33(3), 283-294.

Berman, S., O'Neill, J., Fears, S., Bartzokis, G., and London, E.D. (2008) Abuse of amphetamines and structural abnormalities in the brain.. Ann N Y Acad Sci, 1141, 195-220.

Block, M.L., Zecca, L., and Hong, J.-S. (2007) Microglia-mediated neurotoxicity: uncovering the molecular mechanisms.. Nat Rev Neurosci, 8, 57-69.

Blum, D., Torch, S., Lambeng, N., Nissou, M., Benabid, A.L., Sadoul, R., and Verna, J.M. (2001) Molecular pathways involved in the neurotoxicity of 6-OHDA, dopamine and MPTP: contribution to the apoptotic theory in Parkinson's disease.. Prog Neurobiol, 65, 135-172.

Bondy, S.C., Ali, S.F., and Kleinman, M.T. (2000) Exposure of mice to tobacco smoke attenuates the toxic effect of methamphetamine on dopamine systems.. Toxicol Lett, 118, 43-46.

Brass, S.D., Benedict, R.H.B., Weinstock-Guttman, B., Munschauer, F., and Bakshi, R. (2006) Cognitive impairment is associated with subcortical magnetic resonance imaging grey matter T2 hypointensity in multiple sclerosis.. Mult Scler, 12, 437-444.

Breger, R.K., Yetkin, F.Z., Fischer, M.E., Papke, R.A., Haughton, V.M., and Rimm, A.A. (1991) T1 and T2 in the cerebrum: correlation with age, gender, and demographic factors.. Radiology, 181, 545-547.

Brodie, J.D., Figueroa, E., Laska, E.M., and Dewey, S.L. (2005) Safety and efficacy of gamma-vinyl GABA (GVG) for the treatment of methamphetamine and/or cocaine addiction.. Synapse, 55, 122-125.

Brown, J.M., Quinton, M.S., and Yamamoto, B.K. (2005) Methamphetamine-induced inhibition of mitochondrial complex II: roles of glutamate and peroxynitrite.. J Neurochem, 95, 429-436.

Brown, J.M., and Yamamoto, B.K. (2003) Effects of amphetamines on mitochondrial function: role of free radicals and oxidative stress.. Pharmacol Ther, 99, 45-53.

Buchanan, J.B., Sparkman, N.L., and Johnson, R.W. (2010) Methamphetamine sensitization attenuates the febrile and neuroinflammatory response to a subsequent peripheral immune stimulus.. Brain Behav Immun, 24, 502-511.

Burrows, K.B., Gudelsky, G., and Yamamoto, B.K. (2000) Rapid and transient inhibition of mitochondrial function following methamphetamine or 3,4-methylenedioxymethamphetamine administration.. Eur J Pharmacol, 398, 11-18.

Burrows, K.B., and Meshul, C.K. (1997) Methamphetamine alters presynaptic glutamate immunoreactivity in the caudate nucleus and motor cortex.. Synapse, 27, 133-144.

Burrows, K.B., and Meshul, C.K. (1999) High-dose methamphetamine treatment alters presynaptic GABA and glutamate immunoreactivity.. Neuroscience, 90, 833-850.

Cadet, J.L., and Brannock, C. (1998) Free radicals and the pathobiology of brain

dopamine systems.. Neurochem Int, 32, 117-131.

Cadet, J.L., Brannock, C., Ladenheim, B., McCoy, M.T., Beauvais, G., Hodges, A.B., Lehrmann, E., Wood, W.H., Becker, K.G., and Krasnova, I.N. (2011) Methamphetamine preconditioning causes differential changes in striatal transcriptional responses to large doses of the drug.. Dose Response, 9, 165-181.

Cadet, J.L., Jayanthi, S., and Deng, X. (2003) Speed kills: cellular and molecular bases of methamphetamine-induced nerve terminal degeneration and neuronal apoptosis.. FASEB J, 17, 1775-1788.

Cai, N.S., McCoy, M.T., Ladenheim, B., Lyles, J., Ali, S.F., and Cadet, J.L. (2006) Serial analysis of gene expression in the rat striatum following methamphetamine administration.. Ann N Y Acad Sci, 1074, 13-30.

Caligiuri, M.P., and Buitenhuys, C. (2005) Do preclinical findings of methamphetamine-induced motor abnormalities translate to an observable clinical phenotype?. Neuropsychopharmacology, 30, 2125-2134.

Callaghan, R.C., Cunningham, J.K., Sykes, J., and Kish, S.J. (2012) Increased risk of Parkinson's disease in individuals hospitalized with conditions related to the use of methamphetamine or other amphetamine-type drugs.. Drug Alcohol Depend, 120, 35-40.

Carroll, C.B., Zeissler, M.-L., Chadborn, N., Gibson, K., Williams, G., Zajicek, J.P., Morrison, K.E., and Hanemann, C.O. (2011) Changes in iron-regulatory gene expression occur in human cell culture models of Parkinson's disease.. Neurochem Int, 59, 73-80.

Cass, W.A., Grondin, R., Andersen, A.H., Zhang, Z., Hardy, P.A., Hussey-Andersen, L.K., Rayens, W.S., Gerhardt, G.A., and Gash, D.M. (2007) Iron accumulation in the striatum predicts aging-related decline in motor function in rhesus monkeys.. Neurobiol Aging, 28, 258-271.

Castelnau, P.A., Garrett, R.S., Palinski, W., Witztum, J.L., Campbell, I.L., and Powell, H.C. (1998) Abnormal iron deposition associated with lipid peroxidation in transgenic mice expressing interleukin-6 in the brain.. J Neuropathol Exp Neurol, 57, 268-282.

Ceccarelli, A., Filippi, M., Neema, M., Arora, A., Valsasina, P., Rocca, M.A., Healy, B.C., and Bakshi, R. (2009) T2 hypointensity in the deep gray matter of patients with benign multiple sclerosis.. Mult Scler, 15, 678-686.

Chan, P., Monte, D.A.D., Luo, J.J., DeLanney, L.E., Irwin, I., and Langston, J.W. (1994) Rapid ATP loss caused by methamphetamine in the mouse striatum: relationship between energy impairment and dopaminergic neurotoxicity.. J Neurochem, 62, 2484-2487.

Chang, L., Alicata, D., Ernst, T., and Volkow, N. (2007) Structural and metabolic brain changes in the striatum associated with methamphetamine abuse.. Addiction, 102 Suppl 1, 16-32.

Chang, L., Cloak, C., Patterson, K., Grob, C., Miller, E.N., and Ernst, T. (2005) Enlarged striatum in abstinent methamphetamine abusers: a possible

compensatory response.. Biol Psychiatry, 57, 967-974.

Cheah, J.H., Kim, S.F., Hester, L.D., Clancy, K.W., Patterson, S.E., Papadopoulos, V., and Snyder, S.H. (2006) NMDA receptor-nitric oxide transmission mediates neuronal iron homeostasis via the GTPase Dexras1.. Neuron, 51, 431-440.

Cho, A.K., and Melega, W.P. (2002) Patterns of methamphetamine abuse and their consequences.. J Addict Dis, 21, 21-34.

Cho, S., Jones, D., Reddick, W.E., Ogg, R.J., and Steen, R.G. (1997) Establishing norms for age-related changes in proton T1 of human brain tissue in vivo.. Magn Reson Imaging, 15, 1133-1143.

Connor, J.R., Menzies, S.L., Martin, S.M.S., and Mufson, E.J. (1990) Cellular distribution of transferrin, ferritin, and iron in normal and aged human brains.. J Neurosci Res, 27, 595-611.

Cubells, J.F., Rayport, S., Rajendran, G., and Sulzer, D. (1994) Methamphetamine neurotoxicity involves vacuolation of endocytic organelles and dopamine-dependent intracellular oxidative stress.. J Neurosci, 14, 2260-2271.

Davidson, C., Gow, A.J., Lee, T.H., and Ellinwood, E.H. (2001) Methamphetamine neurotoxicity: necrotic and apoptotic mechanisms and relevance to human abuse and treatment.. Brain Res Brain Res Rev, 36, 1-22.

Davis, G.C., Williams, A.C., Markey, S.P., Ebert, M.H., Caine, E.D., Reichert, C.M., and Kopin, I.J. (1979) Chronic Parkinsonism secondary to intravenous injection of meperidine analogues.. Psychiatry Res, 1, 249-254.

Dawson, V.L., Dawson, T.M., London, E.D., Bredt, D.S., and Snyder, S.H. (1991) Nitric oxide mediates glutamate neurotoxicity in primary cortical cultures.. Proc Natl Acad Sci U S A, 88, 6368-6371.

DeMarco, A., Dalal, R.M., Pai, J., Aquilina, S.D., Mullapudi, U., Hammel, C., Kothari, S.K., Kahanda, M., Liebling, C.N.B., Patel, V., Schiffer, W.K., Brodie, J.D., and Dewey, S.L. (2009) Racemic gamma vinyl-GABA (R,S-GVG) blocks methamphetamine-triggered reinstatement of conditioned place preference.. Synapse, 63, 87-94.

Ding, B., Chen, K.-M., Ling, H.-W., Sun, F., Li, X., Wan, T., Chai, W.-M., Zhang, H., Zhan, Y., and Guan, Y.-J. (2009) Correlation of iron in the hippocampus with MMSE in patients with Alzheimer's disease.. J Magn Reson Imaging, 29, 793-798.

Double, K.L., Maywald, M., Schmittel, M., Riederer, P., and Gerlach, M. (1998) In vitro studies of ferritin iron release and neurotoxicity.. J Neurochem, 70, 2492-2499.

Dusek, P., Dezortova, M., and Wuerfel, J. (2013) Imaging of iron.. Int Rev Neurobiol, 110, 195-239.

Fitzmaurice, P.S., Tong, J., Yazdanpanah, M., Liu, P.P., Kalasinsky, K.S., and Kish, S.J. (2006) Levels of 4-hydroxynonenal and malondialdehyde are increased in brain of human chronic users of methamphetamine.. J Pharmacol

Exp Ther, 319, 703-709.

Flora, G., Lee, Y.W., Nath, A., Maragos, W., Hennig, B., and Toborek, M. (2002) Methamphetamine-induced TNF-alpha gene expression and activation of AP-1 in discrete regions of mouse brain: potential role of reactive oxygen intermediates and lipid peroxidation.. Neuromolecular Med, 2, 71-85.

Fornai, F., Lazzeri, G., Lenzi, P., Gesi, M., Ferrucci, M., Soldani, P., Pellegrini, A., Capobianco, L., Blasi, A.D., Ruggieri, S., and Paparelli, A. (2003) Amphetamines induce ubiquitin-positive inclusions within striatal cells.. Neurol Sci, 24, 182-183.

Fornai, F., Lazzeri, G., Poggio, A.B.D., Soldani, P., Blasi, A.D., Nicoletti, F., Ruggieri, S., and Paparelli, A. (2006) Convergent roles of alpha-synuclein, DA metabolism, and the ubiquitin-proteasome system in nigrostriatal toxicity.. Ann N Y Acad Sci, 1074, 84-89.

Fornai, F., Lenzi, P., Ferrucci, M., Lazzeri, G., di Poggio, A.B., Natale, G., Busceti, C.L., Biagioni, F., Giusiani, M., Ruggieri, S., and Paparelli, A. (2005) Occurrence of neuronal inclusions combined with increased nigral expression of alpha-synuclein within dopaminergic neurons following treatment with amphetamine derivatives in mice.. Brain Res Bull, 65, 405-413.

Fornai, F., Lenzi, P., Gesi, M., Ferrucci, M., Lazzeri, G., Capobianco, L., de Blasi, A., Battaglia, G., Nicoletti, F., Ruggieri, S., and Paparelli, A. (2004a) Similarities between methamphetamine toxicity and proteasome inhibition.. Ann N Y Acad Sci, 1025, 162-170.

Fornai, F., Lenzi, P., Gesi, M., Soldani, P., Ferrucci, M., Lazzeri, G., Capobianco, L., Battaglia, G., Blasi, A.D., Nicoletti, F., and Paparelli, A. (2004b) Methamphetamine produces neuronal inclusions in the nigrostriatal system and in PC12 cells.. J Neurochem, 88, 114-123.

Garthwaite, J. (1991) Glutamate, nitric oxide and cell-cell signalling in the nervous system.. Trends Neurosci, 14, 60-67.

Gelman, N., Ewing, J.R., Gorell, J.M., Spickler, E.M., and Solomon, E.G. (2001) Interregional variation of longitudinal relaxation rates in human brain at 3.0 T: relation to estimated iron and water contents.. Magn Reson Med, 45, 71-79.

Gerasimov, M.R., Ashby, C.R., Gardner, E.L., Mills, M.J., Brodie, J.D., and Dewey, S.L. (1999) Gamma-vinyl GABA inhibits methamphetamine, heroin, or ethanol-induced increases in nucleus accumbens dopamine.. Synapse, 34, 11-19.

Gerlach, M., Ben-Shachar, D., Riederer, P., and Youdim, M.B. (1994) Altered brain metabolism of iron as a cause of neurodegenerative diseases?. J Neurochem, 63, 793-807.

Gerlach, M., Double, K.L., Youdim, M.B.H., and Riederer, P. (2006) Potential sources of increased iron in the substantia nigra of parkinsonian patients.. J Neural Transm Suppl, , 133-142.

Ghio, A.J., Hilborn, E.D., Stonehuerner, J.G., Dailey, L.A., Carter, J.D., Richards, J.H., Crissman, K.M., Foronjy, R.F., Uyeminami, D.L., and Pinkerton, K.E.

(2008) Particulate matter in cigarette smoke alters iron homeostasis to produce a biological effect.. Am J Respir Crit Care Med, 178, 1130-1138.

Gluck, M.R., Moy, L.Y., Jayatilleke, E., Hogan, K.A., Manzino, L., and Sonsalla, P.K. (2001) Parallel increases in lipid and protein oxidative markers in several mouse brain regions after methamphetamine treatment.. J Neurochem, 79, 152-160.

Grant, K.M., Kelley, S.S., Agrawal, S., Meza, J.L., Meyer, J.R., and Romberger, D.J. (2007) Methamphetamine use in rural Midwesterners.. Am J Addict, 16, 79-84.

Greve, D.N., and Fischl, B. (2009) Accurate and robust brain image alignment using boundary-based registration.. Neuroimage, 48, 63-72.

Guo, B., Phillips, J.D., Yu, Y., and Leibold, E.A. (1995) Iron regulates the intracellular degradation of iron regulatory protein 2 by the proteasome.. J Biol Chem, 270, 21645-21651.

Haacke, E.M., Cheng, N.Y.C., House, M.J., Liu, Q., Neelavalli, J., Ogg, R.J., Khan, A., Ayaz, M., Kirsch, W., and Obenaus, A. (2005) Imaging iron stores in the brain using magnetic resonance imaging.. Magn Reson Imaging, 23, 1-25.

Hallgren, B., and Sourander, P. (1958) The effect of age on the non-haemin iron in the human brain.. J Neurochem, 3, 41-51.

Hardy, P.A., Gash, D., Yokel, R., Andersen, A., Ai, Y., and Zhang, Z. (2005) Correlation of R2 with total iron concentration in the brains of rhesus monkeys.. J Magn Reson Imaging, 21, 118-127.

Hare, D.J., Adlard, P.A., Doble, P.A., and Finkelstein, D.I. (2013) Metallobiology of 1-methyl-4-phenyl-1,2,3,6-tetrahydropyridine neurotoxicity.. Metallomics, 5, 91-109.

Harvey, D.C., Lacan, G., Tanious, S.P., and Melega, W.P. (2000) Recovery from methamphetamine induced long-term nigrostriatal dopaminergic deficits without substantia nigra cell loss.. Brain Res, 871, 259-270.

He, Y., Thong, P.S., Lee, T., Leong, S.K., Shi, C.Y., Wong, P.T., Yuan, S.Y., and Watt, F. (1996) Increased iron in the substantia nigra of 6-OHDA induced parkinsonian rats: a nuclear microscopy study.. Brain Res, 735, 149-153.

Hill, J.M. (1985) Iron concentration reduced in ventral pallidum, globus pallidus, and substantia nigra by GABA-transaminase inhibitor, gamma-vinyl GABA.. Brain Res, 342, 18-25.

HIMWICH, W.A., SULLIVAN, W.T., KELLEY, B., BENARON, H.B., and TUCKER, B.E. (1955) Chemical constituents of human brain.. J Nerv Ment Dis, 122, 441-447.

Hoenig, J.M., and Heisey, D.M. (2001) The Abuse of Power: The Pervasive Fallacy of Power Calculations for Data Analysis. The American Statistician, 55, 19-24.

Hotchkiss, A., and Gibb, J.W. (1980) Blockade of methamphetamine-induced depression of tyrosine hydroxylase by GABA transaminase inhibitors.. Eur J Pharmacol, 66, 201-205.

Imam, S.Z., Crow, J.P., Newport, G.D., Islam, F., Slikker, W., and Ali, S.F. (1999) Methamphetamine generates peroxynitrite and produces dopaminergic neurotoxicity in mice: protective effects of peroxynitrite decomposition catalyst.. Brain Res, 837, 15-21.

Imam, S.Z., el Yazal, J., Newport, G.D., Itzhak, Y., Cadet, J.L., Slikker, W., and Ali, S.F. (2001) Methamphetamine-induced dopaminergic neurotoxicity: role of peroxynitrite and neuroprotective role of antioxidants and peroxynitrite decomposition catalysts.. Ann N Y Acad Sci, 939, 366-380.

Itzhak, Y., and Ali, S.F. (1996) The neuronal nitric oxide synthase inhibitor, 7-nitroindazole, protects against methamphetamine-induced neurotoxicity in vivo.. J Neurochem, 67, 1770-1773.

Itzhak, Y., Gandia, C., Huang, P.L., and Ali, S.F. (1998) Resistance of neuronal nitric oxide synthase-deficient mice to methamphetamine-induced dopaminergic neurotoxicity.. J Pharmacol Exp Ther, 284, 1040-1047.

Jana, S., Sinha, M., Chanda, D., Roy, T., Banerjee, K., Munshi, S., Patro, B.S., and Chakrabarti, S. (2011) Mitochondrial dysfunction mediated by quinone oxidation products of dopamine: Implications in dopamine cytotoxicity and pathogenesis of Parkinson's disease.. Biochim Biophys Acta, 1812, 663-673.

Jayanthi, S., Ladenheim, B., and Cadet, J.L. (1998) Methamphetamine-induced changes in antioxidant enzymes and lipid peroxidation in copper/zinc-superoxide dismutase transgenic mice.. Ann N Y Acad Sci, 844, 92-102.

Jellinger, K., Paulus, W., Grundke-Iqbal, I., Riederer, P., and Youdim, M.B. (1990) Brain iron and ferritin in Parkinson's and Alzheimer's diseases.. J Neural Transm Park Dis Dement Sect, 2, 327-340.

Jenkinson, M., Bannister, P., Brady, M., and Smith, S. (2002) Improved optimization for the robust and accurate linear registration and motion correction of brain images.. Neuroimage, 17, 825-841.

Jenkinson, M., and Smith, S. (2001) A global optimisation method for robust affine registration of brain images.. Med Image Anal, 5, 143-156.

Jiang, H., Qian, Z.-M., and Xie, J.-X. (2003) [Increased DMT1 expression and iron content in MPTP-treated C57BL/6 mice].. Sheng Li Xue Bao, 55, 571-576.

Jiang, H., Song, N., Wang, J., Ren, L.-Y., and Xie, J.-X. (2007) Peripheral iron dextran induced degeneration of dopaminergic neurons in rat substantia nigra.. Neurochem Int, 51, 32-36.

Jiang, H., Song, N., Xu, H., Zhang, S., Wang, J., and Xie, J. (2010) Up-regulation of divalent metal transporter 1 in 6-hydroxydopamine intoxication is IRE/IRP dependent.. Cell Res, 20, 345-356.

Jones, J.A., Hodgkinsonc, P., Barkerc, A.L., and P J Horea (1996) Optimal Sampling Strategies for the Measurement of Spin–Spin Relaxation Times. Journal of Magnetic Resonance, Series B, 113, 25-34.

Kaneko, Y., Kitamoto, T., Tateishi, J., and Yamaguchi, K. (1989) Ferritin immunohistochemistry as a marker for microglia.. Acta Neuropathol, 79, 129-136.

Karoum, F., Chrapusta, S.J., Egan, M.F., and Wyatt, R.J. (1993) Absence of 6-hydroxydopamine in the rat brain after treatment with stimulants and other dopaminergic agents: a mass fragmentographic study.. J Neurochem, 61, 1369-1375.

Kaur, D., Peng, J., Chinta, S.J., Rajagopalan, S., Monte, D.A.D., Cherny, R.A., and Andersen, J.K. (2007) Increased murine neonatal iron intake results in Parkinson-like neurodegeneration with age.. Neurobiol Aging, 28, 907-913.

Kaur, D., Yantiri, F., Rajagopalan, S., Kumar, J., Mo, J.Q., Boonplueang, R., Viswanath, V., Jacobs, R., Yang, L., Beal, M.F., DiMonte, D., Volitaskis, I., Ellerby, L., Cherny, R.A., Bush, A.I., and Andersen, J.K. (2003) Genetic or pharmacological iron chelation prevents MPTP-induced neurotoxicity in vivo: a novel therapy for Parkinson's disease.. Neuron, 37, 899-909.

Khan, F.H., Sen, T., Maiti, A.K., Jana, S., Chatterjee, U., and Chakrabarti, S. (2005) Inhibition of rat brain mitochondrial electron transport chain activity by dopamine oxidation products during extended in vitro incubation: implications for Parkinson's disease.. Biochim Biophys Acta, 1741, 65-74.

Kim, H.C., Jhoo, W.K., Choi, D.Y., Im, D.H., Shin, E.J., Suh, J.H., Floyd, R.A., and Bing, G. (1999) Protection of methamphetamine nigrostriatal toxicity by dietary selenium.. Brain Res, 851, 76-86.

Kitamura, O., Takeichi, T., Wang, E.L., Tokunaga, I., Ishigami, A., and ichi Kubo, S. (2010) Microglial and astrocytic changes in the striatum of methamphetamine abusers.. Leg Med (Tokyo), 12, 57-62.

Kiyatkin, E.A., Brown, P.L., and Sharma, H.S. (2007) Brain edema and breakdown of the blood-brain barrier during methamphetamine intoxication: critical role of brain hyperthermia.. Eur J Neurosci, 26, 1242-1253.

Kiyatkin, E.A., and Sharma, H.S. (2009) Acute methamphetamine intoxication: brain hyperthermia, blood-brain barrier, brain edema, and morphological cell abnormalities.. Int Rev Neurobiol, 88, 65-100.

Klongpanichapak, S., Govitrapong, P., Sharma, S.K., and Ebadi, M. (2006) Attenuation of cocaine and methamphetamine neurotoxicity by coenzyme Q10.. Neurochem Res, 31, 303-311.

Koch, M.L. (1922) CHEMICAL INVESTIGATIONS OF THE CENTRAL NERVOUS SYSTEM UNDER NORMAL AND PATHOLOGIC CONDITIONS: CHEMICAL EXAMINATION OF THE CENTRAL NERVOUS SYSTEM IN TWO CASES OF GENERAL PARALYSIS. Arch NeurPsych. 1922;7(4):488-512. doi:10.1001/archneurpsyc.1922.02190100073003., 7(4), 488-512.

Kousik, S.M., Graves, S.M., Napier, T.C., Zhao, C., and Carvey, P.M. (2011) Methamphetamine-induced vascular changes lead to striatal hypoxia and dopamine reduction.. Neuroreport, 22, 923-928.

Kramer, J.C., Fischman, V.S., and Littlefield, D.C. (1967) Amphetamine abuse. Pattern and effects of high doses taken intravenously.. JAMA, 201, 305-309.

Kuhn, D.M., Francescutti-Verbeem, D.M., and Thomas, D.M. (2006) Dopamine quinones activate microglia and induce a neurotoxic gene expression profile:

relationship to methamphetamine-induced nerve ending damage.. Ann N Y Acad Sci, 1074, 31-41.

Lan, J., and Jiang, D.H. (1997) Desferrioxamine and vitamin E protect against iron and MPTP-induced neurodegeneration in mice.. J Neural Transm, 104, 469-481.

Langkammer, C., Krebs, N., Goessler, W., Scheurer, E., Ebner, F., Yen, K., Fazekas, F., and Ropele, S. (2010) Quantitative MR imaging of brain iron: a postmortem validation study.. Radiology, 257, 455-462.

LaVoie, M.J., Card, J.P., and Hastings, T.G. (2004) Microglial activation precedes dopamine terminal pathology in methamphetamine-induced neurotoxicity.. Exp Neurol, 187, 47-57.

LaVoie, M.J., and Hastings, T.G. (1999) Dopamine quinone formation and protein modification associated with the striatal neurotoxicity of methamphetamine: evidence against a role for extracellular dopamine.. J Neurosci, 19, 1484-1491.

Lazzeri, G., Lenzi, P., Busceti, C.L., Ferrucci, M., Falleni, A., Bruno, V., Paparelli, A., and Fornai, F. (2007) Mechanisms involved in the formation of dopamine-induced intracellular bodies within striatal neurons.. J Neurochem, 101, 1414-1427.

Lazzeri, G., Lenzi, P., Gesi, M., Ferrucci, M., Fulceri, F., Ruggieri, S., Bruno, V., and Fornai, F. (2006) In PC12 cells neurotoxicity induced by methamphetamine is related to proteasome inhibition.. Ann N Y Acad Sci, 1074, 174-177.

Leenders, K.L., Antonini, A., Schwarzbach, R., Smith-Jones, P., Reist, H., Ben-Shachar, D., Youdim, M., and Henn, V. (1994) Blood to brain iron uptake in one rhesus monkey using [Fe-52]-citrate and positron emission tomography (PET): influence of haloperidol.. J Neural Transm Suppl, 43, 123-132.

Levenson, C.W., and Tassabehji, N.M. (2004) Iron and ageing: an introduction to iron regulatory mechanisms.. Ageing Res Rev, 3, 251-263.

ping Li, X., jie Xie, W., Zhang, Z., Kansara, S., Jankovic, J., and dong Le, W. (2012) A mechanistic study of proteasome inhibition-induced iron misregulation in dopamine neuron degeneration.. Neurosignals, 20, 223-236.

Liao, P.C., Kuo, Y.M., Chang, Y.C., Lin, C., Cherng, C.F.G., and Yu, L. (2003) Striatal formation of 6-hydroxydopamine in mice treated with pargyline, pyrogallol and methamphetamine.. J Neural Transm, 110, 487-494.

Lin, M., Chandramani-Shivalingappa, P., Jin, H., Ghosh, A., Anantharam, V., Ali, S., Kanthasamy, A.G., and Kanthasamy, A. (2012) Methamphetamine-induced neurotoxicity linked to ubiquitin-proteasome system dysfunction and autophagy-related changes that can be modulated by protein kinase C delta in dopaminergic neuronal cells.. Neuroscience, 210, 308-332.

Linert, W., Herlinger, E., Jameson, R.F., Kienzl, E., Jellinger, K., and Youdim, M.B. (1996) Dopamine, 6-hydroxydopamine, iron, and dioxygen--their mutual interactions and possible implication in the development of Parkinson's

disease.. Biochim Biophys Acta, 1316, 160-168.

Lotharius, J., Falsig, J., van Beek, J., Payne, S., Dringen, R., Brundin, P., and Leist, M. (2005) Progressive degeneration of human mesencephalic neuron-derived cells triggered by dopamine-dependent oxidative stress is dependent on the mixed-lineage kinase pathway.. J Neurosci, 25, 6329-6342.

Mandel, S., Maor, G., and Youdim, M.B.H. (2004) Iron and alpha-synuclein in the substantia nigra of MPTP-treated mice: effect of neuroprotective drugs R-apomorphine and green tea polyphenol (-)-epigallocatechin-3-gallate.. J Mol Neurosci, 24, 401-416.

Marek, G.J., Vosmer, G., and Seiden, L.S. (1990) Pargyline increases 6-hydroxydopamine levels in the neostriatum of methamphetamine-treated rats.. Pharmacol Biochem Behav, 36, 187-190.

Mark, K.A., Soghomonian, J.-J., and Yamamoto, B.K. (2004) High-dose methamphetamine acutely activates the striatonigral pathway to increase striatal glutamate and mediate long-term dopamine toxicity.. J Neurosci, 24, 11449-11456.

Martin, W.R., Ye, F.Q., and Allen, P.S. (1998) Increasing striatal iron content associated with normal aging.. Mov Disord, 13, 281-286.

Mastroberardino, P.G., Hoffman, E.K., Horowitz, M.P., Betarbet, R., Taylor, G., Cheng, D., Na, H.M., Gutekunst, C.-A., Gearing, M., Trojanowski, J.Q., Anderson, M., Chu, C.T., Peng, J., and Greenamyre, J.T. (2009) A novel transferrin/TfR2-mediated mitochondrial iron transport system is disrupted in Parkinson's disease.. Neurobiol Dis, 34, 417-431.

Matarredona, E.R., Santiago, M., Cano, J., and Machado, A. (1997) Involvement of iron in MPP+ toxicity in substantia nigra: protection by desferrioxamine.. Brain Res, 773, 76-81.

McGowan, S.E., and Henley, S.A. (1988) Iron and ferritin contents and distribution in human alveolar macrophages.. J Lab Clin Med, 111, 611-617.

McGraw, K.O., and Wong, S.P. (1996) Forming inferences about some intraclass correlation coefficients. Psychological Methods, 1, 30-46.

Melega, W.P., Laćan, G., Harvey, D.C., and Way, B.M. (2007) Methamphetamine increases basal ganglia iron to levels observed in aging.. Neuroreport, 18, 1741-1745.

Mills, E., Dong, X.-P., Wang, F., and Xu, H. (2010) Mechanisms of brain iron transport: insight into neurodegeneration and CNS disorders.. Future Med Chem, 2, 51-64.

Mirecki, A., Fitzmaurice, P., Ang, L., Kalasinsky, K.S., Peretti, F.J., Aiken, S.S., Wickham, D.J., Sherwin, A., Nobrega, J.N., Forman, H.J., and Kish, S.J. (2004) Brain antioxidant systems in human methamphetamine users.. J Neurochem, 89, 1396-1408.

Mitsumori, F., Watanabe, H., and Takaya, N. (2009) Estimation of brain iron concentration in vivo using a linear relationship between regional iron and apparent transverse relaxation rate of the tissue water at 4.7T.. Magn Reson

Med, 62, 1326-1330.

Miyazaki, I., Asanuma, M., Diaz-Corrales, F.J., Fukuda, M., Kitaichi, K., Miyoshi, K., and Ogawa, N. (2006) Methamphetamine-induced dopaminergic neurotoxicity is regulated by quinone-formation-related molecules.. FASEB J, 20, 571-573.

Mochizuki, H., Imai, H., Endo, K., Yokomizo, K., Murata, Y., Hattori, N., and Mizuno, Y. (1994) Iron accumulation in the substantia nigra of 1-methyl-4-phenyl-1,2,3,6-tetrahydropyridine (MPTP)-induced hemiparkinsonian monkeys.. Neurosci Lett, 168, 251-253.

Monteiro, H.P., and Winterbourn, C.C. (1989) 6-Hydroxydopamine releases iron from ferritin and promotes ferritin-dependent lipid peroxidation.. Biochem Pharmacol, 38, 4177-4182.

Moos, T., Nielsen, T.R., Skjørringe, T., and Morgan, E.H. (2007) Iron trafficking inside the brain.. J Neurochem, 103, 1730-1740.

Morales, A.M., Lee, B., Hellemann, G., O'Neill, J., and London, E.D. (2012) Gray-matter volume in methamphetamine dependence: cigarette smoking and changes with abstinence from methamphetamine.. Drug Alcohol Depend, 125, 230-238.

Morens, D.M., Grandinetti, A., Reed, D., White, L.R., and Ross, G.W. (1995) Cigarette smoking and protection from Parkinson's disease: false association or etiologic clue?. Neurology, 45, 1041-1051.

Moszczynska, A., Turenne, S., and Kish, S.J. (1998) Rat striatal levels of the antioxidant glutathione are decreased following binge administration of methamphetamine.. Neurosci Lett, 255, 49-52.

Moszczynska, A., and Yamamoto, B.K. (2011) Methamphetamine oxidatively damages parkin and decreases the activity of 26S proteasome in vivo.. J Neurochem, 116, 1005-1017.

Muldoon, L.L., Sàndor, M., Pinkston, K.E., and Neuwelt, E.A. (2005) Imaging, distribution, and toxicity of superparamagnetic iron oxide magnetic resonance nanoparticles in the rat brain and intracerebral tumor.. Neurosurgery, 57, 785-96; discussion 785-96.

Muneer, P.M.A., Alikunju, S., Szlachetka, A.M., Murrin, L.C., and Haorah, J. (2011) Impairment of brain endothelial glucose transporter by methamphetamine causes blood-brain barrier dysfunction.. Mol Neurodegener, 6, 23.

Mussalo-Rauhamaa, H., Leppänen, A., Salmela, S.S., and Pyysalo, H. (1986) Cigarettes as a source of some trace and heavy metals and pesticides in man.. Arch Environ Health, 41, 49-55.

Napolitano, A., Crescenzi, O., Pezzella, A., and Prota, G. (1995) Generation of the neurotoxin 6-hydroxydopamine by peroxidase/H2O2 oxidation of dopamine.. J Med Chem, 38, 917-922.

Nash, J.F., and Yamamoto, B.K. (1992) Methamphetamine neurotoxicity and striatal glutamate release: comparison to 3,4-

methylenedioxymethamphetamine.. Brain Res, 581, 237-243.

National Center for Biotechnology Information ((accessed Feb. 22, 2014).) PubChem Compound Database; CID=1206, http://pubchem.ncbi.nlm.nih.gov/summary/summary.cgi?cid=1206. , , .

Neeb, H., Ermer, V., Stocker, T., and Shah, N.J. (2008) Fast quantitative mapping of absolute water content with full brain coverage.. Neuroimage, 42, 1094-1109.

Nichols, T.E., and Holmes, A.P. (2002) Nonparametric permutation tests for functional neuroimaging: a primer with examples.. Hum Brain Mapp, 15, 1-25.

Northrop, N.A., and Yamamoto, B.K. (2012) Persistent neuroinflammatory effects of serial exposure to stress and methamphetamine on the blood-brain barrier.. J Neuroimmune Pharmacol, 7, 951-968.

Oestreicher, E., Sengstock, G.J., Riederer, P., Olanow, C.W., Dunn, A.J., and Arendash, G.W. (1994) Degeneration of nigrostriatal dopaminergic neurons increases iron within the substantia nigra: a histochemical and neurochemical study.. Brain Res, 660, 8-18.

Ogawa, S., Tank, D.W., Menon, R., Ellermann, J.M., Kim, S.G., Merkle, H., and Ugurbil, K. (1992) Intrinsic signal changes accompanying sensory stimulation: functional brain mapping with magnetic resonance imaging.. Proc Natl Acad Sci U S A, 89, 5951-5955.

Oh, J.S., Lyoo, I.K., Sung, Y.H., Hwang, J., Kim, J., Chung, A., Park, K.S., Kim, S.J., Renshaw, P.F., and Song, I.C. (2005) Shape changes of the corpus callosum in abstinent methamphetamine users.. Neurosci Lett, 384, 76-81.

Pantopoulos, K., Weiss, G., and Hentze, M.W. (1996) Nitric oxide and oxidative stress (H2O2) control mammalian iron metabolism by different pathways.. Mol Cell Biol, 16, 3781-3788.

Park, M., Hennig, B., and Toborek, M. (2012) Methamphetamine alters occludin expression via NADPH oxidase-induced oxidative insult and intact caveolae.. J Cell Mol Med, 16, 362-375.

Park, M.-J., Lee, S.-K., Lim, M.-A., Chung, H.-S., Cho, S.-I., Jang, C.-G., and Lee, S.-M. (2006) Effect of alpha-tocopherol and deferoxamine on methamphetamine-induced neurotoxicity.. Brain Res, 1109, 176-182.

Patenaude, B., Smith, S.M., Kennedy, D.N., and Jenkinson, M. (2011) A Bayesian model of shape and appearance for subcortical brain segmentation.. Neuroimage, 56, 907-922.

Peng, J., Peng, L., Stevenson, F.F., Doctrow, S.R., and Andersen, J.K. (2007) Iron and paraquat as synergistic environmental risk factors in sporadic Parkinson's disease accelerate age-related neurodegeneration.. J Neurosci, 27, 6914-6922.

Penke, L., Hernandéz, M.C.V., Maniega, S.M., Gow, A.J., Murray, C., Starr, J.M., Bastin, M.E., Deary, I.J., and Wardlaw, J.M. (2010) Brain iron deposits are associated with general cognitive ability and cognitive aging.. Neurobiol Aging.

Perry, T.L., Kish, S.J., and Hansen, S. (1979) gamma-Vinyl GABA: effects of

chronic administration on the metabolism of GABA and other amino compounds in rat brain.. J Neurochem, 32, 1641-1645.

Pezzella, A., d'Ischia, M., Napolitano, A., Misuraca, G., and Prota, G. (1997) Iron-mediated generation of the neurotoxin 6-hydroxydopamine quinone by reaction of fatty acid hydroperoxides with dopamine: a possible contributory mechanism for neuronal degeneration in Parkinson's disease.. J Med Chem, 40, 2211-2216.

Pfefferbaum, A., Adalsteinsson, E., Rohlfing, T., and Sullivan, E.V. (2009) MRI estimates of brain iron concentration in normal aging: comparison of field-dependent (FDRI) and phase (SWI) methods.. Neuroimage, 47, 493-500.

Pfefferbaum, A., Adalsteinsson, E., Rohlfing, T., and Sullivan, E.V. (2010) Diffusion tensor imaging of deep gray matter brain structures: effects of age and iron concentration.. Neurobiol Aging, 31, 482-493.

Pinheiro, J., Bates, D., DebRoy, S., Sarkar, D., and the R Core team (2009) nlme: Linear and Nonlinear Mixed Effects Models. , , .

Pujol, J., Junqué, C., Vendrell, P., Grau, J.M., Martí-Vilalta, J.L., Olivé, C., and Gili, J. (1992) Biological significance of iron-related magnetic resonance imaging changes in the brain.. Arch Neurol, 49, 711-717.

Quan, L., Ishikawa, T., Michiue, T., Li, D.-R., Zhao, D., Oritani, S., Zhu, B.-L., and Maeda, H. (2005) Ubiquitin-immunoreactive structures in the midbrain of methamphetamine abusers.. Leg Med (Tokyo), 7, 144-150.

R Development Core Team (2010) R: A Language and Environment for Statistical Computing. http://www.R-project.org.

Ramirez, S.H., Potula, R., Fan, S., Eidem, T., Papugani, A., Reichenbach, N., Dykstra, H., Weksler, B.B., Romero, I.A., Couraud, P.O., and Persidsky, Y. (2009) Methamphetamine disrupts blood-brain barrier function by induction of oxidative stress in brain endothelial cells.. J Cereb Blood Flow Metab, 29, 1933-1945.

Randall, L.O. (1938) Chemical Topography of the Brain. J Biol Chem, 124, 481-488.

Rathnasamy, G., Ling, E.-A., and Kaur, C. (2011) Iron and iron regulatory proteins in amoeboid microglial cells are linked to oligodendrocyte death in hypoxic neonatal rat periventricular white matter through production of proinflammatory cytokines and reactive oxygen/nitrogen species.. J Neurosci, 31, 17982-17995.

Riddle, E.L., Fleckenstein, A.E., and Hanson, G.R. (2006) Mechanisms of methamphetamine-induced dopaminergic neurotoxicity.. AAPS J, 8, E413-E418.

Rooney, W.D., Johnson, G., Li, X., Cohen, E.R., Kim, S.-G., Ugurbil, K., and Springer, C.S. (2007) Magnetic field and tissue dependencies of human brain longitudinal 1H2O relaxation in vivo.. Magn Reson Med, 57, 308-318.

Rusyniak, D.E. (2011) Neurologic manifestations of chronic methamphetamine abuse.. Neurol Clin, 29, 641-655.

Ryan, R.E., Ross, S.A., Drago, J., and Loiacono, R.E. (2001) Dose-related neuroprotective effects of chronic nicotine in 6-hydroxydopamine treated rats, and loss of neuroprotection in alpha4 nicotinic receptor subunit knockout mice.. Br J Pharmacol, 132, 1650-1656.

Salazar, J., Mena, N., Hunot, S., Prigent, A., Alvarez-Fischer, D., Arredondo, M., Duyckaerts, C., Sazdovitch, V., Zhao, L., Garrick, L.M., Nuñez, M.T., Garrick, M.D., Raisman-Vozari, R., and Hirsch, E.C. (2008) Divalent metal transporter 1 (DMT1) contributes to neurodegeneration in animal models of Parkinson's disease.. Proc Natl Acad Sci U S A, 105, 18578-18583.

Sastry, S., and Arendash, G.W. (1995) Time-dependent changes in iron levels and associated neuronal loss within the substantia nigra following lesions within the neostriatum/globus pallidus complex.. Neuroscience, 67, 649-666.

Schenck, J.F. (2003) Magnetic resonance imaging of brain iron.. J Neurol Sci, 207, 99-102.

Schenck, J.F., and Zimmerman, E.A. (2004) High-field magnetic resonance imaging of brain iron: birth of a biomarker?. NMR Biomed, 17, 433-445.

Schenker, C., Meier, D., Wichmann, W., Boesiger, P., and Valavanis, A. (1993) Age distribution and iron dependency of the T2 relaxation time in the globus pallidus and putamen.. Neuroradiology, 35, 119-124.

Schuirmann, D.J. (1987) A comparison of the two one-sided tests procedure and the power approach for assessing the equivalence of average bioavailability.. J Pharmacokinet Biopharm, 15, 657-680.

Segal, D.S., Kuczenski, R., O'Neil, M.L., Melega, W.P., and Cho, A.K. (2003) Escalating dose methamphetamine pretreatment alters the behavioral and neurochemical profiles associated with exposure to a high-dose methamphetamine binge.. Neuropsychopharmacology, 28, 1730-1740.

Seiden, L.S. (1985) Methamphetamine: toxicity to dopaminergic neurons.. NIDA Res Monogr, 62, 100-116.

Seiden, L.S., and Vosmer, G. (1984) Formation of 6-hydroxydopamine in caudate nucleus of the rat brain after a single large dose of methylamphetamine.. Pharmacol Biochem Behav, 21, 29-31.

Sekine, Y., Ouchi, Y., Sugihara, G., Takei, N., Yoshikawa, E., Nakamura, K., Iwata, Y., Tsuchiya, K.J., Suda, S., Suzuki, K., Kawai, M., Takebayashi, K., Yamamoto, S., Matsuzaki, H., Ueki, T., Mori, N., Gold, M.S., and Cadet, J.L. (2008) Methamphetamine causes microglial activation in the brains of human abusers.. J Neurosci, 28, 5756-5761.

Sengstock, G.J., Olanow, C.W., Menzies, R.A., Dunn, A.J., and Arendash, G.W. (1993) Infusion of iron into the rat substantia nigra: nigral pathology and dose-dependent loss of striatal dopaminergic markers.. J Neurosci Res, 35, 67-82.

Shah, A., Kumar, S., Simon, S.D., Singh, D.P., and Kumar, A. (2013) HIV gp120- and methamphetamine-mediated oxidative stress induces astrocyte apoptosis via cytochrome P450 2E1.. Cell Death Dis, 4, e850.

Sharma, H.S., and Kiyatkin, E.A. (2009) Rapid morphological brain abnormalities

during acute methamphetamine intoxication in the rat: an experimental study using light and electron microscopy.. J Chem Neuroanat, 37, 18-32.

Shoham, S., Wertman, E., and Ebstein, R.P. (1992) Iron accumulation in the rat basal ganglia after excitatory amino acid injections--dissociation from neuronal loss.. Exp Neurol, 118, 227-241.

Sikk, K., Haldre, S., Aquilonius, S.-M., Asser, A., Paris, M., Roose, Ä., Petterson, J., Eriksson, S.-L., Bergquist, J., and Taba, P. (2013) Manganese-induced parkinsonism in methcathinone abusers: bio-markers of exposure and follow-up.. Eur J Neurol, 20, 915-920.

Sikk, K., Taba, P., Haldre, S., Bergquist, J., Nyholm, D., Zjablov, G., Asser, T., and Aquilonius, S.-M. (2007) Irreversible motor impairment in young addicts--ephedrone, manganism or both?. Acta Neurol Scand, 115, 385-389.

Simon, S.L., Domier, C., Carnell, J., Brethen, P., Rawson, R., and Ling, W. (2000) Cognitive impairment in individuals currently using methamphetamine.. Am J Addict, 9, 222-231.

Smith, S., and Brady, J. (1997) SUSAN - a new approach to low level image processing.. International Journal of Computer Vision, 23 (1), 45-78.

Smith, S.M. (2002) Fast robust automated brain extraction.. Hum Brain Mapp, 17, 143-155.

Smith, S.M., Jenkinson, M., Woolrich, M.W., Beckmann, C.F., Behrens, T.E.J., Johansen-Berg, H., Bannister, P.R., Luca, M.D., Drobnjak, I., Flitney, D.E., Niazy, R.K., Saunders, J., Vickers, J., Zhang, Y., Stefano, N.D., Brady, J.M., and Matthews, P.M. (2004) Advances in functional and structural MR image analysis and implementation as FSL.. Neuroimage, 23 Suppl 1, S208-S219.

Song, N., Jiang, H., Wang, J., and Xie, J.-X. (2007) Divalent metal transporter 1 up-regulation is involved in the 6-hydroxydopamine-induced ferrous iron influx.. J Neurosci Res, 85, 3118-3126.

Sonsalla, P.K., Nicklas, W.J., and Heikkila, R.E. (1989) Role for excitatory amino acids in methamphetamine-induced nigrostriatal dopaminergic toxicity.. Science, 243, 398-400.

Steen, R.G., Ogg, R.J., Reddick, W.E., and Kingsley, P.B. (1997) Age-related changes in the pediatric brain: quantitative MR evidence of maturational changes during adolescence.. AJNR Am J Neuroradiol, 18, 819-828.

Stepens, A., Logina, I., Liguts, V., Aldins, P., Eksteina, I., Platkājis, A., Mārtinsone, I., Tērauds, E., Rozentāle, B., and Donaghy, M. (2008) A Parkinsonian syndrome in methcathinone users and the role of manganese.. N Engl J Med, 358, 1009-1017.

Stephans, S.E., and Yamamoto, B.K. (1994) Methamphetamine-induced neurotoxicity: roles for glutamate and dopamine efflux.. Synapse, 17, 203-209.

Substance Abuse, and Mental Health Services Administration (2012) Results from the 2012 National Survey on Drug Use and Health: National Findings. Office of Applied Studies: Rockville, MD., http://www.samhsa.gov/data/NSDUH/2012SummNatFindDetTables/2012, .

Sullivan, E.V., Adalsteinsson, E., Rohlfing, T., and Pfefferbaum, A. (2009) Relevance of Iron Deposition in Deep Gray Matter Brain Structures to Cognitive and Motor Performance in Healthy Elderly Men and Women: Exploratory Findings.. Brain Imaging Behav, 3, 167-175.

Sulzer, D., Chen, T.K., Lau, Y.Y., Kristensen, H., Rayport, S., and Ewing, A. (1995) Amphetamine redistributes dopamine from synaptic vesicles to the cytosol and promotes reverse transport.. J Neurosci, 15, 4102-4108.

Sulzer, D., Sonders, M.S., Poulsen, N.W., and Galli, A. (2005) Mechanisms of neurotransmitter release by amphetamines: a review.. Prog Neurobiol, 75, 406-433.

Sulzer, D., and Zecca, L. (2000) Intraneuronal dopamine-quinone synthesis: a review.. Neurotox Res, 1, 181-195.

Sun, L., Li, H.-M., Seufferheld, M.J., Walters, K.R., Margam, V.M., Jannasch, A., Diaz, N., Riley, C.P., Sun, W., Li, Y.-F., Muir, W.M., Xie, J., Wu, J., Zhang, F., Chen, J.Y., Barker, E.L., Adamec, J., and Pittendrigh, B.R. (2011) Systems-scale analysis reveals pathways involved in cellular response to methamphetamine.. PLoS One, 6, e18215.

Suriyaprom, K., Tanateerabunjong, R., Tungtrongchitr, A., and Tungtrongchitr, R. (2011) Alterations in malondialdehyde levels and laboratory parameters among methamphetamine abusers.. J Med Assoc Thai, 94, 1533-1539.

Tarohda, T., Ishida, Y., Kawai, K., Yamamoto, M., and Amano, R. (2005) Regional distributions of manganese, iron, copper, and zinc in the brains of 6-hydroxydopamine-induced parkinsonian rats.. Anal Bioanal Chem, 383, 224-234.

Temlett, J.A., Landsberg, J.P., Watt, F., and Grime, G.W. (1994) Increased iron in the substantia nigra compacta of the MPTP-lesioned hemiparkinsonian African green monkey: evidence from proton microprobe elemental microanalysis.. J Neurochem, 62, 134-146.

Thomas, D.M., Dowgiert, J., Geddes, T.J., Francescutti-Verbeem, D., Liu, X., and Kuhn, D.M. (2004a) Microglial activation is a pharmacologically specific marker for the neurotoxic amphetamines.. Neurosci Lett, 367, 349-354.

Thomas, D.M., and Kuhn, D.M. (2005a) MK-801 and dextromethorphan block microglial activation and protect against methamphetamine-induced neurotoxicity.. Brain Res, 1050, 190-198.

Thomas, D.M., and Kuhn, D.M. (2005b) Attenuated microglial activation mediates tolerance to the neurotoxic effects of methamphetamine.. J Neurochem, 92, 790-797.

Thomas, D.M., Walker, P.D., Benjamins, J.A., Geddes, T.J., and Kuhn, D.M. (2004b) Methamphetamine neurotoxicity in dopamine nerve endings of the striatum is associated with microglial activation.. J Pharmacol Exp Ther, 311, 1-7.

Thompson, P.M., Hayashi, K.M., Simon, S.L., Geaga, J.A., Hong, M.S., Sui, Y., Lee, J.Y., Toga, A.W., Ling, W., and London, E.D. (2004) Structural

abnormalities in the brains of human subjects who use methamphetamine.. J Neurosci, 24, 6028-6036.

Tjoa, C.W., Benedict, R.H.B., Weinstock-Guttman, B., Fabiano, A.J., and Bakshi, R. (2005) MRI T2 hypointensity of the dentate nucleus is related to ambulatory impairment in multiple sclerosis.. J Neurol Sci, 234, 17-24.

Toborek, M., Seelbach, M.J., Rashid, C.S., András, I.E., Chen, L., Park, M., and Esser, K.A. (2013) Voluntary exercise protects against methamphetamine-induced oxidative stress in brain microvasculature and disruption of the blood--brain barrier.. Mol Neurodegener, 8, 22.

Todd, G., Noyes, C., Flavel, S.C., Vedova, C.B.D., Spyropoulos, P., Chatterton, B., Berg, D., and White, J.M. (2013) Illicit stimulant use is associated with abnormal substantia nigra morphology in humans.. PLoS One, 8, e56438.

Valvassori, S.S., Petronilho, F.C., Réus, G.Z., Steckert, A.V., Oliveira, V.B.M., Boeck, C.R., Kapczinski, F., Dal-Pizzol, F., and Quevedo, J. (2008) Effect of N-acetylcysteine and/or deferoxamine on oxidative stress and hyperactivity in an animal model of mania.. Prog Neuropsychopharmacol Biol Psychiatry, 32, 1064-1068.

Vito, M.J.D., and Wagner, G.C. (1989) Methamphetamine-induced neuronal damage: a possible role for free radicals.. Neuropharmacology, 28, 1145-1150.

Volkow, N.D., Chang, L., Wang, G.J., Fowler, J.S., Franceschi, D., Sedler, M.J., Gatley, S.J., Hitzemann, R., Ding, Y.S., Wong, C., and Logan, J. (2001) Higher cortical and lower subcortical metabolism in detoxified methamphetamine abusers.. Am J Psychiatry, 158, 383-389.

Volz, S., Nöth, U., and Deichmann, R. (2012) Correction of systematic errors in quantitative proton density mapping.. Magn Reson Med, 68, 74-85.

Vymazal, J., Brooks, R.A., Baumgarner, C., Tran, V., Katz, D., Bulte, J.W., Bauminger, R., and Chiro, G.D. (1996) The relation between brain iron and NMR relaxation times: an in vitro study.. Magn Reson Med, 35, 56-61.

Vymazal, J., Righini, A., Brooks, R.A., Canesi, M., Mariani, C., Leonardi, M., and Pezzoli, G. (1999) T1 and T2 in the brain of healthy subjects, patients with Parkinson disease, and patients with multiple system atrophy: relation to iron content.. Radiology, 211, 489-495.

Wagner, G.C., Carelli, R.M., and Jarvis, M.F. (1985) Pretreatment with ascorbic acid attenuates the neurotoxic effects of methamphetamine in rats.. Res Commun Chem Pathol Pharmacol, 47, 221-228.

Wang, G.-J., Volkow, N.D., Chang, L., Miller, E., Sedler, M., Hitzemann, R., Zhu, W., Logan, J., Ma, Y., and Fowler, J.S. (2004) Partial recovery of brain metabolism in methamphetamine abusers after protracted abstinence.. Am J Psychiatry, 161, 242-248.

Wang, N., Guan, P., Li, F., Fu, Y., Duan, X., and Chang, Y. (2010) Sodium glutamate and gamma-aminobutyric acid affect iron metabolism in the rat caudate putamen. Neural Regeneration Research, 5, 1644-1649.

Wansapura, J.P., Holland, S.K., Dunn, R.S., and Ball, W.S. (1999) NMR

relaxation times in the human brain at 3.0 tesla.. J Magn Reson Imaging, 9, 531-538.

Weinberger, A.H., and Sofuoglu, M. (2009) The impact of cigarette smoking on stimulant addiction.. Am J Drug Alcohol Abuse, 35, 12-17.

Weinreb, O., Mandel, S., Youdim, M.B.H., and Amit, T. (2013) Targeting dysregulation of brain iron homeostasis in Parkinson's disease by iron chelators.. Free Radic Biol Med, 62, 52-64.

Weinstein, J.S., Varallyay, C.G., Dosa, E., Gahramanov, S., Hamilton, B., Rooney, W.D., Muldoon, L.L., and Neuwelt, E.A. (2010) Superparamagnetic iron oxide nanoparticles: diagnostic magnetic resonance imaging and potential therapeutic applications in neurooncology and central nervous system inflammatory pathologies, a review.. J Cereb Blood Flow Metab, 30, 15-35.

Weiss, G., Goossen, B., Doppler, W., Fuchs, D., Pantopoulos, K., Werner-Felmayer, G., Wachter, H., and Hentze, M.W. (1993) Translational regulation via iron-responsive elements by the nitric oxide/NO-synthase pathway.. EMBO J, 12, 3651-3657.

Whittall, K.P., MacKay, A.L., Graeb, D.A., Nugent, R.A., Li, D.K., and Paty, D.W. (1997) In vivo measurement of T2 distributions and water contents in normal human brain.. Magn Reson Med, 37, 34-43.

Wilson, J.M., Kalasinsky, K.S., Levey, A.I., Bergeron, C., Reiber, G., Anthony, R.M., Schmunk, G.A., Shannak, K., Haycock, J.W., and Kish, S.J. (1996) Striatal dopamine nerve terminal markers in human, chronic methamphetamine users.. Nat Med, 2, 699-703.

Woolverton, W.L., Cervo, L., and Johanson, C.E. (1984) Effects of repeated methamphetamine administration on methamphetamine self-administration in rhesus monkeys.. Pharmacol Biochem Behav, 21, 737-741.

Woolverton, W.L., Ricaurte, G.A., Forno, L.S., and Seiden, L.S. (1989) Long-term effects of chronic methamphetamine administration in rhesus monkeys.. Brain Res, 486, 73-78.

Wrona, M.Z., Yang, Z., Zhang, F., and Dryhurst, G. (1997) Potential new insights into the molecular mechanisms of methamphetamine-induced neurodegeneration.. NIDA Res Monogr, 173, 146-174.

Xiong, P., Chen, X., Guo, C., Zhang, N., and Ma, B. (2012) Baicalin and deferoxamine alleviate iron accumulation in different brain regions of Parkinson's disease rats. Neural Regeneration Research, 7, 2092-2098.

Xu, X., Wang, Q., and Zhang, M. (2008) Age, gender, and hemispheric differences in iron deposition in the human brain: an in vivo MRI study.. Neuroimage, 40, 35-42.

Yamamoto, B.K., and Raudensky, J. (2008) The role of oxidative stress, metabolic compromise, and inflammation in neuronal injury produced by amphetamine-related drugs of abuse.. J Neuroimmune Pharmacol, 3, 203-217.

Yamamoto, B.K., and Zhu, W. (1998) The effects of methamphetamine on the

production of free radicals and oxidative stress.. J Pharmacol Exp Ther, 287, 107-114.

Yoshida, T., Tanaka, M., Sotomatsu, A., and Hirai, S. (1995) Activated microglia cause superoxide-mediated release of iron from ferritin.. Neurosci Lett, 190, 21-24.

Yoshida, T., Tanaka, M., Sotomatsu, A., Hirai, S., and Okamoto, K. (1998) Activated microglia cause iron-dependent lipid peroxidation in the presence of ferritin.. Neuroreport, 9, 1929-1933.

Youdim, M.B.H., Stephenson, G., and Shachar, D.B. (2004) Ironing iron out in Parkinson's disease and other neurodegenerative diseases with iron chelators: a lesson from 6-hydroxydopamine and iron chelators, desferal and VK-28.. Ann N Y Acad Sci, 1012, 306-325.

Zecca, L., Berg, D., Arzberger, T., Ruprecht, P., Rausch, W.D., Musicco, M., Tampellini, D., Riederer, P., Gerlach, M., and Becker, G. (2005) In vivo detection of iron and neuromelanin by transcranial sonography: a new approach for early detection of substantia nigra damage.. Mov Disord, 20, 1278-1285.

Zecca, L., Youdim, M.B.H., Riederer, P., Connor, J.R., and Crichton, R.R. (2004) Iron, brain ageing and neurodegenerative disorders.. Nat Rev Neurosci, 5, 863-873.

Zhang, X., Xie, W., Qu, S., Pan, T., Wang, X., and Le, W. (2005) Neuroprotection by iron chelator against proteasome inhibitor-induced nigral degeneration.. Biochem Biophys Res Commun, 333, 544-549.

Zhang, Z., Andersen, A., Smith, C., Grondin, R., Gerhardt, G., and Gash, D. (2000) Motor slowing and parkinsonian signs in aging rhesus monkeys mirror human aging.. J Gerontol A Biol Sci Med Sci, 55, B473-B480.

Zhu, W., Xie, W., Pan, T., Xu, P., Fridkin, M., Zheng, H., Jankovic, J., Youdim, M.B.H., and Le, W. (2007) Prevention and restoration of lactacystin-induced nigrostriatal dopamine neuron degeneration by novel brain-permeable iron chelators.. FASEB J, 21, 3835-3844.

Zweben, J.E., Cohen, J.B., Christian, D., Galloway, G.P., Salinardi, M., Parent, D., Iguchi, M., and Project, M.T. (2004) Psychiatric symptoms in methamphetamine users.. Am J Addict, 13, 181-190.

Appendix 1

Increased striatal iron accumulation in human methamphetamine users

Y. A. Berlow, D. L. Lahna, D. L. Schwartz, A. D. Mitchell, A. A. Stevens, W. D. Rooney, and W. F. Hoffman

Introduction: Recent studies in animal and *in vitro* models have provided preliminary evidence of the role of iron as a biomarker and potential source of methamphetamine (MA) induced toxicity.[1, 2, 3] However, the effects of MA administration on iron accumulation have not yet been demonstrated in human MA users. Magnetic resonance imaging (MRI) provides noninvasive methods to indirectly measure iron accumulation *in vivo* in human subjects. Iron is paramagnetic, and its presence shortens the transverse relaxation (T_2) time constant of nearby water protons causing decreased signal intensity on T_2 weighted images. The purpose of this study was to investigate regional cerebral T_2-weighted MRI signal intensity (SI) differences between healthy controls and subjects with a history of MA abuse. It was predicted that MA users will have increased iron concentrations as measured by decreased T_2-weighted SI values within basal ganglia structures compared to aged match healthy controls.

Methods: Subject data sets were acquired retrospectively from a previous study investigating the effects of MA on measures of white matter integrity, using diffusion tensor imaging. This study included 37 individuals with a history of MA

abuse and 33 healthy control subjects. All MA subjects met DSM-IV criteria for MA dependence based on interview and chart review of available records. Control subjects' drug use history was assessed by interview. Control subjects had never used substances aside from alcohol, tobacco and marijuana and were excluded if they had ever met criteria for abuse or dependence on alcohol or marijuana. All MRI data were acquired on a Siemens 3T TIM Trio and included a high-resolution, T_1-weighted, whole-brain 3D MPRAGE sequence (FOV = 20x20x16 cm, matrix 256x256x144, TE=4ms, TI=900ms, TR=2300ms, flip angle=8º) and an axial 2D double spin echo EPI T_2 weighted image (FOV=256x256 mm, matrix 128x128, 72 2mm thick slices, 2mm gap width, TR 9100ms, TE = 90ms). Bilateral, subcortical regions of interest (ROI), including caudate, putamen, and pallidum, were identified on the MPRAGE images using FMRIB's Integrated Registration and Segmentation Tool.[4] These identified ROI's were transformed to the individual's T_2-weighted image space and mean SI values within each ROI were obtained (Fig. 1). Mixed effect linear models were constructed to assess the effects MA use on T_2-weighted SI
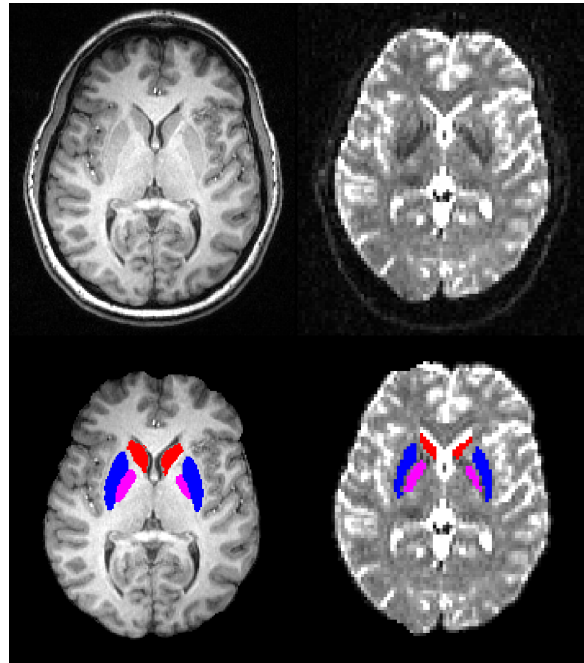
Figure 1: Subcortical region of interest (ROI) identification.

139

in each ROI. Iron content estimates were calculated for control subjects using published regression equations from postmortem data based on age and subcortical region.[5] Voxel wise analysis of the T_2-weighted images was carried out using tools from FSL[6] and AFNI[7] as an unbiased confirmation of the ROI approach.

Results and Discussion: Individuals with a history of MA dependence had reduced T_2 SI values in the caudate ($F(1,67)=6.04$, $p=0.0166$) and putamen $F(1,67)=8.42$, $p=0.005$), but not in the pallidum ($F(1,67)=1.01$, $p=0.31$)(Fig. 2). These findings were further confirmed with a voxel wise analysis approach which identified reduced T_2-weighted SI measurements in the right striatum of MA users (Fig 3). The iron content estimates obtained by applying the regression formulas based on postmortem data of iron content by region and age[5] significantly correlated with the measured T_2-weighted SI values in control subjects ($R^2=0.88$, $p<0.0001$). T_2-weighted SI measurements also demonstrated a strong effect of age in the caudate ($F(1,67)=22.08$, $p<0.0001$) and putamen ($F(1,67)=17.22$, $p<0.0001$),
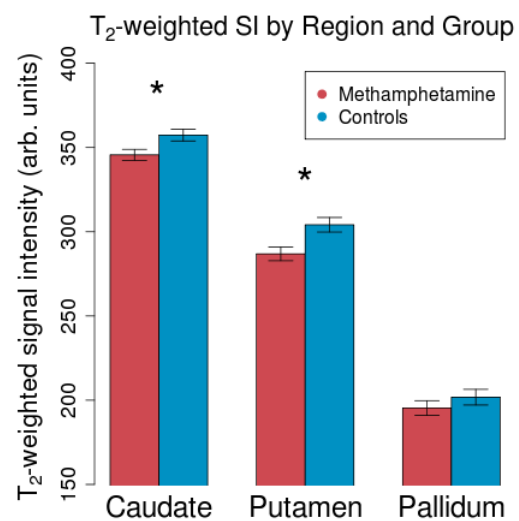
Figure 2: Region of interest analysis demonstrating the main effects of methamphetamine use on T_2-weighted signal intensity measurements in the caudate and putamen. * = $p<0.05$ after Bonferroni corrections.

140
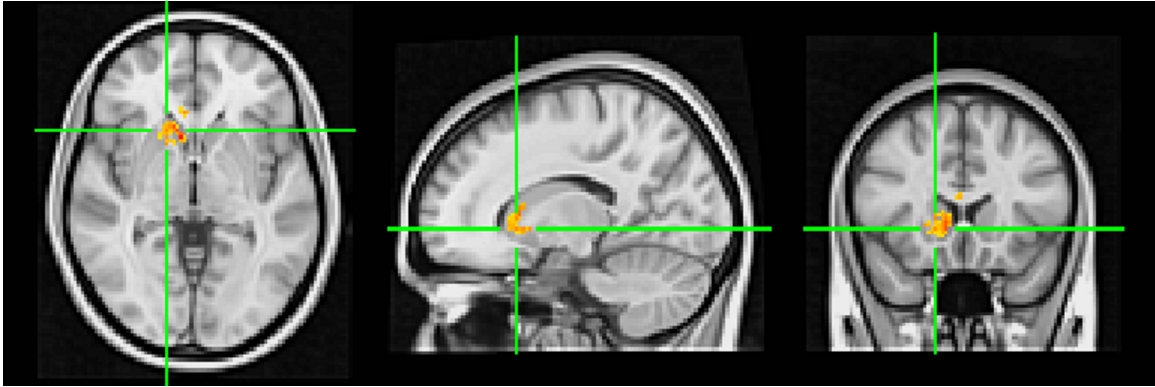
Figure 3: Voxel wise analysis demonstrating striatal areas of lower T2-weighted signal intensity in methamphetamine users.

consistent with the established age-related increase in iron seen in these subcortical areas.[5, 8, 9] Taken together, these results provide some of the first evidence that suggests increased iron accumulation within the striatum in human MA users.

References: 1: Melega, Laćan, Harvey, & Way. Neuroreport. 2007; 18:1741-1745. 2: Yamamoto, & Zhu. J Pharmacol Exp Ther. 1998; 287:107-114. 3: Lotharius, Falsig, van Beek, Payne, Dringen, Brundin, & Leist. J Neurosci. 2005; 25:6329-6342. 4: Patenaude. D. Phil. Thesis. University of Oxford. 2007. 5: Hallgren, & Sourander. J Neurochem. 1958; 3:41-51. 6: Andersson, Jenkinson, & Smith. www.fmrib.ox.ac.uk/analysis/ techrep/, 2007. 7: Ward. http://afni.nimh.nih.gov/pub/dist/ doc/manual/3dRegAnam.pdf, 2006. 8: Bartzokis, Tishler, Lu, Villablanca, Altshuler, Carter, Huang, Edwards, & Mintz. Neurobiol Aging. 2007; 28:414-423. 9: Pfefferbaum, Adalsteinsson, Rohlfing, & Sullivan. Neuroimage. 2009; 47:493-500.

Appendix 2

Brain Iron Levels Across the Japanese Macaque Lifespan

Yosef A. Berlow, Steve Kohama, James Pollaro, Manoj Sammi, and William

Rooney

Introduction: Iron (Fe) is an essential element for almost all living organisms. In mammals, Fe is crucial for oxygen transport, electron transport reactions associated with oxidative metabolism, DNA replication and repair, and many other biochemical functions (1-3). In the human brain non-heme iron content varies regionally, with the highest concentration in the globus pallidus (21 mg Fe/100 g tissue; 5.2 mM Fe), and relatively low concentration in the cortical gray matter (3 mg Fe/100 g tissue; 0.7 mM Fe) (4). Iron concentration in the human brain parenchyma increases non-linearly with age (4). Ferritin is the primary iron storage protein in the brain, and can accommodate up to 4500 iron (Fe^{3+}) atoms (5). Since free iron can catalyze oxidative tissue injury, elaborate iron handling and storage mechanisms exist to mitigate such effects. Increased brain iron has been implicated in many neurodegenerative disease states including Alzheimer's disease, Parkinson's disease, multiple sclerosis and others (1-3). For some conditions, such as NBIA, a rare autosomal recessive neurodegenerative disease (1,2), massively increased brain iron deposition is thought to be a primary disease pathology. The purpose of this study was to investigate high-field

MRI relaxometry for non-invasive brain iron measurement across the Japanese macaque lifespan and compare to similar measurements in healthy humans.

Methods: The ONPRC Japanese macaque (JM) colony is housed year-round in an outdoor corral with a current total population of ~300. This study included 88 JM (48 female; 39 males, 1 hermaphrodite; age range 1-38 y) and 43 healthy human control subjects (24 females, 19 males; aged 22-61 y) scanned under IACUC and IRB approved protocols. All MRI data were acquired on a whole-body Siemens 3 Tesla (T) MRI instrument (Erlangen, Germany) using a using a 15 cm quadrature radiofrequency (RF) coil for the JM and a 24 cm 12-channel receive only RF coil for human brain.Animals were initially sedated with Telazol, intubated and maintained on 1% isolfurane in 100% O_2 and were continuously monitored by pulse oximetry, respiration, and end tidal CO_2 levels during the study. After shim adjustment and spatial localizers the following sequences were acquired for all JMs: 1) an axial 2D T_2-weighted TSE sequence (TR: 9000 ms; TE: 92 ms; ETL 9, FOV 180 mm x 160 mm, matrix: 320x240, ST 1.0 mm), and 2) an axial 2D PD TSE sequence (TR: 9000 ms, TE: 13 ms, ETL 9, FOV 180 mm x 160 mm matrix: 320x240, ST 1.0 mm).Sequences acquired for human data included an axial 2D T_2-weighted TSE sequence (TR: 12000 ms; TE: 90 ms; ETL 9, FOV 192 mm x 256mm, matrix: 240x320, ST 2.0 mm), and 2) an axial 2D PD TSE sequence (TR: 12000 ms, TE: 13 ms, ETL 9, FOV 192 mm x 256mm, matrix: 240x320, ST 2.0 mm).T_2 and the corresponding R_2 maps were calculated at each voxel using a mono-exponential decay function. Bilateral regions of

interest (ROI) were placed in the caudate, putamen and pallidum using the base PD image as a reference. Brain iron content estimates were calculated using published regression equations from postmortem data based on age and subcortical region (4,6). The effects of age on R_2 were modeled with exponential functions based on the work of Hallgren and Sourander (4).

Results and Discussion: R_2 values significantly correlated with calculated estimates of brain iron content (Fe_{est}; mg/100g) in both JM ($R_2 = 0.46*Fe_{est} + 9.0$; $R^2 = 0.72$, $p < 0.0001$) and humans ($R_2 = 0.44*Fe_{est} + 8.0$; $R^2 = 0.83$, $p < 0.0001$). The models of R_2 changes with age demonstrate that in the JM, R_2 values increase rapidly during the first two decades of life and then begin to plateau at high levels. The time rate constants of the increasing R_2 values in the JM are very similar to the patterns of R_2 increase and iron accumulation seen in humans. However, the maximum R_2 values seen in the JM are much greater than the values seen in humans. This is especially apparent in the pallidum where R_2 values in the JM almost double those seen in humans. These findings suggest that JM continue to accumulate brain iron throughout much of their adulthood
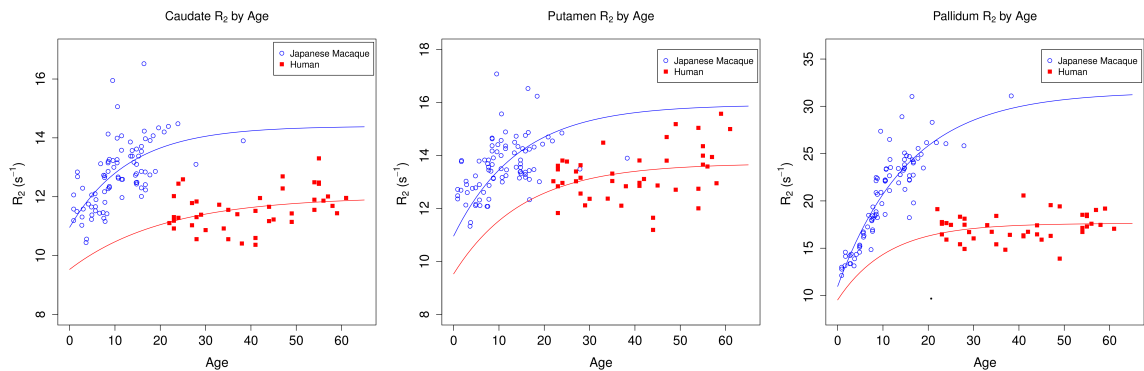
and attain brain iron concentrations that are much greater than the concentrations seen in human brains.

References: 1. Hayflick SJ. Semin Pediatr Neurol. 2006 13:182-185. **2.** Gregory A, Hayflick SJ. Folia Neuropathol. 2005;43:286-296. **3.** Pinero DJ, Connor JR. Neuroscientist 2000: 6:435-453. **4.** Hallgren B, and Sourander P. J. Neurochem. 1958 3:41-51. **5.** Bartzokis G, Tishler TA, Lu PH, Villablanca P, Altshuler LL, Carter M, Huang D, Edwards N, Mintz J. Neurobiol Aging. 2007 28:414-423. **6.** Hardy, Gash, Yokel, Andersen, Ai,& Zhang. J Magn Reson Imaging. 2005; 21:118-127

Appendix 3

Brain Iron Content and Smoking History in Healthy Older Individuals

Yosef A. Berlow, David L. Lahna, Daniel L. Schwartz, Randall L. Woltjer, Robin

Guariglia, Lisa C. Silbert, Jeffrey A Kaye, William D. Rooney

Proceedings of the International Society for Magnetic Resonance in Medicine,

2014; 22: 4677

Introduction: While cigarette smoking has been demonstrated to increase iron accumulation in the lungs[1,2] and significantly alter systemic iron metabolism,[2,3] little is known about the relationship between smoking and brain iron accumulation. Magnetic Resonance Imaging (MRI) provides an in vivo method to assess brain iron content indirectly by measuring the water proton transverse relaxation rate constant (R_2), which varies linearly with iron concentration. This study utilized R_2 measurements from the MRI scans of 81 healthy elderly individuals to investigate the relationship between smoking history and MRI measures of iron content within basal ganglia structures.

Methods: MRI scans and de-identified subject data were acquired through the Oregon Brain Aging Study (OBAS). Eighty-nine healthy subjects, independently living and cognitively intact, aged 62-102 y, who had comparable MRI scans and information about smoking history were identified. Of these, 51 subjects (18 men, 33 women) reported smoking fewer than 100 cigarettes in their lifetime and were classified as nonsmokers. Thirty two subjects (16 men and 16 women) were identified as having a positive smoking history, including two individuals who

146

continued to smoke and 30 exsmokers that had at least a 5 year period of regular smoking in their lifetime. These subjects were dichotomized into "long-term smokers" (n=16) and "short-term smokers" (n=16) using a median split of their years smoking. Six subjects who either smoked primarily cigars or pipes or smoked more than 100 cigarettes but for fewer than 5 years were excluded from the analysis. A Fast Spin Echo Double Echo sequence (FOV=24x24x16 cm, matrix=256x256x40,TE=32, 80ms, TR=3s) was used to generate voxelwise R_2 maps using a mono-exponential decay function. Square regions of interest (14 mm^2) were placed bilaterally in the caudate, putamen and pallidum (see **Figure 1**). The effect of smoking history on R_2 values was analyzed with analysis of variance, followed by Tukey's HSD to compare individual groups. Additional linear models adjusting for sex and age were also analyzed. Pack year estimates were determined in 29 of the subjects with positive smoking history and additional correlations were run between ranked pack year estimates and R_2 values.

Results: The groups did not differ in age ($F_{(2,80)}=0.47$, $p=0.63$) or gender distribution ($\chi^2(1)=1.76$, $p=0.42$). Significant main effects of smoking history were found bilaterally in the caudate (Left: $F_{(2,80)}=4.54$, $p=0.014$; Right: $F_{(2,80)}=6.24$, $p=0.0030$) and putamen (Left: $F_{(2,80)}=6.85$, $p=0.0018$; Right: $F_{(2,80)}=8.58$, $p=0.00042$), but not in the pallidum. Post hoc analyses revealed that "long-term smokers" (>23 years of smoking) had higher R_2 values than both "short-term smokers" (5-22 years) and nonsmokers in these regions (**Figure 2**). Linear

models adjusting for age and gender resulted in similar main effects of smoking status for the caudate and putamen, with "long-term smokers" displaying higher R_2 values compared to the other groups. Small age effects were seen in left pallidum $(F(1,79)=5.14, p=0.026)$ and left caudate $(F(1,79=4.73, p=0.033)$ with increasing age associated with decreasing R_2 values. No gender effects were detected. Positive correlations were found between ranked pack years and R_2 values in the right and left caudate $(r(27)=0.45, p=0.015; r(27=0.48, p=0.009)$, respectively). Similar positive correlations were seen in the right
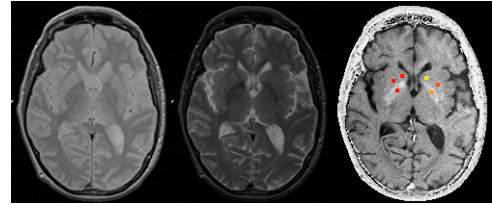
Figure 1: R_2 maps and region of interest placement. Examples of the proton density (left) and T_2 weighted (middle) images that were used to generate R_2 maps (right). Regions of interest were placed bilaterally in the caudate, putamen and pallidum.
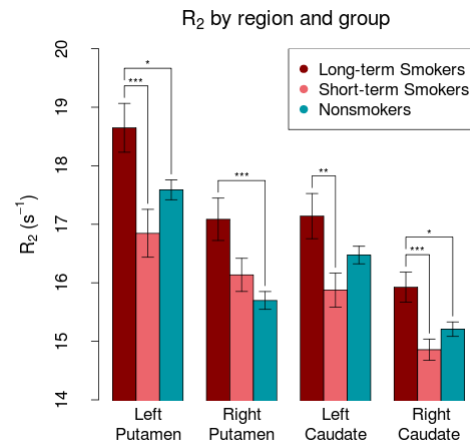
Figure 2: Effect of smoking history on striatal R_2 values. * $p<0.05$; ** $p<0.01$; *** $p<0.005$

$(r(27)=0.36, p=0.053)$ and left putamen $(r(27)=0.30, p=0.12)$ and in the left pallidum $(r(27)=0.30, p=0.11)$, but these failed to reach significance.

Discussion and Conclusions: Individuals with "long-term" smoking histories had increased R_2 values in the caudate and putamen compared to aged-matched nonsmokers and individuals with short-term smoking histories. Increased R_2 values were correlated with pack year history in the caudate. In the aging brain, there are two major changes in tissue composition that affect R_2 measures:

increased water content which decreases R_2 and increased iron content which increases R_2. While both of these processes could contribute to the current results, it seems unlikely that smoking would be associated with decreased tissue water content in these regions, as smoking has been repeatedly associated with increased brain water content in large white matter regions.[4] This suggests that our results are consistent with the hypothesis that smoking cigarettes increases lifetime brain iron accumulation in basal ganglia structures in a dose dependent manner. If verified and replicated, these findings would complement previous studies demonstrating regional and systemic alterations in iron metabolism in smokers[1,2,3] as well as findings in rodent models showing increased brain iron levels in response to cigarette smoke exposure.[5] Increased brain iron levels have been associated with age-associated cognitive impairment and risk of dementia.[6,7,8] The current study suggests that cigarette smoking increases brain iron content and this effect may provide some insight into the associations of smoking and cognitive decline in old age.[9]

1. McGowan, S. E.; Murray, J. J. & Parrish, M. G. J Lab Clin Med, 1986, 108, 587-595. **2.** Ghio, A. J.; Hilborn, E. D.; Stonehuerner, J. G.; Dailey, L. A.; Carter,

J. D.; Richards, J. H.; Crissman, K. M.; Foronjy, R. F.; Uyeminami, D. L. & Pinkerton, K. E. Am J Respir Crit Care Med, 2008, 178, 1130-1138. **3.** Pacht, E. R. & Davis, W. B. J Lab Clin Med, 1988, 111, 661-668. **4.** Kim SH, Yun CH, Lee SY, Choi KH, Kim MB, Park HK.Neurol Sci. 2012 Feb;33(1):45-51. **5.** Anbarasi K, Vani G, Balakrishna K, Devi CS. Life Sci. 2006 Feb 16;78(12):1378-84. **6.** Bartzokis, G., Lu, P. H., Tingus, K., Peters, D. G., Amar, C. P., Tishler, T. A., Finn, J. P., Villablanca, P., Altshuler, L. L., Mintz, J., Neely, E. & Connor, J. R. Neuropsychopharmacology 2011; 36(7): 1375-1384; **7.** Penke, L., Hernandéz, M. C. V., Maniega, S. M., Gow, A. J., Murray, C., Starr, J. M., Bastin, M. E., Deary, I. J. & Wardlaw, J. M. Neurobiol Aging 2012: 33(3):510-517; **8.** Sullivan, E. V., Adalsteinsson, E., Rohlfing, T. & Pfefferbaum, A. Brain Imaging Behav 2009; 3(2): 167-175. **9.** Anstey KJ, von Sanden C, Salim A, O'Kearney R. Am J Epidemiol. 2007 Aug 15;166(4):367-78.